

THE *WISE* EXTENDED SOURCE CATALOGUE (WXSC)
I: THE 100 LARGEST GALAXIES

T.H. JARRETT,¹ M.E. CLUVER,^{2,3} M.J.I. BROWN,⁴ D.A. DALE,⁵ C.W. TSAI,⁶ AND F. MASCI⁷

¹*Department of Astronomy, University of Cape Town, Rondebosch, South Africa*

²*Centre for Astrophysics and Supercomputing, Swinburne University of Technology, John Street, Hawthorn 3122, Victoria, Australia*

³*Department of Physics and Astronomy, University of the Western Cape, Robert Sobukwe Road, Bellville 7535, South Africa*

⁴*School of Physics and Astronomy, Monash University, Clayton 3800, Victoria, Australia*

⁵*Department of Physics and Astronomy, University of Wyoming, Laramie, WY 82071, USA*

⁶*Department of Physics and Astronomy, University of California, Los Angeles, Los Angeles, CA, 90095, USA*

⁷*Infrared Processing and Analysis Center, California Institute of Technology, Pasadena, CA 91125, USA*

(Accepted Oct 23, 2019)

Submitted to ApJS

ABSTRACT

We present mid-infrared photometry and measured global properties of the 100 largest galaxies in the sky, including the well-studied Magellanic Clouds, Local Group galaxies M 31 and M 33, the Fornax and Virgo Galaxy Cluster giants, and many of the most spectacular Messier objects (e.g., M 51 and M 83). This is the first release of a larger catalog of extended sources as imaged in the mid-infrared, called the *WISE* Extended Source Catalogue (WXSC). In this study we measure their global attributes, including integrated flux, surface brightness and radial distribution. The largest of the large are the LMC, SMC and the Andromeda Galaxy, which are also the brightest mid-infrared galaxies in the sky. We interrogate the large galaxies using *WISE* colors, which serve as proxies for four general types of galaxies: bulge-dominated spheroidals, intermediate semi-quiescent disks, star-forming spirals, and AGN-dominated. The colors reveal a tight “sequence” that spans 5 magnitudes in $W2 - W3$ color, ranging from early to late-types, and low to high star-forming activity; we fit the functional form given by: $(W1 - W2) = [0.015 \times e^{\frac{(W2 - W3)}{1.38}}] - 0.08$. Departures from this sequence may reveal nuclear, starburst, and merging events. Physical properties and luminosity attributes are computed, notably the diameter, aggregate stellar mass and the dust-obscured star formation activity. To effectively study and compare these galaxy characteristics, we introduce the ‘pinwheel’ diagram which depicts physical properties with respect to the median value observed for *WISE* galaxies in the local universe. Utilized with the WXSC, this diagram will delineate between different kinds of galaxies, identifying those with similar star formation and structural properties. Finally, we present the mid-infrared photometry of the 25 brightest globular clusters in the sky, for which many are also the largest and brightest objects orbiting the Milky Way, including Omega Centauri, 47 Tucanae and a number of famed night-sky targets (e.g., M 13).

Keywords: galaxies: photometry, star formation — infrared: galaxies — surveys

1. INTRODUCTION

In the realm of our galactic neighbours, the most appropriate distance scale is megaparsecs. At these vast distances, even the nearest of these *island universes* appear faint and low surface brightness. It has been well on 100 years since they were first identified as distinct objects beyond the Milky Way. Nevertheless, the nearest spiral galaxies have held fascination for centuries – they were somehow different from the wealth of stars and Galactic nebulae. The observations of M 51 by Lord Rosse, in the 1840’s, clearly showed spiral arms, the nucleus and a companion galaxy, all of which were singularly unique to astronomers at the time.

Galaxies such as Andromeda (M 31), Triangulum (M 33), the Whirlpool (M 51), and the Pinwheel (M 101) have been the focus of observations since at least the times of Lord Rosse, possibly earlier by medieval Persian astronomers¹. Their relatively close proximity, less than 10 Mpc, means they are the largest galaxies in angular appearance. Today, the largest galaxies in the sky are still some of the favourite laboratories to study the internal gas and stellar components, dynamics, present and historic star formation, as well as used to construct local analogues of high-redshift systems.

There are a variety of galaxy types that are local to the Milky Way, as such they can be studied with physical resolutions that are necessary to connect the star formation processes, e.g. cloud collapse at the pc level, to their environment – the galaxy “main sequence” at two orders larger in scale – to the kpc-scale components such as spiral arms, bars, bulges, that represent the ‘skeleton’ of the galaxy. These galaxies are important because they not only offer a window into the workings of these individual galaxies, but can also serve as proxies for galaxies in the early universe. The most active galaxy building epoch was between redshifts of 1 and 3 (e.g., Hopkins & Beacom 2006), but even space telescopes cannot access these systems with the detail and fidelity that is (currently only) possible in the local volume, within 10 to 20 Mpc. To begin to understand the galaxy “ecosystem”, you must first study nearby galaxies.

Since the days of Vesto Slipher and Edwin Hubble, nearby galaxies have been carefully studied using a combination of spectroscopy and imaging to decode their nature. We have a wealth of data on tens of thousands of nearby galaxies, fully articulated in archives such as the NASA Extragalactic Database (NED) and Lyon-Meudon Extragalactic Database (HyperLEDA), mostly from optical observations, both photographic

(e.g., RC3) and CCD imaging (e.g., SDSS), but also in the last four decades from UV and infrared whole-sky surveys of galaxies (e.g., *GALEX*, *IRAS*, 2MASS, *WISE*). Completing the electromagnetic spectrum, from the radio to the gamma-ray, the latest surveys hope to provide new and complementary ways of looking at galaxies, unlocking the complex processes of the baryonic cycle: halo accretion, star formation, feedback and Gyr secular evolution.

One such survey, the Wide-field Infrared Survey Explorer (*WISE*; Wright et al. 2010), is well suited to the study of galaxy evolution in general, and to nearby galaxies in particular. The reason is that *WISE* has imaged the entire 4π sky – with relatively uniform breadth and depth. The imaging bands are sensitive to both stellar population and ISM processes, which can be used to study the past-to-present star formation history (Jarrett et al. 2013). The ALLWISE Catalogue (Cutri et al. 2012) and the upcoming CATWISE catalog (Eisenhardt et al. 2019) are optimized for point sources, both Milky Way stars and high-redshift galaxies. The *WISE* mission did not make provision for systematically and properly measuring resolved sources; hence, these catalogs are either incomplete or poorly constructed for nearby and resolved galaxies. We estimate that there are at least 2 million resolved galaxies detected in the *WISE* all-sky imaging, similar to the 2MASS Extended Source Catalogue (Jarrett et al. 2000). As such, our mission has been to identify and measure resolved galaxies in the *WISE* imaging. **We have carried out a systematic study of nearby galaxies, first introduced in the pilot study by Jarrett et al. (2013), that endeavours to build dedicated mosaics for all resolved galaxies, extract and characterize their measurable attributes, and produce uniform catalogs.** For those with redshifts or known distances, their physical (global) attributes are derived, including stellar mass and star formation activity. **The over-arching project is called the *WISE* Extended Source Catalogue (WXSC).**

The full-sky coverage of *WISE* means that every galaxy in the sky is imaged (to the sensitivity limits of *WISE*, see below), including the largest and most extended objects. Hence, *WISE* has the unique dual capability of adding ancillary infrared data to any survey or observation, while also the ability to study the largest objects in the sky. It is this current study that addresses the latter capability. As a first major release, the largest angular-extent galaxies in the sky lead the way, which is appropriate given their historical and contemporary importance to galaxy studies. Subsequent releases of the WXSC will include well-known samples, such as the

¹ Notably Abd Al-Rahman Al-Sufi in his “Book of the Fixed Stars”, published in 964 AD

NGC, UGC, S⁴G, as well as new galaxies that may be used to target spectroscopic surveys such as TAIPAN (da Cunha et al. 2016) and SDSS-V (Kollmeier et al. 2017). To date we have measured and cataloged over 70,000 galaxies in the WXSC.

Inspired by the release of the largest 2MASS galaxies (Jarrett et al. 2003), here we present the angular largest 100 *WISE* galaxies in the sky, which includes most of the Local Group (LG), and many of the most famous Messier objects (M81, M51, M83, M101), as well as ‘exotic’ varieties, the starbursts NGC 253 and M82, and the AGN systems: NGC 1068 (M77) and the Circinus Galaxy. Some of the WXSC data (mosaics and measurements, including large galaxies) have already been used in recent studies, notably neutral hydrogen studies of NGC 253 (Lucero et al. 2015), M83 (Heald et al. 2016) and M33 (Kam et al. 2017; Elson et al. 2019), multi-wavelength studies of NGC 6744 (Yew et al. 2017) and M31 (Tomicic et al. 2019), baryonic Tully-Fisher study (Ogle et al. 2019), moderate-sized samples (e.g., HIPASS) that study star formation-stellar mass relations (Hall et al. 2018) and the star-formation-gas connection (Korsaga et al. 2018; Parkash et al. 2018, 2019). A number of studies are currently underway using the WXSC, including a complete census of the Coma and Perseus-Pisces Galaxy Clusters. One of the most important applications of the WXSC comes from Cluver et al. (2017) who derived a new set of star formation rate (SFR) relations using *WISE* and total infrared luminosities from SINGS (Kennicutt et al. 2003) and KINGFISH (Kennicutt et al. 2011). We will be using these SFR relations to characterize WXSC galaxies.

Here we present a uniform set of mosaics and measurements, and derive global properties, that may be used to study the local volume of galaxies. We compare the measurements of the 100 Largest with a statistically-significant sample from the local universe, as compiled in the WXSC, to give context and contrast (if any) to the largest angular-sized galaxies. For completeness, we also provide measurements of LG galaxies that do not satisfy the angular size requirement. Finally, measurements for the largest and brightest (Milky Way) globular clusters are also included since they are both large, bright and require similar photometric methods to extract their global fluxes. We note this current release of the 100 largest galaxies will be directly followed by the periodic release of WXSC galaxies, whose catalog and data products will be fully described in a second paper, hereafter referred to as Paper II.

This paper is organized as follows: Explanation of source measurements and the data are presented in §2. The 100 largest galaxy sample is introduced in §3.

Source properties, such as coordinates, size, shape, and photometry are presented in §4. We then derive global physical attributes for the sample, and compare with large WXSC samples to assess the nature of the largest galaxies relative to the local universe; §5. In §6 we introduce a new way to graphically study the physical attributes, which will be used in future releases; and finally, §7 presents the photometric measurements for the brightest globular clusters.

For galaxies without redshift independent distances, the cosmology adopted throughout this paper is $H_0 = 70 \text{ km s}^{-1} \text{ Mpc}^{-1}$, $\Omega_M = 0.3$ and $\Omega_\Lambda = 0.7$. The conversions between luminosity distance and redshift use the analytic formalism of Wickramasinghe & Ukwatta (2010) for a flat, dark energy dominated Universe, assuming standard cosmological values noted above. Length and size comparisons are all carried out within the co-moving reference frame. All magnitudes are in the Vega system (*WISE* photometric calibration described in Jarrett et al. 2011). Photometric colors are indicated using band names; e.g., W1–W2 is the $[3.4 \mu\text{m}] - [4.6 \mu\text{m}]$ color. The Vega magnitude-to-flux conversion factors are 309.68, 170.66, 29.05, 7.871 Jy, respectively, for W1, W2, W3, and W4. We adopt the new W4 calibration from Brown et al. (2014b), in which the central wavelength is $22.8 \mu\text{m}$ (and hence we will refer to W4 as $23 \mu\text{m}$) and the magnitude-to-flux conversion factor is 7.871 Jy. It follows that the conversion from Vega System to the monochromatic AB System conversions are 2.67, 3.32, 5.24 and 6.66 mag.

2. *WISE* IMAGING & SOURCE CHARACTERIZATION

In this section we describe the data, the imaging products, source characterization and selection of the largest galaxies. All of the data are derived from the *WISE* mission, notably the level-1 individual frames and the ALLWISE source catalogs (Cutri et al. 2012). Mosaics are constructed from the individual-epoch frames, and source characterization commences with both automated pipelines and expert-user interaction. Measurements are carried out on galaxies, roughly 70,000 to date as part of the *WISE* Extended Source Catalogue, located in the local universe, $z < 0.3$, including the largest known galaxies. Here we report on the 100 largest in the sky, including four, LMC/SMC and M31/M33, of which required special processing due to their extreme angular extent.

2.1. *WISE* Mission Details

WISE is a NASA Medium-Class Explorer mission, launched in December 2009, featuring a 40-cm primary-mirror and 1024×1024 pixel Si:As and HgCdTe solid-

hydrogen-cooled arrays that simultaneously imaged in four broad-spectral bands (Wright et al. 2010). Simply abbreviated as W1, W2, W3 and W4, the bands are centered on 3.4, 4.6, 12 and 22 μm in the mid-infrared window, with a W1 point source sensitivity that reaches $\sim 25 \mu\text{Jy}$ (5σ ; Jarrett et al. (2017)). As previously noted, the W4 band has a filter response that is closer to 23 μm (Brown et al. 2014b), and hence we refer to the central wavelength of W4 band as 23 μm . This primary ‘cryogenic’ mission fully covered the sky several times (epochs) before the cryogen was exhausted (pre-2011), after which *WISE* began a new post-cryogen phase in which its two short bands (3.4 and 4.6 μm) continued to map the sky with passive thermal cooling, focusing on asteroid science (read all about NEOWISE at <http://wise2.ipac.caltech.edu/docs/release/postcryo/>).

2.2. Target Galaxies

Building the *WISE* Extended Source Catalogue is a multi-phase project, starting with known, cataloged galaxies and extending to galaxies in the local universe that are resolved by *WISE*. The former involves targeting specific galaxy catalogs (or samples), and the latter ‘blind’ detection and characterization to determine the nature of the object: star, galaxy, or otherwise (Jarrett et al. 2017). For the largest galaxies in the sky, we rely on known catalogs, including the optically-based RC3/UGC (de Vaucouleurs et al. 1991; Nilsson, 1973) and S⁴G (Sheth et al. 2010), and the databases NED and LEDA, to extract large galaxies. Additionally, since we are building an infrared catalog, specifically using W1 (3.4 μm) for the size metric, we include a number of infrared galaxy catalogs (e.g., IRAS Revised Bright Galaxy Sample, and the 2MASS XSC) to construct an initial sample to make sure we collect all of the largest galaxies.

To date, we have measured over 70,000 nearby galaxies, including discrete Local Group galaxies that are detected by *WISE*. Source characterization provides the W1 (3.4 μm) $1-\sigma_{\text{sky}}$ isophotal ($\sim 23 \text{ mag arcsec}^{-2}$) size, which is used to identify the 100 largest galaxies. Most of which are ‘normal’ galaxies, but also includes some physically notable examples, from M82 (starburst), to the AGN/Seyferts NGC 1068 (M77) and Circinus Galaxy. In addition to extragalactic sources, we have measured the brightest (Milky Way) globular clusters since they are some of the largest and brightest objects in the sky, with at least one of them, Omega Centauri (NGC 5139) considered to be a stripped dwarf galaxy (e.g., Noyola, Gebhardt, & Bergmann 2008). We describe the characterization process for globulars below, which is similar to that used for the Magellanic Clouds.

2.3. Mosaic Construction

Owing to the relatively small primary mirror, the *WISE* angular resolution is poor compared to *Spitzer*-IRAC, with $\sim 6\text{--}8''$ in the short bandpasses and $12''$ in the longest bandpass (Jarrett et al. 2012). It is therefore important to work with native-resolution mosaic images when measuring extragalactic sources, especially those that are resolved. Unfortunately the public-release ‘Atlas’ imaging from the *WISE* mission does not have native resolution – they were smoothed to primarily benefit point source detection. Hence, we have constructed new mosaics of all galaxies in the WXSC to have native resolution with a field-of-view size, from arc-minutes to degrees, capable of measuring both the target galaxy and its local environment (see Jarrett et al. (2013)). There is the added benefit of co-adding epochs that were not available during the primary ALLWISE mission, with additional data from NEOWISE (Mainzer et al. 2013) in the W1 and W2 bands resulting in deeper, more sensitive photometric imaging.

Mosaics feature re-sampling with $1''$ pixels using a ‘drizzle’ technique developed in the software package ICORE (Masci 2013) specifically designed for *WISE* single-frame images; details of the process and performance can be found in Jarrett et al. (2012). All galaxies have this well-sampled (relative to the beam) $1''$ pixel scale except for the LMC, SMC and M31: they are too large to practically accommodate the resulting extreme image sizes. Details of these exception galaxies and their processing is given below. Depending on the total coverage (and hence, depth), the typical $1-\sigma_{\text{sky}}$ surface brightness depths are 23.2, 22.1, 18.4 and 15.8 mag arcsec⁻² (Vega mags), respectively for W1, W2, W3 and W4 bands.

Mosaic construction is relatively straightforward for most galaxies. There are some cases which require extra attention, the highest surface brightness objects, specifically, M82, NGC 253, Circinus, NGC 1068, and NGC 2070 (see below), as well as some of the globular clusters, all saturated their cores, notably in the longest bands of *WISE*. Recovery of the lost information was carried out using a technique developed for *Spitzer* IRAC/MIPS image saturation (by the first author of this paper; see also the IRAC instrument handbooks² for more detail), which entails utilizing the PSF and super-resolution image construction (Jarrett et al. 2012) to recover the core information. The method was utilized successfully for these cases; nevertheless, the resulting core flux has a large uncertainty, 20–30%, which

² <https://irsa.ipac.caltech.edu/data/SPITZER/docs/irac/iracinstrumenthandbook/>

translates to an extra 3-5% uncertainty for the global flux.

In addition to the images, which include the signal, uncertainty and coverage maps per band, we also construct point spread functions (PSFs) that are used for star removal (see below).

2.4. Source Characterization

The goal of source characterization is to extract global parameters and to ‘reduce’ an image (or in this case, four multi- λ images) to a set of standard metrics that can be used to study the nature of the target galaxy. The most important parameters are the integrated flux (or brightness), size and shape (inclination for disk galaxies), surface brightness, and cross-band flux ratios (i.e., colors). There are many other parameters that are measured and cataloged (e.g., nuclear concentration), but are otherwise not discussed here, details will be given in Paper II. The basic source characterization pipeline has a heritage that extends from the 2MASS Extended Source Catalogue (Jarrett et al. 2000), also used in the *WISE* processing pipeline, and various aspects have been discussed in previous *WISE* work (Jarrett et al. 2011, 2013; Cluver et al. 2014; Jarrett et al. 2017; Cluver et al. 2017). Below we add some additional detail relevant to large galaxies.

One of the most important first steps is to identify and remove foreground Galactic stars so as not to contaminate the galaxy measurements. This is particularly important for W1 and W2, which are filled with foreground Milky Way stars; hence, particular attention is given to the W1 and W2 star-cleaning process. We identify stars using the ALLWISE Catalog (Cutri et al. 2012), which has basic point source characterization, the most important being the fluxes, colors and profile metrics – notably, the reduced χ^2_{reduced} which provides an assessment of the point or resolved nature of the object. We use a combination of the source colors and point-like characteristics to decide if the source should be removed from the image – that is to say, if the source is foreground or associated with the target galaxy.

We have found that sources that are resolved (i.e., galaxies in most cases) have a W1 χ^2_{reduced} value greater than 2 (Jarrett et al. 2011; Cluver et al. 2014; Jarrett et al. 2017). We use this metric to assess if the source is point-like (i.e., Galactic star, or background, distant galaxy) or resolved. If resolved, it may be a piece of the target galaxy (e.g., H II region), in which case we may not want to remove it, especially if located on a spiral arm or within the disk, or it may be a blend of two or three stars, necessitating its removal from the cleaned image. An even more powerful discriminant is the W2–W3 color, which is relatively ‘blue’ (low value)

for Galactic stars compared to extragalactic sources or star-forming (SF) regions in the target galaxies. In this way we avoid shredding our target galaxies into multiple pieces, which can be a real challenge for large imaging surveys and automated source extraction. Moreover, and crucially, we visually inspect every galaxy to make sure that stars have been properly identified and removed, and that the inverse, shredding, has not occurred, in any band. Stars are removed from the images by PSF subtraction, in the case of faint to moderately bright sources, W1 ~ 15 mag (0.3 mJy), and for bright stars we use a masking process in which pixels are then recovered using the local background. As noted, visual inspection and human-intervention are used for difficult cases, especially with source crowding and bright nearby stars, and for overall validation.

Once stars have been removed, the next step is to determine the local background value, which is an iterative – curve of growth, flux convergence – process such that the local background is determined in a centered elliptical annulus whose inner and outer radii are safely (30 to 50%) beyond the light coming from the target galaxy. Stars are excluded from the distribution through subtraction and masking. Using the same method as that developed for *WISE* point-source processing, the local background is derived from a mean centered about the pixel-value distribution mode of the annulus pixel values (previously cleaned of foreground stars). The RMS uncertainty (σ_{sky}) of this background value is computed from the width of the distribution, as described in the *WISE* Explanatory Supplement (Cutri et al. 2012). For nearly all cases a simple offset is all that is needed to removed the background emission, but in the case of M31, a tilted plane was used to account for the slight background light gradient (orthogonal to the Galactic Latitude axis) across the enormous field area, over 25 deg².

The local background, or sky value, is subtracted from the star-cleaned mosaics, and the primary source characterization is then carried out. Shape characterization is derived from the $3\text{-}\sigma_{\text{sky}}$ elliptical isophote, and held fixed for all measurements; i.e., the source is assumed to be elliptical and axi-symmetric. The maximum extent of the galaxy is determined at the $1\text{-}\sigma_{\text{sky}}$ elliptical isophote, which then represents the isophotal aperture for integrated flux measurements. The total light, however, is estimated using both larger apertures (approaching the asymptotic limit) and by first constructing the radial surface brightness distribution, fitting a double Sérsic function, and extrapolating the extent of the galaxy to three disk scale lengths (based on the Sérsic scale lengths). The resulting ‘extrapolation’ flux

represents the “total” flux, although it is not much more (5 to 10%) than the isophotal flux, and agrees very well (1 to 2%) with the asymptotic flux in most cases; details are in Section 4.1. Finally, integrating radially from the center until 50% of the integrated light is reached, the half-light (or effective) radius and surface brightness are then derived from the total flux.

These are the basic steps that are used to measure resolved galaxies. However, there are four notable exceptions that require further explanation: M 31, M 33, LMC and SMC, given below.

2.5. Magellanic Clouds

With the Magellanic Clouds, our challenging aim was to construct a mosaic large enough to encompass both galaxies, thereby revealing the bridge region between them. The Large and Small Clouds encompass a region of the sky that is ~ 35 degrees across, mostly along the equatorial axis. This is far too large to accommodate $1''$ pixels, and given our primary goal of measuring the global properties of the Clouds, we did not require heavy over-sampling. Consequently, we chose a pixel scale that was comparable to the resolution of *WISE*, specifically $8''$ pixels.

The resulting images (four bands) are $18,501 \times 10,001$ pixels, constructed with an equatorial projection (a galactic projection is not all that different), with the LMC to the east, and the SMC to the west. Artifacts from bright stars in the images are manually removed, and the *WISE* bands are combined to form a four-color panorama of the region; see Figure 1. The depth of the images is relatively high for *WISE* because of the proximity to the South Ecliptic Pole; the resulting high coverage (>100 epochs on average) is good for optimal sensitivity, but the source confusion in W1 is reaching its peak (explored in detail by Jarrett et al. 2011). So although the longward bands, W3 and W4, have excellent sensitivity in this region, the short bands of W1 and W2 are reaching diminishing returns with confusion noise.

The LMC is graced by the star formation complex 30 Doradus (aka the Tarantula Nebula), which is both spectacular, and supremely bright in the mid-infrared, so much so that the central star cluster (NGC 2070) saturates in all four *WISE* bands. The multiple-core saturation was rectified (see Section 2.3), and the restored super-resolution image is shown in Fig. 1 with the inset image on the east side. On the west side, the SMC is shadowed by the magnificent globular cluster 47 Tucanae, which was also saturated in the core (W1 only) and restored using the PSF and super-resolution; see the inset figure showing 47 Tuc.

Source characterization for the Magellanic Clouds is carried out on the large mosaics. Since both objects are

large in angular extent compared to the field of Galactic stars, it is not practical to identify stars within the Clouds that may or may not belong to the Milky Way. This is also the case for M 31, M 33 and, worst case, globular clusters since member stars look just like foreground Galactic stars. Hence, we employ a technique developed for measuring globular clusters in 2MASS (Jarrett et al. 2003), whereby the mean flux of the foreground Galactic stars is measured and subtracted from the target galaxy. The assumption is that the mean flux (per pixel) of the starlight as measured in a patch of sky (annulus centered on the target galaxy) is the same as that within the galaxy. This is statistically robust for faint stars, but clearly there can be fluctuations from bright stars. To minimize this deleterious effect, we identify bright Milky Way stars, contained in the ALLWISE Catalogue, from both the target and the sky patch and remove them before statistical measurements are taken.

In the infrared, the LMC displays the well-known stellar bar (appearing blue and elliptical in Fig. 1), but also appears strangely square or “blocky” in the ISM bands. This is not an artifact of the *WISE* imaging, it is real and can also be seen in the large *Spitzer*-SAGE mosaics of the LMC (Meixner et al. 2006) and in *IRAS* $60 \mu\text{m}$ dust maps. To measure the global flux of the LMC, we have chosen to use a circular aperture (for simplicity) that fully covers the LMC, extending 10 degrees in diameter, encompassing the bar (seen in W1 and W2) and the star formation regions (W3 and W4). For the sky patch, we choose a region that is equally between the LMC and the SMC so that we can use the same mean stellar “sky” flux for both clouds. The sky region is centered on (03:00:45, -71:42:10) and has a radius of 4.5 degrees. The resulting Galactic foreground mean surface brightness is 21.62, 21.38, 20.41 and 19.10 mag arcsec $^{-2}$ (Vega system) for the sky patch (W1, W2, W3 and W4, respectively), which is then subtracted from the surface brightness of each pixel in the LMC and the SMC.

One final note of interest with the big mosaic; there is a “river” of emission extending from the north to south, west of the LMC, that appears to terminate in the Chameleon II SF complex of the Milky Way. It is notably bright in W3 (hence, orange-reddish in the adopted Fig. 1 color scheme), which would suggest the emission arises from warm dust and polycyclic aromatic hydrocarbon (PAH) emission in the bridge region, or possibly a closer projection from the Milky Way itself. Although you can clearly see “ringing” artifact features throughout this large mosaic of the Magellanic clouds, the N-S filament is in fact real. You can see the exact correspondence in deep optical imaging (Besla et al. 2016, using a wide-field luminance filter imaging),

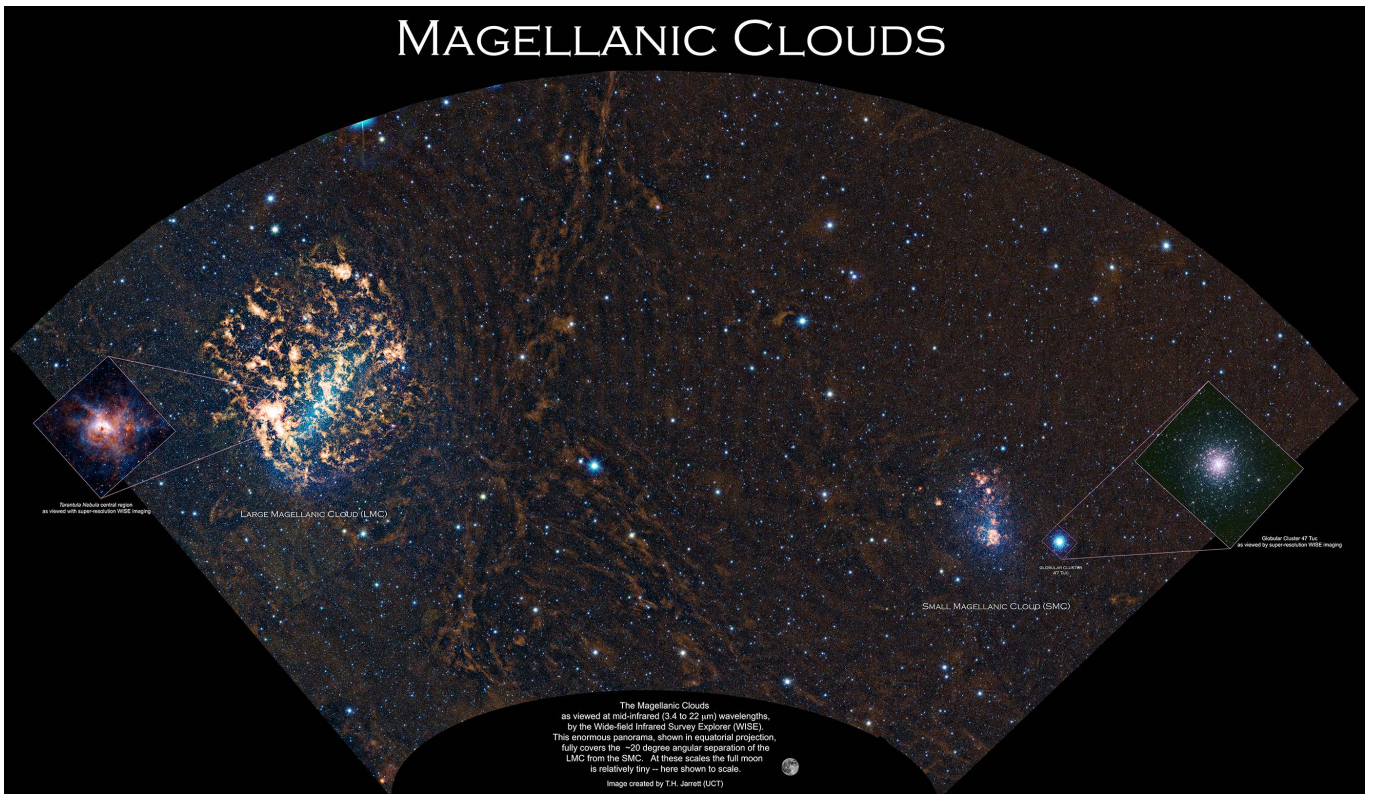


Figure 1. Mid-infrared four-color panorama of the Magellanic Clouds, constructed from *WISE* imaging. This equatorial projection fully covers the >20 degree separation between the LMC and the SMC. The insets show *WISE* super-resolution mosaics of the Tarantula Nebula (30 Dor) in the LMC, and the globular cluster 47 Tuc adjacent to the SMC. Note the long stream of nebulosity running north-south between the clouds, this is real emission likely associated with the tidal interaction between the clouds and the Milky Way.

and in *IRAS* maps, the so-called Galactic cirrus filaments – perfectly consistent with *WISE* $12\ \mu\text{m}$ imaging – and even in Planck 353 GHz polarization maps. The large-scale feature may be related to the tidal interaction between the Clouds and the Milky Way, or simply a nearby magnetic-field-collimated dust filament that is unrelated to the Magellanic Clouds. In any case, it is a very interesting feature for further investigation.

2.6. *M31 and M33*

The extreme angular size of M31 and M33 required using a larger pixel scale (to conserve CPU memory, for example); here we construct with $1.5''$ pixels. The necessary angular extent of the images was first estimated by using the W1 stellar number density from the ALLWISE catalog, computed in shells that extended from the center of M31 out to large radii. In close proximity to M31 the number density is high, while at large radii the value settles to the Milky Way mean value corresponding to about 3 degrees from the center of M31 (Chauke 2013). In this way we determined that a 6 degree mosaic of M31 would be sufficient to measure the galaxy in the *WISE* bands; although M31 may yet extend beyond this range, we are not able to measure it, relative to the field,

outside a radius of approximately 3 degrees. Moreover, since M31 is fairly inclined and its orientation is diagonal in equatorial projection, we decided to construct the mosaic in *WISE* spacecraft mapping orientation (ecliptic). In this way, M31 disk appears horizontal, which is the optimal projection for minimizing the size of the required mosaic. In the case of M33, since the galaxy is not nearly as large, we used the standard equatorial projection with a 2 degree extension along the north-south axis.

It is not as straightforward to identify foreground Galactic stars from actual M31 sources due to the angular size of M31 and the large foreground Galactic population (centre of M31 is located at Galactic coordinates: $l = 121.2^\circ$, $b = -21.6^\circ$). The method we developed was part of a Masters dissertation (Chauke 2013), and it uses in combination the stellar number density, proximity to the M31 disk, and photometric properties of the ALLWISE sources to determine the nature of the source. It is a statistical method that determines the likelihood that a source belongs to M31 or to the Milky Way. For example, well beyond the nucleus of M31, >2.7 deg, the field is completely dominated by Galac-



Figure 2. *WISE* four-color view of the Andromeda (M31) galaxy, projected in the ecliptic (spacecraft) orientation. The upper panel shows the galaxy, its satellite galaxies (M32 and M110) and foreground Galactic stars, while the bottom panel shows only the galaxy with stars and satellites removed. The outstanding feature with the infrared is that spiral arms embedded with molecular clouds and SF activity are in emission, as compared to absorption at optical wavelengths.

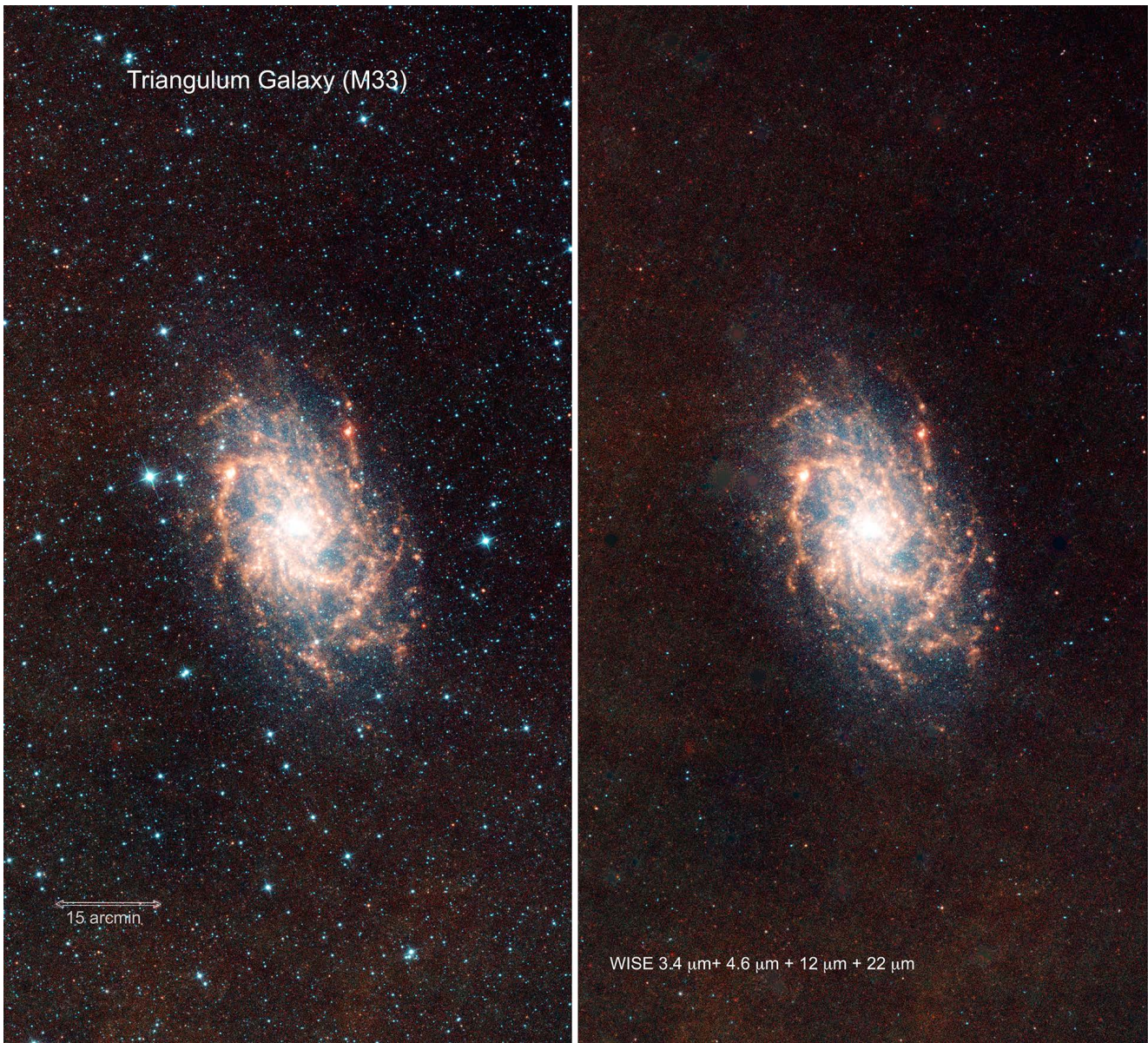


Figure 3. *WISE* four-color view of the Triangulum (M33) galaxy. The left panel shows the galaxy and foreground Galactic stars, while the right panel shows only the galaxy. M33 is one of the best targets in the sky to study because it is relatively face-on and presents parsec-scale SF regions for an entire range of spiral arm radii and environments.

tic stars, and the W1 star-counts and colors (W1–W2, W2–W3) have a signature of the Galactic population at the longitude and latitude of M31. In closer proximity to the disk of M31, the source counts rise and the photometric properties begin to change; e.g., more faint stars are seen, from M31 itself, and colors redden because the K/M-giant populations are the only extragalactic stars detected because of the distance of M31 relative to Milky Way stars; and hence, evolved and luminous stars appear much fainter (the distance modulus of M31 is about 24 magnitudes). Exploiting these differences, we determine the most-likely Galactic foreground pop-

ulation, which are then removed from the M31 cleaned mosaic.

The total number of foreground stars within the influence of M31 is impressive: in a 11 deg^2 region centered on M31, over 100,000 foreground stars are identified. We should note that near the nuclear bulge of M31, the density of sources is so high that confusion and crowding renders any source identification as impossible, and Galactic stars will remain in the bulge region. Nevertheless, this is a relatively small area and the estimated flux of the total number of Galactic sources in the bulge is still less than 1% of the total flux of M31 itself. So with the sources that are identified as Galactic, they are

removed from the image using the technique of PSF and area-masking, described earlier. The resulting mosaic of M31 is shown in Fig. 2

The same statistical method for star identification is used for M33, although not as challenging since M33 is considerably smaller ($\sim 1/3$) relative to M31, and is located further from the Galactic Plane (coordinates: $l = 133.6^\circ$, $b = -31.3^\circ$). Crowding is also much less of a problem, as M33 has a weak stellar bulge. The cleaned mosaic of M33 is shown in Fig. 3.

3. THE LARGEST GALAXIES IN THE SKY

We choose as the primary metric for angular size the *WISE* W1 ($3.4\ \mu\text{m}$) $1\ \sigma_{\text{sky}}$ isophotal radius (that is, the semi-major axis of the disk or tri-axial stellar distribution). The W1 spectral window is sensitive to starlight from evolved stars, characterized by the stellar ‘bump’ which peaks in the H-band ($1.6\ \mu\text{m}$) and extends into the mid-infrared through the Rayleigh-Jeans (R-J) tail. Similar to using the K-band ($2.2\ \mu\text{m}$) as a tracer of the host galaxy stellar mass, the W1 band has been shown to be an excellent proxy for the stellar component of the baryonic mass (Jarrett et al. 2013; Meidt et al. 2014; Cluver et al. 2014; Ponomereva et al. 2017; Kettlety et al. 2018; Hall et al. 2018).

In terms of surface brightness, *WISE* is relatively sensitive because it is a space-bound and it has large native pixels ($2.5\ \text{arcsec}$). Consequently, in the W1 band the typical RMS per pixel is about $23\ \text{mag arcsec}^{-2}$ (Vega), and faint depths are reached with axi-symmetry averaging, typically $25\ \text{mag arcsec}^{-2}$ (Vega), or $\sim 28\ \text{mag arcsec}^{-2}$ (AB), similar to those achieved with *S⁴G*’s *Spitzer*-IRAC (Sheth et al. 2010). These depths are considerably fainter than the K_s -band in 2MASS which typically reaches $20\ \text{mag arcsec}^{-2}$, and so W1 has much larger radii, ranging from 2 to 5 times larger than as measured by 2MASS K_s -band (Cluver et al. 2014). Moreover, as will be shown below, the ‘total’ integrated flux in the W1 channel is 95% contained within the isophotal aperture; and hence, the W1 $1\text{-}\sigma_{\text{sky}}$ isophote is both robustly measured as well as being a good trace of the size and mass of the galaxy.

Based on the *WISE* W1 angular radius, we present the largest 100 galaxies in the sky in Table 1. The table is sorted by the isophotal radius, and includes the Hubble Type, axis ratio (b/a), position angle orientation (East of North), and the integrated fluxes, quoted in flux density and in Vega magnitudes. These parameters represent only a small subset of the full characterization that is completed for each galaxy (e.g., surface bright-

nesses, total fluxes, etc). This additional data will be made available online with the full WXSC data release.

Not surprisingly, the largest galaxies in the sky are the Magellanic Clouds (Fig. 1), followed by the other Local Group galaxies M31 and M33 (Figs. 2, 3). These galaxies have extents that can be measured in degrees, whereas the remaining galaxies in the universe have sizes in the arcmin and arcsec range. We should note that it is challenging to measure the actual extent of these galaxies due to their sheer size relative to the imaging focal plane that they are measured with, thus requiring extremely large mosaic constructions. Moreover, in the case of the Magellanic Clouds, they do not have well defined shapes; the LMC has an elliptical bar and a squarish-ISM (see Fig. 1), while the SMC is irregular in shape and extent. Hence, the infrared size quoted here, 10 degrees diameter for the LMC and 5.6 degree for the SMC, has considerable uncertainty, $>10\%$.

The general galaxy properties and measured photometry are listed in Table 1. The first column (IS) indicates the radial size order, and the second column (IB) is the order based on the W1 integrated flux. The rank of the radius and integrated brightness correlates, as shown in Figure 5 and Figure 6. The LMC is the brightest galaxy in the sky, in terms of its integrated flux: 1828, 1064, 2377, and 5728 Jy, respectively for the four bands of *WISE*. Next is Andromeda: 285, 152, 175, and 143 Jy, which just edges that of the SMC. Both the Magellanic Clouds have larger W4 fluxes due to their current star formation (see Section 5.4).

Besides the famed LG galaxies, the largest galaxies includes many that are well-studied, including the local starburst NGC 253 (#5), Centaurus A (#6), M101 (the Pinwheel; #9), NGC 1316 (Fornax A, #12), the Sombrero (#17), Virgo A (#21), LG dwarf NGC 6822 (#25), M83 (Southern Pinwheel, #27), M51 (Whirlpool, #42), the Fireworks (#49), knife-edge NGC 5907 (#63), the Seyfert galaxy Circinus (#75) located behind the Milky Way, the starburst M82 (#83), and spectacularly NGC 1068 (#85, M77), to name just a few. Some of the largest-extent galaxies are not all that bright (e.g., the local dwarfs), correspondingly, some of the brightest galaxies are not in this list of large galaxies; if we only consider the SF bands of W3 and W4, compact luminous IR galaxies would make the list of Top 100, such as Arp 220.

A large fraction of the LG galaxies appear in the list, however, a few notable ones are too small or too faint in surface brightness to detect in angular extent. Hence, for completeness, we include the LG galaxies that *WISE* is able to detect and measure; note that many of the tiny and diffuse dwarf galaxies are not in play here. Table 1, at the bottom, the list includes IC 1613, M32, UGC 5373 and ESO 245-007 (Phoenix Dwarf).

Table 1. Photometry of the 100 Largest Galaxies Imaged by *WISE*

iS	iB	Galaxy	R.A. deg	Dec deg	Morph	ba	pa	R _{W1} amin	m1 ± Δm1 mag	R _{W2} amin	m2 ± Δm2 mag	R _{W3} amin	m3 ± Δm3 mag	R _{W4} amin	m4 ± Δm4 mag
(1)	(2)	(3)	(4)	(5)	(6)	(7)	(8)	(9)	(10)	(11)	(12)	(13)	(14)	(15)	(15)
1	1	LMC	79.64101	-68.81836	SBm	1.00	0.0	300.00	-1.93	300.00	-1.99	300.00	-4.78	300.00	-7.15
2	3	SMC	13.18660	-72.82860	SBm-pec	1.00	0.0	166.67	0.56	166.67	0.62	166.67	-0.93	166.67	-3.48
3	2	MESSIER31	10.68479	41.26907	Sb	0.35	37.3	111.44	0.08	111.44	0.13	111.44	-1.95	111.44	-3.09
4	5	MESSIER33	23.46204	30.66022	Sc	0.59	18.9	31.64	3.09	31.64	3.02	31.64	-0.17	31.64	-1.94
5	6	NGC0253	11.88844	-25.28827	SABc	0.28	53.0	21.13	3.46	21.13	3.27	21.13	-0.54	21.13	-2.94
6	4	NGC5128	201.36481	-43.01954	S0	0.77	33.8	19.64	3.01	19.64	2.98	19.64	0.45	19.64	-1.25
7	36	NGC0055	3.72192	-39.19775	SBm	0.19	108.9	19.49	5.45	19.49	5.36	19.49	2.80	19.49	0.29
8	7	MESSIER81	148.88837	69.06528	Sab	0.56	156.7	14.67	3.60	14.67	3.61	14.67	1.84	14.67	0.45
9	27	MESSIER101	210.80225	54.34893	SABc	0.92	33.3	14.50	5.22	14.50	5.10	14.50	1.62	14.50	-0.28
10	12	NGC4945	196.36409	-49.46816	SBc	0.37	43.4	12.98	4.07	12.98	3.87	12.98	0.31	12.98	-1.56
11	10	IC0342	56.70144	68.09635	SABcd	0.95	75.5	12.98	3.97	12.98	3.89	12.98	0.23	12.98	-1.81
12	23	NGC1316	50.67380	-37.20796	S0	0.64	34.7	12.82	5.08	10.03	5.14	3.38	4.49	3.38	3.24
13	20	MESSIER49	187.44489	8.00050	E	0.77	152.0	12.75	4.95	9.73	5.08	2.58	4.82	2.58	3.92
14	37	MESSIER86	186.54897	12.94619	E	0.62	127.2	11.88	5.48	9.05	5.58	1.74	5.96	1.74	5.10
15	9	MAFFELI	39.14779	59.65487	E-S0	0.77	89.3	11.54	3.94	10.33	3.96	1.74	4.18	1.74	2.80
16	31	MESSIER110	10.09197	41.68548	E	0.50	168.2	11.36	5.32	10.10	5.41	10.10	4.65	10.10	3.34
17	16	MESSIER104	189.99765	-11.62305	Sa	0.46	90.7	11.04	4.62	9.28	4.66	3.67	3.74	3.67	2.57
18	43	NGC2403	114.20885	65.60103	SABc	0.53	124.1	10.94	5.69	10.94	5.59	10.94	2.26	10.94	0.28
19	99	NGC0247	11.78529	-20.76036	SABc	0.30	171.9	10.90	6.49	10.90	6.52	10.90	4.06	10.90	2.28
20	28	MESSIER106	184.73955	47.30408	Sbc	0.46	152.0	10.67	5.23	10.67	5.19	10.67	2.75	10.67	1.09
21	30	MESSIER87	187.70593	12.39113	E	0.79	152.9	10.37	5.32	6.88	5.46	1.86	5.14	1.86	3.84
22	48	NGC3628	170.07085	13.58912	SBb	0.23	105.1	10.20	5.76	8.24	5.64	8.24	2.44	8.24	0.51
23	46	NGC0300	13.72251	-37.68413	Scd	0.77	123.2	10.03	4.77	10.03	5.73	10.03	3.13	10.03	1.28
24	18	NGC4736	192.72110	41.12020	SABa	0.89	105.6	9.64	4.77	7.19	4.78	7.19	2.03	7.19	0.32
25	51	NGC6822	296.24115	-14.80224	IBm	0.82	20.5	9.53	5.80	9.53	5.80	9.53	3.50	9.53	1.20
26	90	NGC1532	63.01807	-32.87421	SBb	0.24	32.2	9.44	6.43	7.40	6.41	7.40	3.61	7.40	2.00
27	13	NGC5236	204.25296	-29.86598	Sc	0.95	161.4	9.33	4.24	9.33	4.12	9.33	0.32	9.33	-1.86
28	109	NGC0147	8.30052	48.50901	E	0.57	28.7	9.28	6.57	7.52	6.69	7.52	4.84	7.52	null
29	38	NGC6744	287.44211	-63.85751	Sbc	0.70	11.9	9.14	5.49	9.14	5.47	9.14	2.27	9.14	0.68
30	29	MESSIER63	198.95549	42.02931	Sbc	0.60	103.4	8.73	5.26	8.73	5.20	8.73	1.88	8.73	0.25
31	54	NGC1553	64.04361	-55.78003	S0	0.79	153.1	8.70	5.89	6.21	6.00	2.25	5.38	2.25	4.27
32	52	NGC1399	54.62093	-35.45040	E1pec	0.85	78.0	8.66	5.82	6.73	5.94	2.05	5.71	2.05	4.86
33	533	NGC4236	184.17477	69.46757	SBdm	0.30	158.0	8.66	7.91	8.66	7.99	8.66	5.97	8.66	3.09
34	47	NGC4565	189.08658	25.98755	Sb	0.19	136.3	8.54	5.76	8.54	5.71	8.54	3.21	8.54	1.66
35	17	Maffei2	40.47926	59.60422	Sbc	0.44	27.7	8.50	4.76	8.50	4.58	8.50	1.07	8.50	-1.03
36	60	NGC4631	190.53334	32.54174	SBcd	0.27	83.2	8.27	6.01	8.27	5.80	8.27	1.99	8.27	-0.06
37	33	MESSIER60	190.91643	11.55272	E	0.82	99.3	8.23	5.38	6.28	5.47	2.17	5.04	2.17	3.98
38	65	NGC4636	190.70770	2.68779	E	0.68	147.7	8.06	6.07	6.45	6.17	1.65	6.17	1.65	4.95
39	142	NGC2768	137.90607	60.03756	E	0.32	91.7	7.98	6.76	5.89	6.83	1.80	6.67	1.80	5.62
40	77	NGC3585	168.32115	-26.75477	E	0.57	109.0	7.94	6.28	5.76	6.40	1.34	6.30	1.34	5.35
41	1151	ESO270-G017	203.70584	-45.54919	SBm	0.18	107.5	7.94	8.55	6.05	8.72	6.05	6.27	6.05	3.98
42	24	MESSIER51a	202.46959	47.19518	SABb	0.67	17.6	7.72	5.09	7.72	4.97	7.72	1.19	7.72	-0.61

Table 1 continued

Table 1 (continued)

IS	IB	Galaxy	R.A.	Dec	Morph	ba pa	Rw1	m1 \pm Δ m1	Rw2	m2 \pm Δ m2	Rw3	m3 \pm Δ m3	Rw4	m4 \pm Δ m4
(1)	(2)	(3)	deg	deg	(6)	(7)	(8)	(9)	(10)	(11)	(12)	(13)	(14)	(15)
43	41	NGC3115	151.30800	-7.71870	E-S0	0.56 41.7	7.69	5.59 0.01	5.65	5.64 0.01	1.57	5.47 0.01	1.57	4.61 0.03
44	56	NGC3923	177.75705	-28.80606	E	0.88 40.6	7.66	5.98 0.01	5.89	6.12 0.01	1.32	6.15 0.01	1.32	5.33 0.06
45	76	NGC4365	186.11780	7.31775	E	0.68 35.6	7.53	6.27 0.01	5.48	6.44 0.01	0.85	6.86 0.01	0.85	5.82 0.05
46	136	NGC1313	49.56689	-66.49796	SBCd	0.63 173.3	7.47	6.71 0.01	7.47	6.64 0.01	7.47	3.51 0.01	7.47	1.03 0.01
47	45	MESSIER84	186.26555	12.88707	E	0.97 16.3	7.46	5.73 0.01	5.50	5.82 0.01	1.31	5.81 0.01	1.31	4.87 0.05
48	72	NGC0185	9.74029	48.33795	E	0.74 49.0	7.45	5.01 0.01	7.45	6.34 0.01	2.06	5.52 0.01	2.06	4.65 0.04
49	21	NGC6946	308.71796	60.15392	SABc	0.91 51.5	7.45	6.23 0.01	7.45	4.84 0.01	7.45	0.94 0.01	7.45	-1.04 0.01
50	93	NGC1395	54.62383	-23.02732	E	0.81 146.5	7.42	6.45 0.01	5.63	6.57 0.01	1.32	6.41 0.01	1.32	5.47 0.07
51	25	IC0010	5.07196	59.30388	IBm	0.87 125.8	7.33	5.11 0.01	7.00	5.04 0.01	3.87	2.35 0.01	3.87	-0.33 0.01
52	206	NGC4517	188.18965	0.11525	Sc	0.18 81.9	7.22	7.08 0.01	7.22	6.99 0.01	7.22	3.91 0.01	7.22	2.11 0.01
53	32	NGC1291	49.32742	-41.10804	S0-a	0.98 44.7	7.22	5.35 0.01	7.22	5.39 0.01	7.22	4.30 0.01	7.22	3.10 0.04
54	67	NGC2683	133.17226	33.42194	Sb	0.19 42.0	7.16	6.14 0.01	6.26	6.10 0.01	6.26	3.79 0.01	6.26	2.65 0.02
55	59	NGC4697	192.14961	-5.80060	E	0.81 49.9	7.13	6.00 0.01	5.27	6.10 0.01	1.32	6.02 0.01	1.32	4.81 0.04
56	35	NGC3521	166.45242	-0.03587	SABb	0.62 165.4	7.13	5.44 0.01	4.93	5.38 0.01	4.93	1.98 0.01	4.93	0.33 0.01
57	598	NGC3109	150.79233	-26.16096	SBm	0.31 91.7	7.09	8.00 0.01	7.09	8.01 0.01	7.09	6.66 0.04	7.09	null null
58	39	NGC0891	35.63731	42.34778	Sb	0.25 22.9	7.09	5.51 0.01	7.09	5.30 0.01	7.09	1.97 0.01	7.09	0.23 0.01
59	50	MESSIER85	186.35025	18.19108	S0-a	0.78 18.4	7.09	5.79 0.01	5.76	5.86 0.01	1.73	5.67 0.01	1.73	4.57 0.04
60	340	NGC4244	184.37286	37.80739	Sc	0.19 46.5	7.08	7.51 0.01	7.08	7.46 0.01	7.08	5.34 0.01	7.08	3.27 0.03
61	221	NGC4762	193.23326	11.23105	S0	0.29 27.8	7.08	7.11 0.01	5.16	7.19 0.01	1.61	6.96 0.02	1.61	6.18 0.10
62	155	NGC5084	200.07019	-21.82725	S0	0.40 75.8	6.85	6.83 0.01	6.85	6.84 0.01	6.85	5.53 0.02	6.85	4.16 0.08
63	96	NGC5907	228.97304	56.32876	SABc	0.19 154.3	6.76	6.47 0.01	6.76	6.35 0.01	6.76	3.24 0.01	6.76	1.57 0.01
64	461	NGC4395	186.45364	33.54688	Sm	0.81 144.2	6.72	7.78 0.01	6.72	7.81 0.01	6.72	5.45 0.02	6.72	3.01 0.05
65	71	NGC1407	55.04918	-18.58000	E	1.00 178.7	6.63	6.20 0.01	5.25	6.32 0.01	1.28	6.22 0.01	1.28	5.44 0.07
66	40	NGC3627	170.06262	12.99155	Sb	0.53 177.3	6.59	5.56 0.01	5.16	5.47 0.01	5.16	2.03 0.01	5.16	0.02 0.01
67	148	NGC4438	186.94028	13.00887	Sa	0.44 29.6	6.53	6.79 0.01	5.50	6.81 0.01	1.87	5.32 0.01	1.87	3.82 0.02
68	61	NGC1365	53.40142	-36.14048	Sb	0.60 41.0	6.52	6.03 0.01	6.52	5.74 0.01	6.52	2.11 0.01	6.52	-0.46 0.01
69	42	NGC2903	143.04214	21.50136	Sbc	0.49 21.5	6.48	5.67 0.01	6.48	5.58 0.01	6.48	2.07 0.01	6.48	0.09 0.01
70	87	NGC5846	226.62210	1.60555	E	0.89 51.8	6.46	6.41 0.01	4.64	6.56 0.01	1.17	6.59 0.01	1.17	5.77 0.06
71	66	NGC4725	192.61075	25.50079	SABa	0.63 40.0	6.44	6.09 0.01	5.12	6.15 0.01	5.12	3.99 0.01	5.12	2.62 0.02
72	83	NGC1549	63.93811	-55.59235	E	0.80 5.3	6.43	6.35 0.01	5.68	6.46 0.01	1.90	6.09 0.01	1.90	5.21 0.03
73	1782	WLM	0.49227	-15.46099	IB	0.33 2.9	6.43	8.93 0.01	6.43	9.00 0.01	6.43	8.36 0.20	6.43	5.47 0.26
74	53	NGC2841	140.51106	50.97655	SBb	0.47 151.4	6.41	5.89 0.01	4.93	5.91 0.01	4.93	3.78 0.01	4.93	2.21 0.01
75	14	CircinusGalaxy	213.29146	-65.33923	Sb	0.67 20.9	6.37	4.43 0.01	6.37	3.76 0.01	9.19	-0.29 0.04	8.70	-2.58 0.04
76	82	NGC3621	169.56879	-32.81405	SBCd	0.48 162.0	6.33	6.33 0.02	5.23	6.21 0.02	5.23	2.57 0.01	5.23	0.85 0.01
77	134	NGC5078	199.95856	-27.41013	Sa	0.39 145.7	6.32	6.71 0.01	4.60	6.68 0.01	2.73	4.07 0.01	2.73	2.46 0.01
78	62	NGC1023	40.10017	39.06337	E-S0	0.47 84.0	6.30	6.04 0.01	4.52	6.12 0.01	1.60	5.94 0.01	1.60	5.01 0.05
79	44	NGC7331	339.26675	34.41580	Sbc	0.43 172.0	6.22	5.70 0.01	6.22	5.61 0.01	6.22	2.36 0.01	6.22	0.67 0.01
80	26	MESSIER64	194.18185	21.68300	SABa	0.54 114.7	6.16	5.18 0.01	5.01	5.18 0.01	5.01	2.96 0.01	5.01	1.19 0.01
81	92	MESSIER59	190.50938	11.64700	E	0.76 164.9	6.11	6.45 0.01	4.50	6.74 0.01	1.44	6.20 0.01	1.44	5.23 0.06
82	123	NGC4696	192.20518	-41.31093	E	0.62 97.9	6.07	6.66 0.01	5.06	6.74 0.01	1.62	6.63 0.01	1.62	5.54 0.06
83	11	MESSIER82	148.96646	69.67978	S?	0.79 54.1	6.06	4.07 0.01	6.06	3.61 0.01	8.01	-0.96 0.01	8.49	-4.14 0.01
84	538	ESO274-001	228.55611	-46.80931	SAd	0.16 36.6	5.91	7.91 0.01	5.91	7.93 0.01	5.91	6.94 0.08	5.91	3.04 0.02
85	15	MESSIER77	40.66975	-0.01340	Sb	0.87 80.2	5.87	4.59 0.01	4.73	2.89 0.01	5.91	-0.68 0.04	6.32	-2.45 0.04
86	149	NGC3077	150.82985	68.73387	S?	0.73 38.5	5.84	6.80 0.01	4.51	6.76 0.01	2.64	4.12 0.01	2.64	1.64 0.01
87	55	MESSIER65	169.73309	13.09245	Sa	0.34 171.3	5.84	5.90 0.01	4.91	5.92 0.01	4.91	4.16 0.01	4.91	2.78 0.02

Table 1 continued

Table 1 (*continued*)

iS	iB	Galaxy	R.A.	Dec	Morph	ba pa	Rw1	m1 \pm Δ m1	Rw2	m2 \pm Δ m2	Rw3	m3 \pm Δ m3	Rw4	m4 \pm Δ m4
(1)	(2)	(3)	deg	deg	(6)	(7)	amin	mag	amin	mag	amin	mag	amin	mag
88	98	NGC7213	332.31741	-47.16676	Sa	0.97 174.6	5.83	6.48 0.01	3.99	6.47 0.01	2.21	4.36 0.01	2.21	2.48 0.01
89	49	IC0356	61.94514	69.81254	Sb	0.72 103.0	5.80	5.76 0.01	4.98	5.78 0.01	4.98	3.78 0.01	4.98	1.95 0.02
90	1213	NGC1560	68.20547	71.88394	Scd	0.22 24.4	5.79	8.59 0.01	4.51	8.75 0.01	1.56	7.71 0.04	1.56	5.55 0.04
91	74	NGC2663	131.28387	-33.79462	E	0.65 112.2	5.78	6.26 0.01	5.03	6.36 0.01	1.22	6.45 0.01	1.22	4.95 0.03
92	85	NGC4216	183.97667	13.14956	SABb	0.26 20.7	5.77	6.36 0.01	4.71	6.38 0.01	4.71	4.24 0.01	4.71	2.89 0.02
93	143	NGC1055	40.43828	0.44376	SBb	0.30 103.8	5.69	6.76 0.01	5.69	6.64 0.01	5.69	3.08 0.01	5.69	1.32 0.01
94	303	NGC5170	202.45326	-17.96646	Sc	0.17 127.3	5.67	7.43 0.01	4.74	7.41 0.01	4.74	5.24 0.01	4.74	3.79 0.02
95	135	MESSIER98	183.45123	14.90056	SABb	0.28 155.7	5.64	6.71 0.01	5.64	6.67 0.01	5.64	3.83 0.01	5.64	2.21 0.02
96	68	NGC2997	146.41144	-31.19094	SABc	0.78 99.2	5.62	6.15 0.01	5.62	6.03 0.01	5.62	2.35 0.01	5.62	0.54 0.01
97	101	NGC4125	182.02449	65.17439	E	0.71 83.9	5.61	6.50 0.01	4.03	6.59 0.01	1.44	6.27 0.01	1.44	5.20 0.04
98	102	NGC7793	359.45728	-32.59102	Scd	0.62 97.9	5.60	6.52 0.01	5.60	6.43 0.01	5.60	3.21 0.01	5.60	1.55 0.01
99	108	NGC5363	209.03012	5.25490	S0-a	0.68 124.6	5.60	6.57 0.01	4.06	6.63 0.01	1.49	5.69 0.01	1.49	4.36 0.02
100	245	NGC4217	183.96248	47.09152	ZZZ	0.17 49.3	5.59	7.23 0.01	4.20	7.09 0.01	4.20	3.74 0.01	4.20	2.07 0.01
-	1081	IC1613	16.20089	2.11914	IBm	0.90 135.4	4.69	8.49 0.01	4.69	8.69 0.01	null	null null	null	null null
-	22	MESSIER32	10.67439	40.86511	E	0.86 165.8	3.62	5.02 0.01	2.95	5.07 0.01	2.95	4.42 0.01	2.95	3.61 0.04
-	3902	UGC05373	149.99974	5.33153	IB	0.75 97.0	2.89	9.76 0.01	1.76	10.04 0.02	null	null null	1.76	6.69 0.35
-	8996	ESO245-007	27.77698	-44.44341	Sm	0.81 11.2	2.18	11.06 0.01	2.18	11.28 0.04	null	null null	null	null null

NOTE—columns: (1) order of W1 $3.4\mu\text{m}$ angular size; (2) order of W1 brightness; (3) Galaxy name; (4, 5) J2000 coordinates; (6) RC3 Hubble Type; (7) axis ratio and position angle (degrees, E of N); (8) W1 angular semi-major axis (arcmin); (9) W1 magnitude and associated error; (10) W2 angular semi-major axis (arcmin); (11) W2 magnitude and associated error; (12) W3 angular semi-major axis (arcmin); (13) W3 magnitude and associated error; (14) W4 angular semi-major axis (arcmin); (15) W4 magnitude and associated error. The following galaxies had saturated cores, necessitating recovery of lost flux: M 82, NGC 253, Circinus, NGC 1068 (M77), and NGC 2070 (LMC).

In the following sections, we compare the properties of the largest galaxies, including their derived physical properties (size, mass and star formation). For some context, we also consider their mass and star formation properties relative to a large spectroscopic survey of local universe galaxies (Jarrett et al. 2017).

4. PHOTOMETRIC PROPERTIES OF THE LARGEST GALAXIES

In this section we present the source characterization for 100 largest galaxies, including isophotal and total flux measurements, colors, surface brightness and bulge-to-disk comparisons.

4.1. Measurements of Integrated Flux and Radial Flux Distribution

Isophotal fluxes are derived from the W1 ($3.4\ \mu\text{m}$) $1\text{-}\sigma_{\text{sky}}$ isophote ($\sim 23\ \text{mag arcsec}^{-2}$) fit with an elliptical aperture whose shape (axis ratio and position) was determined at higher S/N ($3\text{-}\sigma_{\text{sky}}$) and, for simplicity, assumed constant orientation throughout all radii. Total fluxes are estimated in two different ways: (1) asymptotic apertures and (2) by fitting the axisymmetric radial flux distribution; see below.

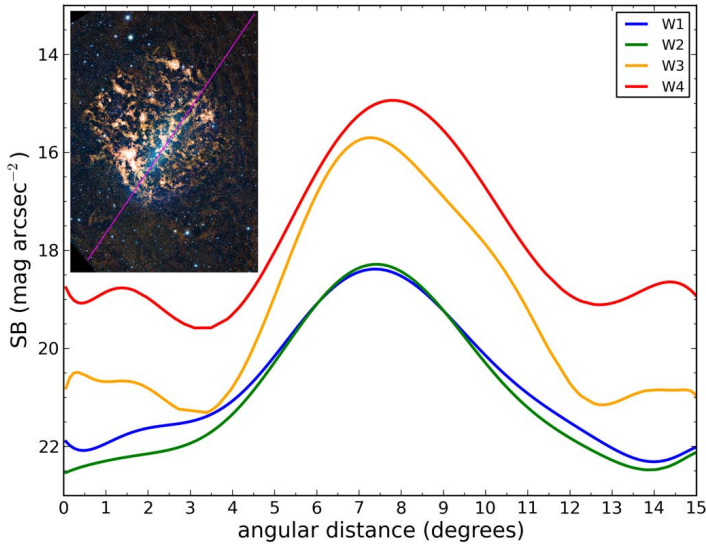


Figure 4. Mean surface brightness slice through the bar and central region of the LMC. The slice starts in the lower left of the LMC (see inset, magenta line), and extends 15 degrees ($\sim 15.7\ \text{kpc}$) diagonally along the stellar bar. The mean surface brightness at $100\times 100\ \text{pc}$ scale is first computed, followed by fitting an 11th order Legendre polynomial to produce the smooth (large-scale) result shown here. The stellar bar surface brightness (W1) peaks at (05:25:36, -69:49:34) J2000 coordinates.

The angular size distribution ranges from 11 arcmin in diameter, to the extreme ~ 10 degree size of the LMC.

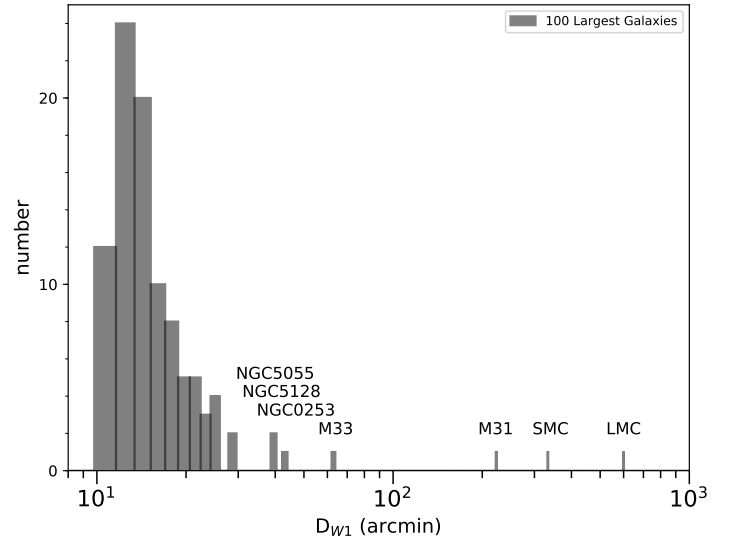


Figure 5. Angular diameter size distribution of the 100 largest galaxies based on the *WISE* W1 imaging. The size metric is from the $1\text{-}\sigma_{\text{sky}}$ ($\sim 23\ \text{mag arcsec}^{-2}$) isophotal semi-major axis (R_{W1}). The largest are the Local Group galaxies, followed by the nearest galaxy groups, (NGC 253; Cen A), all within a few Mpc from the Milky Way.

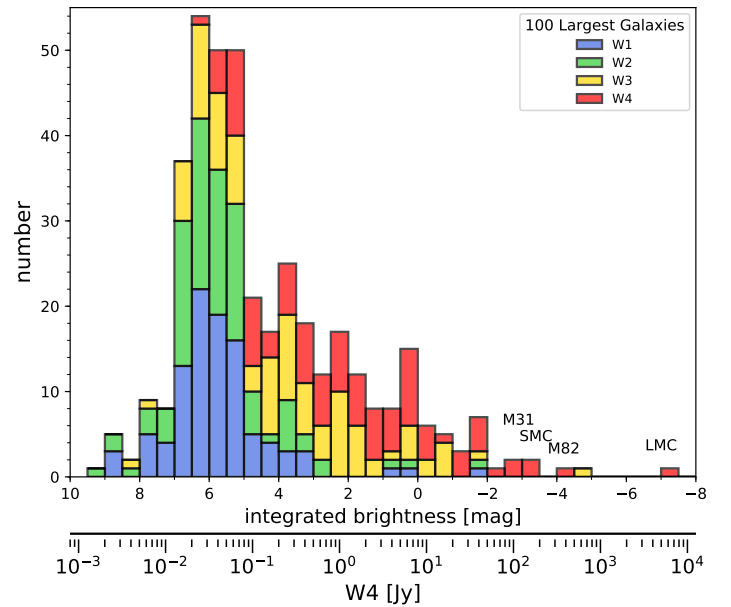


Figure 6. Stacked histogram showing the integrated brightness distribution for the four *WISE* bands based on the isophotal measurements. The brightest galaxies in W4 ($22\ \mu\text{m}$) are indicated, with the W4 flux density (in Jansky units) scale given for comparison to the magnitudes. The LMC is the brightest owing to its proximity (50 kpc), but here the outstanding galaxy is M 82, whose starburst is creating so much light in the infrared ($\sim 360\ \text{Jy}$) that it saturates in *WISE* (and *Spitzer*) imaging.

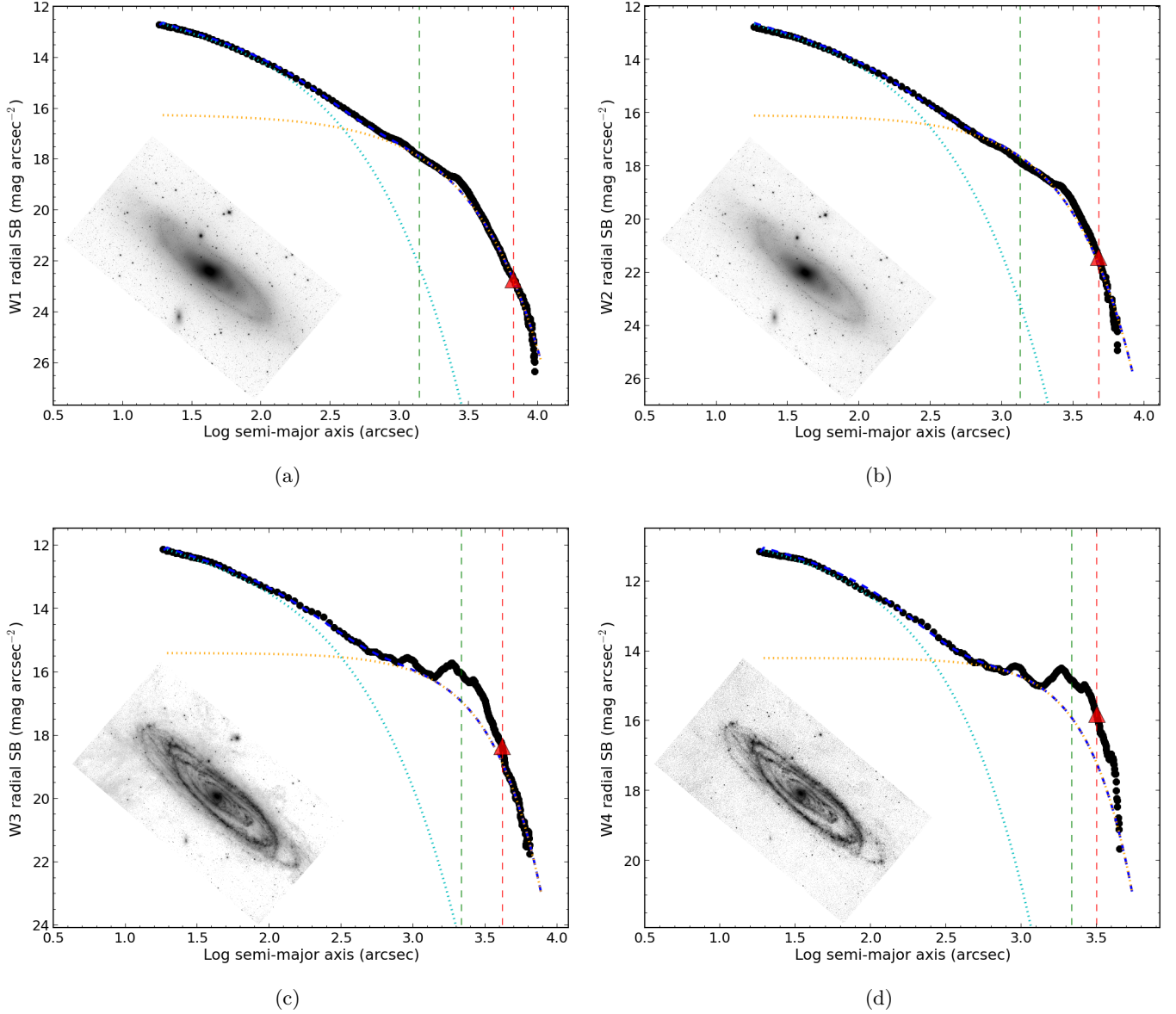


Figure 7. Axi-symmetric radial profiles of M31 as measured for the four bands of *WISE*. The data measurements are indicated with black points, extending well beyond the $1\text{-}\sigma_{\text{sky}}$ isophotal radius (demarcated by the red triangle and dashed red line) into the single pixel noise. The half-light radius is indicated by the green dashed line. The data are fit with a double Sérsic profile consisting of the inner bulge (blue dotted line) and the disk (orange dotted line). The W1 B/T ratio is 0.67, indicating a prominent bulge. The inset figure shows the galaxy in the individual monochromatic band. Note that at the longer wavelengths, the assumption of axi-symmetry and smoothness is no longer valid due to the spiral arms and star formation regions.

In fact, the size of the LMC is difficult to determine; it is neither symmetric in shape, nor does it have an easily-characterized radial distribution, as demonstrated in Figure 4. Here, slicing along the stellar bar, with lower-left endpoint (06:51:19, -71:32:57) to upper-right endpoint (04:14:11, -65:19:19), perpendicular width of 100 pc (5.7 arcmin) and stretching 15 degrees in total angular extent, the mean surface brightness is computed in 100×100 pc blocks along the profile. Fitting a high-order polynomial to the distribution produces a smoothed rep-

resentation of the mean surface brightness (Fig. 4). The stellar bar is evident in all four bands, peaking at J2000 position (05:25:36, -69:49:34), and extending *at least* ± 5 degrees to the nominal background level. As noted in the previous section, there is significant structure in the local background to the Magellanic Clouds, including the N-S “river” filament, which complicates the LMC characterization; consequently, the size and integrated flux measurements carry this additional uncertainty.

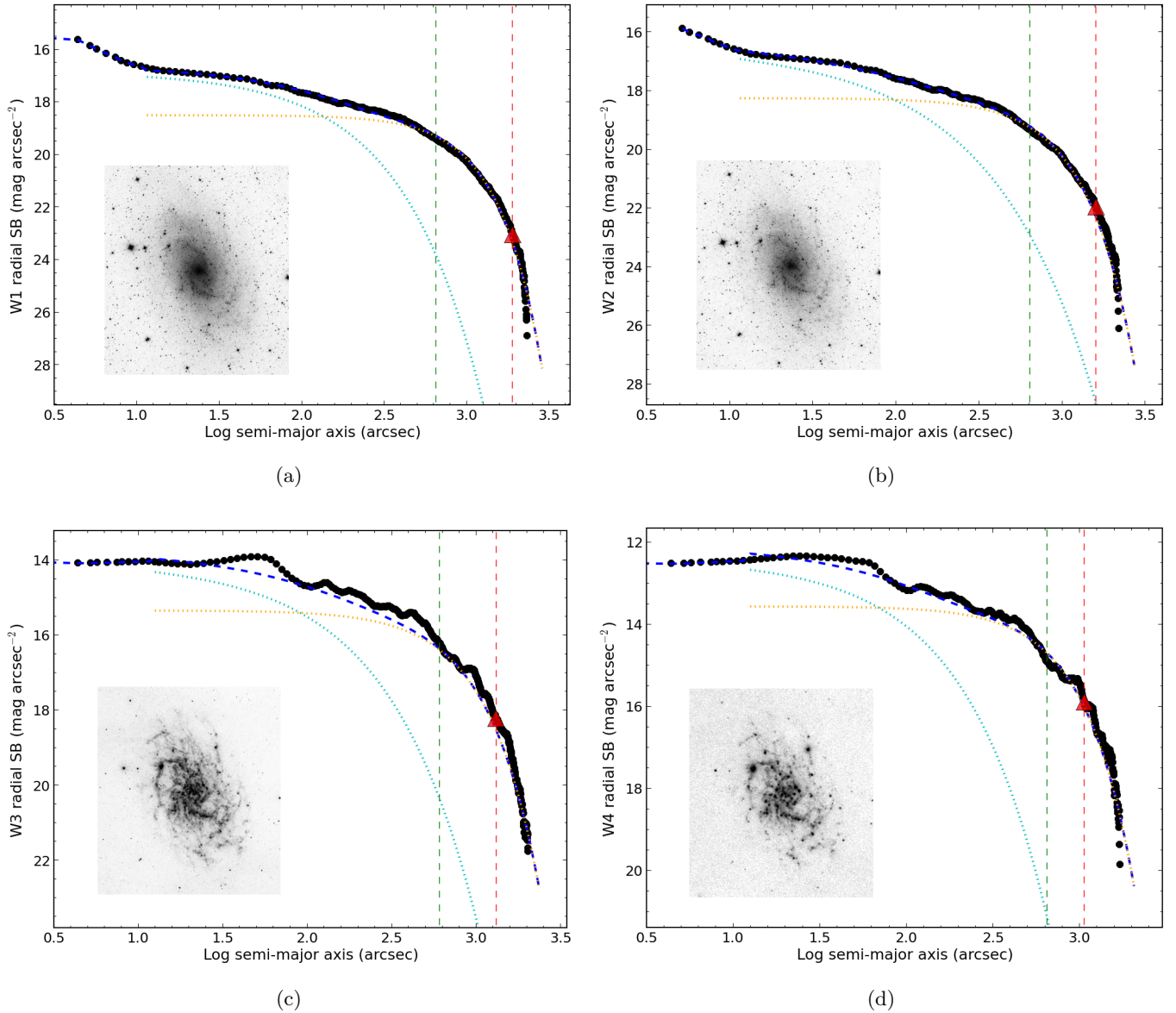


Figure 8. Axi-symmetric radial profiles of M33 as measured for the four bands of *WISE*. See Fig. 7 for details. The W1 B/T ratio is 0.33, indicating a prominent disk compared to the bulge population (compare with the bulge galaxy, M31).

The mode of the size distribution, Figure 5, is about 13 arcmin in diameter. Other notably large galaxies include bright radio galaxy Cen A (NGC 5128), nearby nuclear starburst NGC 253, and the big-four LG galaxies. The integrated flux ranges across ~ 7 magnitudes for W1 and W2, but also an incredible 13-14 magnitudes for W3 and W4 due to the extremes in SF activity traced in these mid-IR bands (notably, M82 makes a strong appearance); see Figure 6.

Total fluxes are estimated using both radial surface profile fitting and maximal curve-of-growth ‘asymptotic’ apertures. The latter is simply a large aperture that represents the maximum flux achieved through radial

curve of growth within the error tolerance. This aperture is less than the background annulus radius since it will converge before reaching the background level. It has some advantages, including both simplicity and robustness for smaller angular-sized galaxies. On the other hand, it is susceptible to background gradients (e.g., nearby bright stars) and unsubtracted foreground stars – both of these effects can be systematic and are especially problematic for very large galaxies. Asymptotic magnitudes are a common method for estimating the total flux, having been used in many studies; e.g., Neil et al. (2014) used them for a large *WISE* sample Tully-Fisher relation study. The other method to esti-

mate the total flux comes from a technique developed for 2MASS (Jarrett et al. 2000), by fitting a Sérsic profile to the axi-symmetric radial profile. Since the mid-infrared (mid-IR) includes both a bulge and disk (SF) component, we employ a double Sérsic to better fit the distribution. We demonstrate the performance of the fitting for M31 and M33 in Fig. 7 and Fig. 8 showing log-log plots of the radial surface brightness. The measured surface brightness as a function of radius (in symmetric shells) is denoted by the filled points, starting at a radius well beyond the PSF ($\sim 15''$) and extending several degrees (in the case of M31), to well beyond the $1-\sigma_{\text{sky}}$ isophotal limit (denoted by the red triangle), to depths of around 26 mag arcsec $^{-2}$ (or about 28.7 mag arcsec $^{-2}$ in AB). The Sérsic fit is shown with the blue dotted curve (bulge component) and the orange dotted curve (disk component).

Table 2. Comparison between Total and Asymptotic Magnitudes

<i>WISE</i> Band	[Total - Asymptotic] Magnitudes		
	Ave mag	Median mag	St. Dev mag
W1	-0.01	-0.01	0.01
W2	-0.01	-0.01	0.01
W3	+0.05	-0.01	0.15
W4	-0.06	-0.06	0.05

NOTE—The sample consists of the 100 largest galaxies (with the exception of the Magellanic Clouds, which are not relevant here); the values correspond to the total minus the asymptotic magnitudes, where the total is estimated using a double-Sersic fitting to the radial surface brightness profile.

Integrating out to three disk scale lengths beyond the $1-\sigma_{\text{sky}}$ isophotal limit, a radius of about 2.8 degrees for M31 and 0.8 degrees for M33, the total integrated flux (isophotal flux + extrapolation) for the four bands of *WISE* is 0.063, 0.104, -1.997, -3.132 mag, and 3.078, 3.020, -0.217, -2.015 mag for M31 and M33, respectively. Comparing to the asymptotic aperture measurements, the M31 and M33 radii are 2.49 and 1.08 degrees respectively, with fluxes 0.078, 0.127, -1.950, -3.111 mag, and 3.032, 3.003, -0.174, -1.945 mag, respectively. For these two LG galaxies, both total flux estimates appear to agree to better than 5%. Likewise, comparing the total fluxes from the two methods for the 100 largest galaxies we find that there is very good correspondence, $\sim 1\%$, for the sensitive *WISE* bands (W1 and W2), and 5 to 6% for the W3 and W4 bands; see the tabulated statistical results in Table 2. Interestingly there is a systematic in the median distribution, with profile fitting giving slightly (1%) brighter results in comparison to asymptotic apertures, likely because the fitting goes beyond the image noise to capture more flux. The ex-

ception is with W3, where the average (not the median) is skewed towards brighter fluxes. Visual inspection of galaxies with large discrepancies between the two methods reveals that early-type galaxies with very little W3 emission (because only R-J stellar emission is seen for these types) have poor radial fits which do not extend much beyond the R_{W1} radius. It would appear that the asymptotic fluxes are more robust under these conditions, notably when the S/N is poor for radial fitting much beyond the $1-\sigma_{\text{sky}}$ limit. We list the total photometry results for the largest 100 galaxies, including the radial profile fitting and the asymptotic, in Appendix Table A1. We will investigate the total flux differences in more detail and statistical clarity in Paper II when we include a much larger sample.

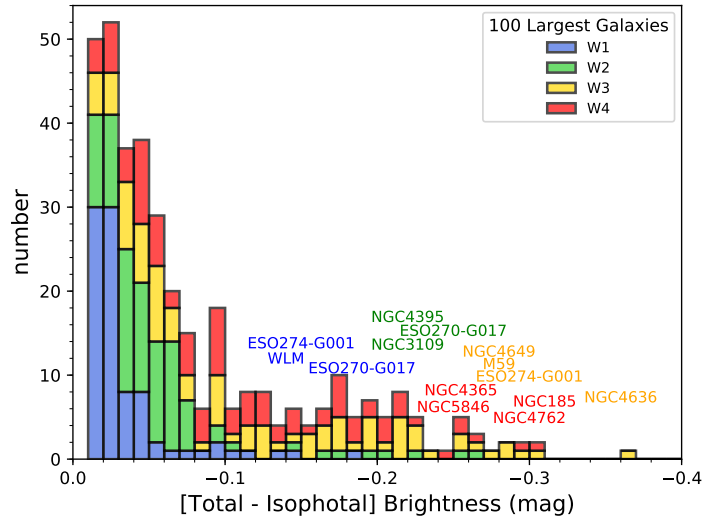


Figure 9. Comparison of the total versus isophotal brightness for all four *WISE* bands. It is notable that W1 isophotal and total fluxes are within 5% of each other, indicating the depth of the $1-\sigma$ photometry. Outliers are indicated: low surface brightness galaxies tend to have large deviations for W1 and W2, early-types (spheroids) for W3 and W4.

Next, comparing the total fluxes from the radial fitting method to the $1-\sigma_{\text{sky}}$ isophotal fluxes, these total values are only 1.5, 2.3, 4.4 and 4.1% brighter for bands W1, W2, W3 and W4, for M31, and 1.5, 0.5, 5.2, 7.6% for M33. There is relatively little flux beyond the W1 and W2 isophotes, as demonstrated in Figure 9, which shows the difference (in magnitudes) between the total and isophotal mags for the largest galaxies. For the most part, the total flux is within 4% of the isophotal flux for W1 and 6% for W2. The exceptions ($>20\%$) tend to be very low surface brightness galaxies (e.g., WLM and ESO 270-G017), in which there may be a significant component just below the $1-\sigma_{\text{sky}}$ noise per pixel.

For the long wavelengths, W3 and W4, we observe a different behaviour. The isophotal-to-total correction has a larger spread, easily ranging out to 25% or more, with the largest deviations occurring for early-type galaxies (e.g., Maffei 1; NGC 4406; NGC 4762), in which there is little emission in the W3 and W4 bands, only stellar (R-J) emission, and hence these bands miss a large fraction of the stellar and ISM light. Consequently, total flux measurements (either asymptotic or profile-fitting) are important for these bands when, e.g., measuring the global star formation rate; see next section.

4.2. Color Classification of the Largest Galaxies

Similar to optical color analysis of galaxies (e.g., the red and blue sequence, green valley), mid-IR color diagnostics have proven to be useful in classifying the activity of galaxies, at least crudely separating quiescent, SF, and AGN populations (Lacy et al. 2004; Jarrett et al. 2011; Stern et al. 2012; Yan et al. 2013; Cluver et al. 2014, 2017), and as well for radio galaxy types (Ching et al. 2017; Jarrett et al. 2017). Here we consider the galaxy colors after correcting for spectral redshift using a diverse set of templates compiled by Brown et al. (2014a) fit to the 2MASS XSC (Jarrett et al. 2003) plus *WISE* photometric SED measurements from this work; the templates and fitting method are detailed in Jarrett et al. (2017), and some example SED templates with photometric fits given in Appendix B.

The color-color location for the largest 100 galaxies is presented in Figure 10. For comparison and context, we show the *WISE* rest-frame-corrected colors for the ~ 5000 brightest galaxies in the WXSC, to be presented in detail in Paper II. The largest galaxies, with their corresponding high signal to noise measurements, define a tight track within the color-color distribution of bright (low-redshift) WXSC galaxies (grey contours). The track ranges from mid-IR ‘blue’ stellar-dominated galaxies to mid-IR ‘red’ or dusty, star-forming galaxies, with approximately four magnitudes of delineation in the W2–W3 color. Along the W1–W2 (Y-)axis, the trend is for the color to ‘warm’ as the SF, or alternatively AGN, activity increases. In the case of the largest galaxies, this spans approximately 0.4 magnitudes.

We use the rest-frame-corrected measurements from largest and highest S/N galaxies to fit the functional form of this *WISE* color-color “sequence”, given by:

$$(W1 - W2) = [0.015 \times e^{\frac{(W2-W3)}{1.38}}] - 0.08, \quad (1)$$

The track is roughly flat with W2–W3 color, curving upwards (in W1–W2 color) for the dusty, star-forming galaxies. This curvature can be understood as

warm dust from active star-formation elevating the W2 (4.6 μm) band relative to the bluer W1 (3.4 μm) band. For example, the starburst galaxy M82 with a steeply rising mid-IR continuum exhibits a warmer W1–W2 color – by 0.5 magnitudes – compared to the early-type spiral galaxy M31. More extreme galaxies, including luminous infrared galaxies and AGN lie well above this SF track, separating normal galaxies from active systems.

Considering just the 100 largest galaxies, there are several notable outliers: starburst M82 has the reddest W2–W3 color of the sample, indicative of its active SF, while the two AGN of the sample, Circinus and NGC1068, have very warm W1–W2 colors, a signature of AGN torus-dust heating. In fact, NGC 1068 is so warm, W1–W2 ~ 1.7 mag, it falls near the extreme limit of the AGN-QSO zone defined in Wright et al. (2010) and Jarrett et al. (2011). NGC 1068 (M77), classified as a Seyfert-2 LIRG, is not only exceptional given its close proximity to the Milky Way (~ 10 Mpc), but is clearly an outlier compared to other galaxies in the local universe as the grey contours ($z < 0.3$) are tracing, and the higher redshift galaxies (> 0.3) with luminous AGN appearing in significant numbers (the magenta contours).

Following the prescription of Jarrett et al. (2017), we have divided the color-color plane into four zones that are inspired by infrared morphology considerations of bulge, disk and nuclear stellar populations (Johnson et al. 2007; Walker et al. 2010; Jarrett et al. 2011, 2013, 2017).

The early-type (spheroids; E/S0) have ‘blue’ colors, W2–W3 < 1.5 mag. They are characterized by prominent bulges with stellar-dominated mid-IR emission arising from evolved (luminous) stars (see also next section, bulge-to-disk measurements). They are some of the most massive and brightest galaxies in the mid-IR (see below), and tend to be located in dense environments: brightest cluster galaxies, such as Fornax A (NGC 1316), Virgo A (M87) and many of the bright Virgo Cluster galaxies, live in this zone. Since they tend to have little SF activity (unless undergoing a gas-rich ‘wet’ merger or accretion event, consider the infrared excess in the core of Fornax A, Asabere et al. 2016), they are often difficult to detect in W3 and W4 because of the rapidly diminishing R-J tail, and hence only nearby examples can be detected in all three *WISE* W1, W2, W3 bands, rendering a distance selection bias when studying these objects with *WISE* colors, also noted in Jarrett et al. (2017).

In contrast, active SF galaxies, W2–W3 > 3 mag, have bright W3 emission and are easily detected in all four bands. Here we find the late-type disks that have ongoing SF (e.g., M83), and starbursting galaxies (M82,

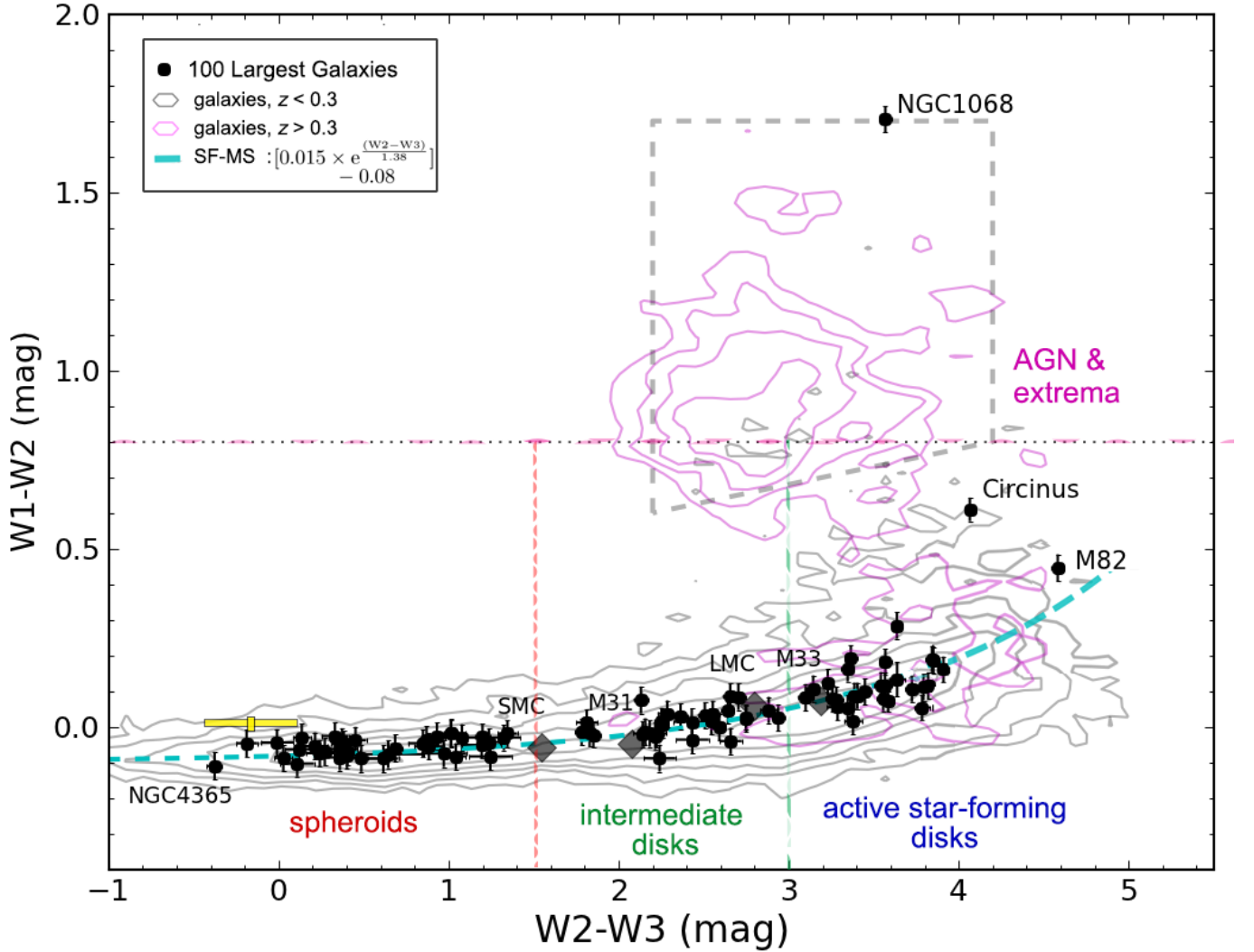


Figure 10. *WISE* colors of the 100 largest galaxies. The diagram attempts to delineate galaxies into four major groups: spheroid-dominated, intermediate disk, star-formation dominated, and AGN-dominated populations. The polygon dashed box is the AGN/QSO region defined in (Jarrett et al. 2011). For comparison, the color distribution for ~ 5000 WXSC (nearby, bright) galaxies is shown with the grey contours, and a set of WXSC galaxies that are at higher redshift ($z > 0.3$), which accentuates the AGN and luminous (starbursting) types. We have defined a “star formation sequence” (cyan dashed line) in which normal galaxies – from quiescent to active SF – follow a track in this infrared color-color space. The yellow-cross, to the left, represents the mean colors and range of the brightest globular clusters, presented in Section 7.

NGC 253, NGC 1365). Intermediate between the gas-depleted galaxies and the SF galaxies, $1.5 < W2-W3 < 3.0$ mag, are the early-type spirals (e.g., M 81, M 31, Milky Way) characterized by prominent bulges, semi-quiescent SF-disks and pseudo-bulges. Some of these galaxies may be undergoing quenching due to environmental effects, and maybe likened to ‘green valley’ populations seen in the optical and infrared (e.g., Johnson et al. 2007; Walker et al. 2010; Cluver et al. 2013).

The final demarcation is for the extrema populations, QSOs and various flavors of mid-infrared AGN activity, including high excitation, broad-line radio galaxies (HERGs and AeBs). Those whose hosts are completely

dominated by AGN emission tend to have $W1-W2$ colors greater than 0.8 (Stern et al. 2012), while some Seyferts may lie below this line (e.g., Circinus) chiefly due to strong host SF emission, comparable to the AGN itself (For et al. 2012). In order to track Circinus as an AGN (Seyfert 2), we relax the $W1-W2$ threshold to a value of 0.5 mag in order to include Circinus in the AGN group (along with NGC 1068). Current studies of AGN and X-ray/ infrared colors (Mingo et al. 2016; Huang et al. 2017) seem to indicate that Seyferts and low-power AGN can have $W1-W2$ colors well less than the 0.8 demarcation (e.g., 0.3 to 0.8), but still well above the SF track (Eq. 1).

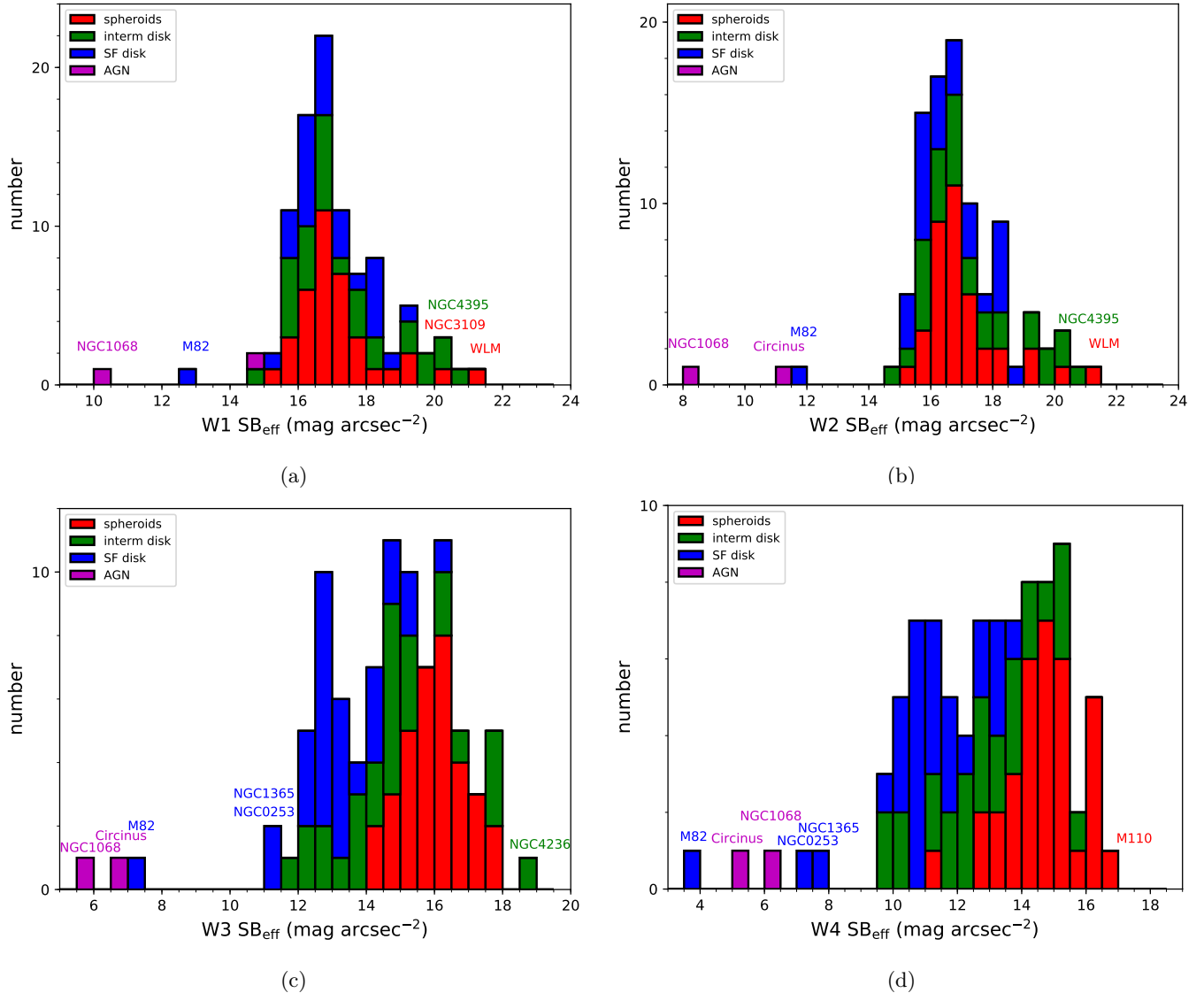


Figure 11. Half-light surface brightness (SB_{eff}) for the 100 largest galaxies based on the four bands of *WISE*. The galaxies are group-delineated by their *WISE* colors (see Fig. 10), with notably bright and faint galaxies labeled, with four-band standouts NGC 1068, Circinus and M82.

Colors broadly reveal spectral features and continuum trends. The actual mid-IR spectra for galaxies are far richer, encoding the early-to-late star-formation histories. Examples of the broad *WISE* color classification are shown in Appendix B, where the SEDs reveal the rich emission features for each color class.

4.3. Surface Brightness

Employing the color classification, we investigate the half-light surface brightness, SB_{eff} , of the sample. The half-light, or effective radius is derived from the total flux measurement, and corresponds to the radius at which half of the total light is enclosed within the ellipsoidal shape of the galaxy. This radius can be com-

promised by the relatively large *WISE* PSF for small galaxies, but in the case of the largest galaxies in the sky, the radius is well-determined. The effective surface brightness is the half-light flux normalized by the encompassed area. This distant-independent value is sensitive to the Hubble Type, with bright surface brightnesses attributed to early-type bulge-dominated systems, and conversely, late-type spirals have relatively faint surface brightnesses.

The resulting half-light surface brightness for the 100 largest galaxies is presented in Figure 11, which includes panels for each photometric band. In the stellar bands, W1 and W2, there are a number of sources with brightnesses between 16 and 17 mag arcsec^{-2} , for

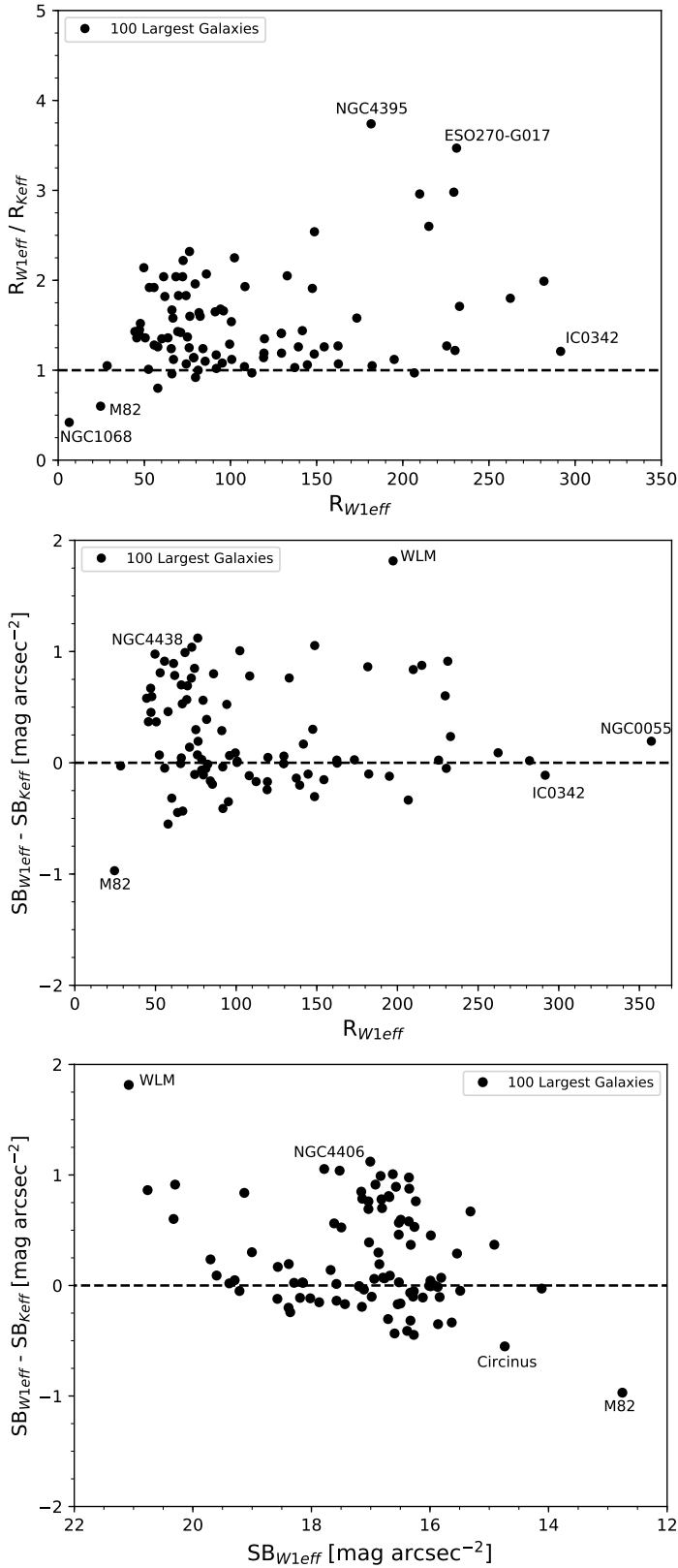


Figure 12. Half light radius (top panel) and surface brightness (bottom two panels) comparison between *WISE* W1 and 2MASS K_s -band. $W1[3.4\ \mu\text{m}]$ is much more sensitive than 2MASS $K_s[2.17\ \mu\text{m}]$ -band, and hence it has much larger radii (and fainter SBs) for dwarf (low-SB) and early-type galaxies.

all classification types, with more subtle delineations following the expected trends: spheroids are typically brighter than SF disks, although there is a distinct population of spheroids that have low values, these are the dwarf spheroidals (see below). Intermediate disk galaxies have the largest spread in surface brightness, 15-20 mag arcsec⁻², and finally, the brightest galaxies by several orders of magnitude are the AGN and nuclear starburst galaxies. The faintest galaxies are the low surface brightness (LSB) dwarfs (hence, their moniker), including the ghostly ESO 245-007.

More diversity is evident in the dust emission-sensitive bands of W3 and W4 (Fig 11c,d). Spheroidals are now the faintest galaxies, and as noted previously, can be difficult to detect in the long wavelength channels of *WISE*. Not surprisingly, the brightest galaxies are the active SF galaxies (e.g., M 82, NGC 0253, NGC 1365) and the AGN ‘extrema’ (NGC 1068 and Circinus). Intermediate disks again have a broad range in values, indicating both semi-quiescent (low SB_{eff}) and high SF (high SB_{eff}) populations, but truly fill the ‘gap’ between ‘dead’ and SF galaxies, notably in the warm dust continuum band of W4 (Fig. 11d).

It is instructive to compare the *WISE* half-light measurements with those from the 2MASS Large Galaxy Atlas (LGA) from Jarrett et al. (2003). It has already been noted that *WISE* isophotal radii are 2 to 5 times larger than those from the LGA, and hence capturing more of the total light, notably for low surface brightness (dwarf) galaxies and for early types with $R^{1/4}$ profiles. For these cases, we would expect half-light radii to be correspondingly larger, and surface brightnesses to be fainter. Fig. 12 presents the comparison of (effective) half-light radii and surface brightness between the *WISE* and 2MASS measurements. The top panel shows the results for the half-light radii; the dashed line shows the expected 1:1 correspondence if all things were equal. The bottom panels show the effective surface brightness comparison with the dashed line representing equal half-light surface brightness. What we see is that *WISE* $3.4\ \mu\text{m}$ half-light radii are, nearly all, much larger than those from the $2.2\ \mu\text{m}$ imaging, and in some extreme cases reach nearly 4 times larger, corresponding to the lowest SB galaxies (note bottom panels), thus demonstrating the relatively poor sensitivity of the LGA to dwarf galaxies (e.g., WLM and ESO270-G017). Similarly, for the large and extended early-type galaxies, such as NGC4406, *WISE* detects far more total emission, giving rise to larger half-light radii and fainter surface brightnesses. Interestingly, for the nuclear active galaxies – starburst M82 and AGN Circinus and NGC1068 – the *WISE* half-light radii are smaller (more compact)

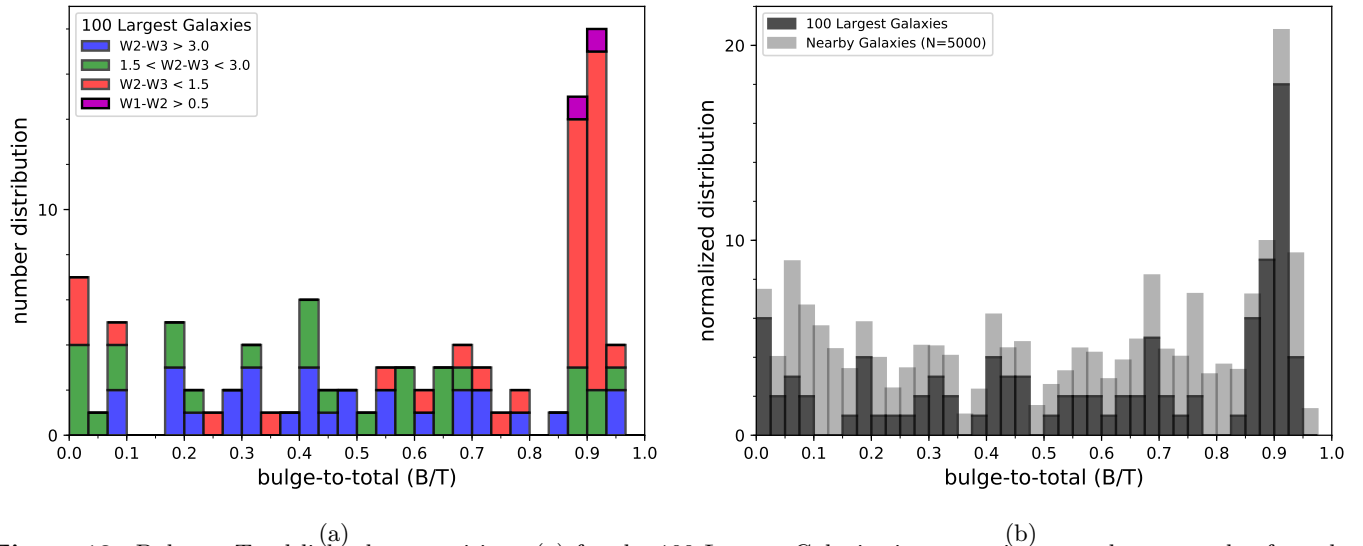


Figure 13. Bulge-to-Total light decomposition. (a) for the 100 Largest Galaxies in comparison to a large sample of nearby galaxies in the *WISE* Extended Source Catalogue. The bulge and disk properties are derived from the axi-symmetric radial profile fit with a double Sérsic Function. Disk and spheroidal properties are correlated with W2-W3 color: blue galaxies tend to have high B/T ratios, while red (SF) galaxies have considerably lower ratios. It should be noted that the largest galaxies have a strong peak at $B/T \sim 0.9$, which is not as apparent in a large sample of nearby galaxies (see panel b).

and significantly higher SB (1 to 3 magnitudes, see bottom panels, Fig. 12) compared to 2MASS – likely due to less extinction in the longer *WISE* bands and the SED differences between the $2.2 \mu\text{m}$ and $3.4 \mu\text{m}$ bands (see e.g., the SEDs in Fig 20, note the steep index power-law distribution for NGC1068).

4.4. Bulge and Disk Populations

On scales of kpc, well-resolved galaxies exhibit aggregate stellar populations that are typically decomposed into disk and bulge populations, which are distinct, not only in their spatial distribution, but also mean age, mass, and luminosity characteristics. The near- and mid-infrared are sensitive to cooler populations of dwarf and giant stars, which dominate the total stellar mass of the host galaxy. For the *WISE* colors, we have sub-divided the W2–W3 color to represent bulk populations, from spheroidal (early-type, typically the oldest populations), intermediate disks and young spiral galaxies, which in principle should be reflected in the light coming from the separate bulge and disk populations (see previous section on the infrared color-color diagram).

Here we employ a very simple decomposition based on axi-symmetry and a double Sérsic fit to the W1 ($3.4 \mu\text{m}$) radial profile. The inner profile represents the bulge population, constrained by a (relatively high) Sérsic index that may range between 2 and 4, and a smaller scale length relative to the disk. The disk component has an index between 0.8 and 2 (the ideal being a perfect exponential, index of 1). An example of a radial de-

composition can be seen in Figure 7, showing the bulge and disk populations of M31, which has a bulge-to-total ratio (B/T) of 0.67.

Figure 13a presents the bulge-to-total ratios for the 100 largest galaxies, coded by their W2–W3 global colors and normalized to show relative differences. The strongest trend is for the early-types, which have a strong peak at high (~ 0.9) B/T ratio, consistent with their dominant (global) spheroidal population. The two AGN in the sample also have a high ratio due to the unresolved nucleus emitting at mid-infrared wavelengths from hot dust accretion, thoroughly dominating the total light (see Fig. 11 showing the effective surface brightness). Much less defined, the late-type spirals (W2–W3 > 3 mag) range across the B/T scale, and similarly with the intermediate disks; only a slight trend towards lower B/T is seen for the more SF-active galaxies. At face value, the B/T clearly delineates the early-type spheroids, but seems to have less power in decomposing the stellar populations in the more active (and presumably disky) galaxies, perhaps confusing the (low scale-height) pure disk, (larger scale-height) thick disk and pseudo-bulge populations that would comprise the SF-color galaxy set.

We compare the B/T of the 100 largest galaxies with that of the nearby-galaxy WXSC, notably the 5000 brightest galaxies (all at low redshifts, $z < 0.1$), in Fig 13b, again normalized to show relative differences across the range. The only difference between these two samples is that the 100 largest are the most well re-

solved, while the 5000 brightest may not always clearly resolve the different stellar populations. We would expect little difference between the two sets; however, we see that the nearby galaxy sample does not have the prominent peak at $B/T=0.9$, while it does have a relative excess at low B/T , disk galaxies with 0.05 to 0.2 in ratio. Either the larger nearby sample has a statistically significant set of disk galaxies (relative to the 100 largest), or conversely, the 100 largest sample is dominated by bulgy galaxies, or there is some biased difference, perhaps related to angular resolution. The 100 largest is biased in the sense that we have chosen those with the largest angular extents, which could very well be the spheroidal galaxies whose $R^{\frac{1}{4}}$ light distribution is detectable at larger angular scales compared to disks with exponential light fall-off. We will investigate the B/T properties of the nearby galaxies in Paper II, creating sub-samples that do not have such angular biases.

5. DERIVED PHYSICAL PROPERTIES: SIZE, MASS AND SFR

Physical parameters presented in this section are derived from the isophotal measurements presented above, combined with the adopted distance to the object. If available, we use redshift-independent distances (Cepheid, Tip of the Red Giant Branch, Tully-Fisher, etc) as tabulated in NED³, adopting the median value as a robust estimate that minimizes the impact of completely unphysical values, compared to the distribution, occasionally found in lists curated by NED. For those without redshift-independent distances, we instead compute the redshift luminosity distance in the CMB frame after correcting for LG motion. In the case of physical diameters and beam sizes, we instead use the angular diameter distance. For luminosities, we compute two different kinds: spectral νL_{ν} , and in-band L_{λ} , the former is used for star formation rates and the latter for stellar mass, as is the tradition. It should be emphasized that these two luminosities are distinctly different, the spectral luminosity is monochromatic and normalized by the bolometric luminosity of the Sun, while the in-band is normalized by the integrated Solar spectrum convolved with the *WISE* W1 band (as computed in Jarrett et al. 2013). Key derived parameters are listed in Table 3.

5.1. Physical Size Distribution

We compute the diameters using the W1 ($3.4 \mu\text{m}$) $1-\sigma_{\text{sky}}$ isophotal radii and the redshift-independent distance or the angular diameter distance (as discussed

above). The distribution of the 100 largest (angular) galaxies is presented in Fig. 14, ranging from a few kpc to the well over 100 kpc. Here we have once again divided the sample by the color classification (Fig. 10) to discern any trends with the morphology proxy.

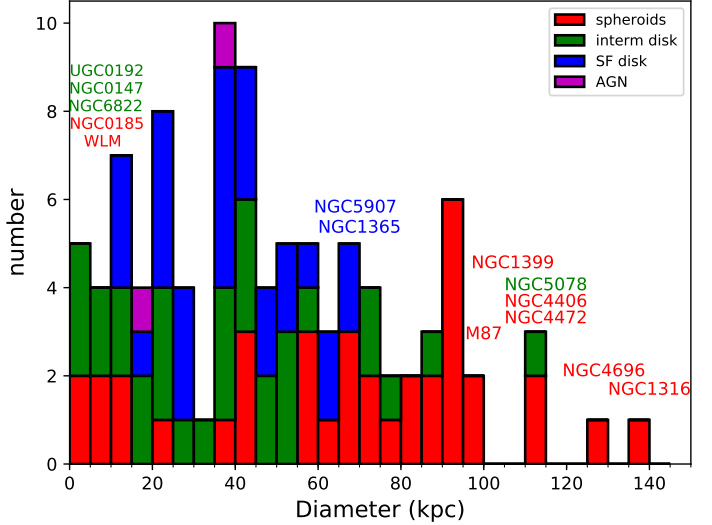


Figure 14. Physical size (kpc) distribution for the 100 largest (angular) galaxies, based on the infrared W1 ($3.4 \mu\text{m}$) size. The galaxies are group-delineated by their *WISE* colors (see Fig. 10), with notable galaxies labeled.

To begin with, there is a stark separation between the two flavours of early-type systems (bulge-dominated spheroids): giant cluster (brightest or BCG) galaxies and the dwarf spheroidals. Fornax A has the largest diameter, nearly 140 kpc in size, closely followed by the largest Virgo Cluster galaxies, which are all double or triple the size of large disk galaxies (e.g., Milky Way is ~ 50 kpc in extent), and some local BCG galaxies (e.g., NGC 4696 and NGC 5078). Intermediate disk galaxies (e.g., NGC 5078) have the second largest distribution. At the other end of the scale, the diminutive satellite dwarf spheroidals (e.g., NGC 0147) are the representative population, followed by dwarf intermediate-type galaxies (e.g., NGC 6822). Occupying the center stage, late-type disks uniformly range from small ~ 10 kpc to the broad 60 kpc diameters. Setting aside the extreme size (~ 100 kpc) of radio galaxy M 87 (Virgo A), the two outstanding AGNs in the sample, NGC 1068 (M 77) and Circinus, have host galaxy sizes that are not particularly large, < 25 kpc, indicating relatively modest or compact bulges and SF regions. We will investigate this trend with the larger WXSC sample to see if Seyferts and AGN in general are more compact relative to SF disk galaxies.

³ <http://ned.ipac.caltech.edu/Library/Distances/>

5.2. Spatial Resolution

WISE does not have outstanding angular resolution, roughly $6''$ in the shortest bands. Nevertheless, the largest galaxies in the sky are also (typically) the nearest galaxies, and hence the physical spatial resolution is well-suited for the study of the internal components of galaxies. Examining Column 4 in Table 3, the physical beam size (at $3.4\ \mu\text{m}$) ranges from 1 to 2 parsecs in the Magellanic Clouds, to <300 pc for Local Volume galaxies (e.g., M51), and 500 pc for Virgo and Fornax Cluster galaxies, and up to 1 kpc for the most distant galaxies in the 100 largest sample. The four independent bands of *WISE* at this physical resolution makes it a superlative imaging set to combine with complementary data sets (e.g., GALEX-UV; Herschel-PACS; radio continuum; neutral hydrogen) in order to study the internal star formation processes in GMCs and the general ISM; see for example the detailed study of M31 (Tomicic et al. 2019), M33 (Kam et al. 2017; Elson et al. 2019), NGC 253 (Lucero et al. 2015), and M83 (Jarrett et al. 2013; Heald et al. 2016). Both the standard and mask/cleaned *WISE* mosaics (see Appendices C and D) of the largest galaxies will be publicly available to the astronomical community through NED and other astronomical archives.

5.3. Global Stellar Mass

As one of the most important physical parameters toward decoding the star formation history of a galaxy, estimating the aggregate stellar mass is one of the key priorities for near- and mid-infrared imaging extragalactic surveys because of their sensitivity to the evolved population R-J stellar bump between 1 and 4 microns; see (Jarrett et al. 2013) for discussion of the *Spitzer*-IRAC and *WISE* bands used to trace the stellar mass. Accordingly, the galaxy host stellar mass is estimated using the W1 integrated (isophotal) flux density converted to in-band luminosity, L_{W1} , and the M/L ratio based on the W1–W2 color relation (Cluver et al. 2014). Here we assume the W1 ($3.4\ \mu\text{m}$) light arises from the evolved population, and that the short-lifetime dusty-phase populations (post-AGBs) are not significantly skewing the near-infrared brightness compared to the calibrated relation⁴

We adopt the ‘nearby galaxy’ M/L prescription from Cluver et al. (2014), where the *WISE* W1 in-band luminosity was calibrated against GAMA stellar masses

⁴ The $3\text{--}5\ \mu\text{m}$ bands appear to remarkably trace the stellar mass compared to other independent metrics (Cluver et al. 2014; Ponomereva et al. 2017; Kettlety et al. 2018), but see also Querejeta et al. (2015) and Meidt et al. (2012) for altering views.

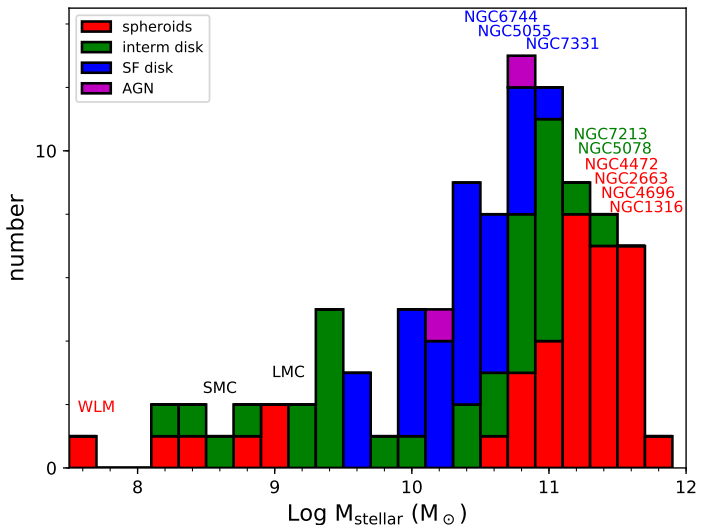


Figure 15. Stellar mass distribution for the 100 largest galaxies. The galaxies are group-delineated by their *WISE* colors (see Fig. 10), with a few of the exceptional labeled.

derived using stellar population synthesis models (Taylor et al. 2011). The relation is reproduced here:

$$\log_{10} M_{\star}/L_{W1} = -2.54(W1 - W2) - 0.17, \quad (2)$$

where $L_{W1} (L_{\odot, W1}) = 10^{-0.4(M - M_{\odot, W1})}$, M is the absolute magnitude of the source in W1, and $M_{\odot, W1} = 3.24$ mag is the W1 in-band solar value; see Jarrett et al. (2013). We place floor/ceiling limits on the W1–W2 color: -0.05 to 0.2 mag – corresponding M/L ranging from 0.21 to 0.91 – to minimize the contaminating effects of AGN light, as well as unphysical blue colors due to low S/N in the W2 band (relative to the more sensitive W1 band). For those dwarf galaxies with only W1 detections or colors with $S/N \leq 3$, we adopt a M/L value of 0.6 (Kettlety et al. 2018). In general, adopting a single M/L between 0.5 (for disk galaxies, see Ponomereva et al. 2017) and 0.7 (bulge-dominated types; see Cluver et al. 2014) is a good strategy for estimating the stellar mass using *WISE* W1 ($3.4\ \mu\text{m}$) light.

The distribution of stellar mass is presented in Figure 15, with the sample delineated by color as before. Unsurprisingly, the largest-diameter galaxies are also the most massive. These bulge-dominated early-type systems typically have values $>10^{11} M_{\odot}$. In terms of the stellar mass, the most massive galaxy is NGC 1316 (Fornax A) weighing in at $5.2 \times 10^{11} M_{\odot}$, which is nearly an order of magnitude larger than the Milky Way at $6 \times 10^{10} M_{\odot}$ (Licquia & Newman 2015). At the other extreme, the dwarf spheroids have $\text{Log } M_{\star}$ values that range between 7.5 and 8.5. The least massive galaxies, 6 to 7, are the very low SB dwarfs (e.g., ESO 245-007),

which are only visible to *WISE* in the Local Volume, $d < 10$ kpc. The Magellanic Clouds are in the upper dwarf range (8.5 - 9.0). Intermediate disks, such as M81 ($\text{Log } M_* = 10.85$) and M31 (10.96), are the second most massive population (but also have a ‘dwarf’ population near 9.4), followed by the late-type SF disks, which tend to have $\text{Log } M_* < 10.5$, and are clearly still building their disks (see SFR and specific-SFR below and in Table 2). The Milky Way falls within the intermediate range, with an estimated $\text{Log } M_* = 10.78$ (Licquia & Newman 2015), somewhat smaller than its sister galaxy, M31.

5.4. Star Formation Activity

The ISM-sensitive bands of *WISE*, W3 ($12 \mu\text{m}$) and W4 ($23 \mu\text{m}$) are effective tracers of the dust-obscured SF activity (Jarrett et al. 2013; Cluver et al. 2014, 2017). It turns out that W3 is particularly effective because, not only is it far more sensitive than the $23 \mu\text{m}$ band, but it better traces the total infrared luminosity, and appears to be robust to metallicity variation. This is largely attributable to the breadth of the W3 band, resulting in it being dominated by the dust continuum and less susceptible to emission-line and PAH variations (Cluver et al. 2017), compared to, for example, the *Spitzer*-IRAC $8 \mu\text{m}$ band. We should stress that galaxies with little to no dust emission, or alternatively very low metallicities, will have correspondingly low SFRs based on the infrared emission. It is more appropriate to use $\text{H}\alpha$ and UV tracers of SF for such galaxies, which may be particularly important for dwarf galaxies.

In the low- z universe, the W3 $12 \mu\text{m}$ band includes contributions from the warm $T \sim 150$ K dust continuum, the 7.7, 8.5, and $11.3 \mu\text{m}$ PAHs, and the $12.8 \mu\text{m}$ [Ne II] and $15.7 \mu\text{m}$ [Ne III] emission features. It is thus sensitive to SF activity (but also metallicity), as well as a small fraction of stellar light (R-J tail). Although our sample does not contain any extreme IR-bright galaxies, the closest being NGC 1068, we should note that the band also contains a $10 \mu\text{m}$ silicate absorption, which is clearly present in the spectra of heavily dust-obscured galaxies, such as Arp 220. Cluver et al. (2017) does observe that LIRGS and ULIRGS have a slightly different SFR relation compared to normal galaxies, likely indicative of the extreme dust and ice(s) absorption. For these extreme infrared-bright galaxies, we recommend using the $23 \mu\text{m}$ W4 band.

Relative to the near-IR bands of *WISE*, W1 and W2, the mid-IR W3 and W4 bands are not nearly as sensitive; this particularly affects stellar-continuum (bulge) dominated systems with predominately R-J emission at these wavelengths. Hence, SF activity can only be measured for (1) relatively nearby galaxies, or (2) relatively dusty galaxies. Luminous infrared galaxies can be de-

tected to high redshift (e.g., the Hyper-LIRGs discovered by *WISE*; see Tsai et al. (2015)). There are cases where the W3 flux is easily detected, but after subtraction of the stellar continuum (estimated from the W1 flux), there is nothing left representing the ISM emission (e.g., NGC 2768). Nevertheless, for most of the largest galaxies in the sky, and for most WXSC galaxies within $z < 0.1$, SF activity can be estimated using *WISE*.

We employ the latest SFR calibration based on the total infrared luminosity – and adopting a Kroupa (2002) initial mass function (IMF) – of a varied sample of nearby systems from the SINGS (Kennicutt et al. 2003) and KINGFISH (Kennicutt et al. 2011) surveys, correlated to the corresponding mid-infrared luminosities (Cluver et al. 2017). The general prescription is that the 12 and $23 \mu\text{m}$ SFRs are derived from the spectral luminosities: νL_ν , where ν is the bandpass central frequency and is normalized by the bolometric luminosity of the Sun.⁵

The total infrared SFR scaling relations of Cluver et al. (2017) are given by:

$$\text{Log}_{10} \text{SFR}_{\text{TIR}}(M_\odot/\text{yr}) = 0.873(\pm 0.021) \times \text{Log}_{10} \nu L_{12 \mu\text{m}}(L_\odot) - 7.62(\pm 0.18) \quad (3)$$

$$\text{Log}_{10} \text{SFR}_{\text{TIR}}(M_\odot/\text{yr}) = 0.900(\pm 0.027) \times \text{Log}_{10} \nu L_{22 \mu\text{m}}(L_\odot) - 7.87(\pm 0.24) \quad (4)$$

where $\nu L_{12 \mu\text{m}}$ and $\nu L_{22 \mu\text{m}}$ are the spectral luminosities, normalized by the solar luminosity (L_\odot), and the stellar continuum removed using the W1 luminosity as a proxy for the stellar continuum, as follows: 15.8% in the W3 band, and 5.9% in the W4 band (see Cluver et al. (2017) for details). Note that the relation uncertainties, in particular the offsets, render SFR accuracy of at minimum 20 to 25%, but can be several percent higher when propagating the formal photometric errors. Moreover and as noted earlier, the mid-IR SFRs are based on the warmed ISM that arises from dust-obscured star formation, which does not account for unobscured UV emission from young stars that manages to escape the host galaxy.

The SFRs and stellar masses for each galaxy are presented in Table 3, which includes the redshift-independent or luminosity distance (column 3), the physical resolution (4), the colors (5, 6), the spectral luminosities, continuum-subtracted (7, 8), the W1 in-band luminosity (9), the estimated stellar mass (10),

⁵ We note that the spectral luminosity is different from the in-band luminosity due to the bolometric versus W1 in-band normalization. See Jarrett et al. (2013).

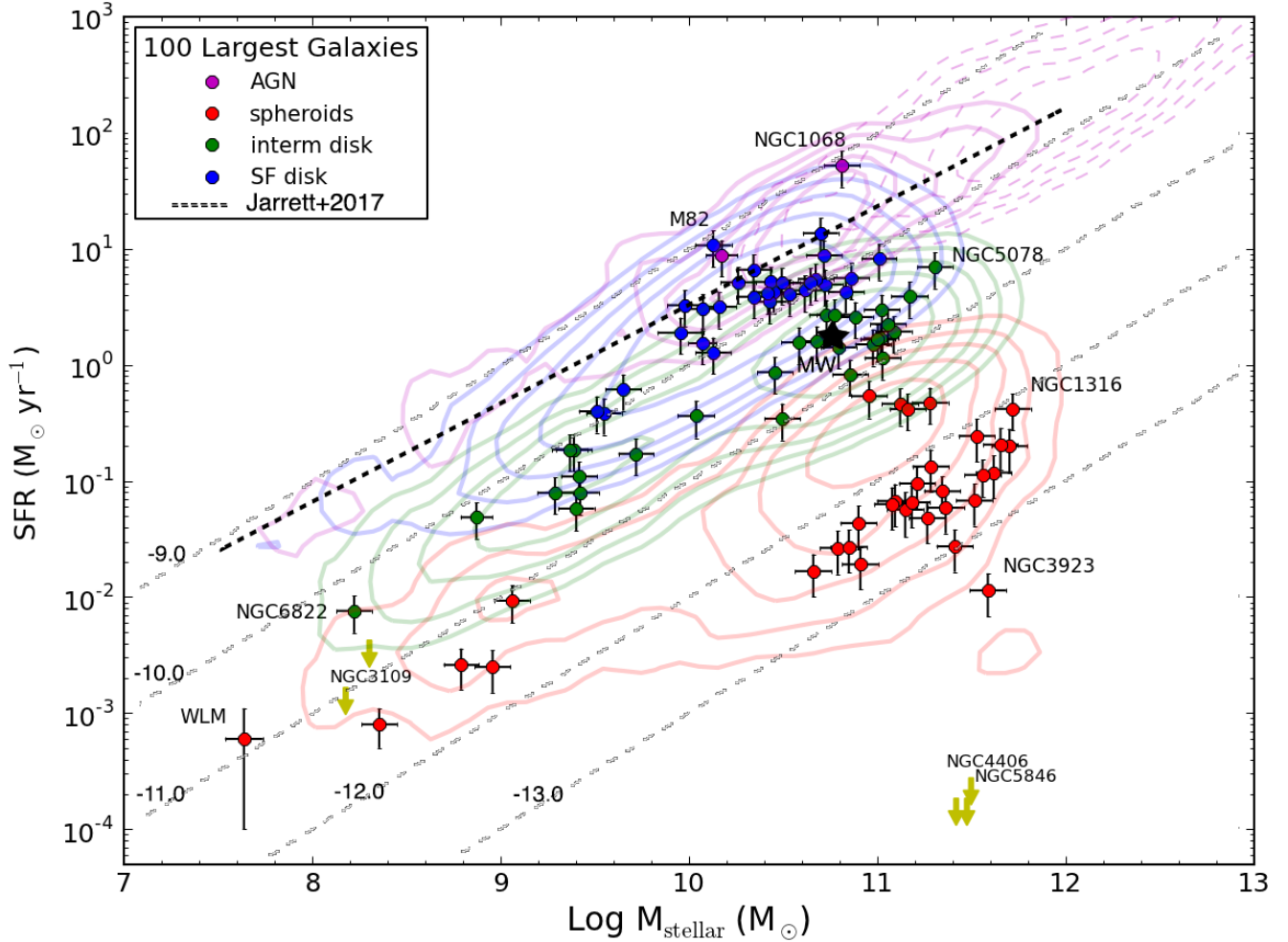


Figure 16. Galaxy Main Sequence (GMS): star-formation rate (based on W3, Eq. 3) versus stellar mass sequence for the 100 largest galaxies (points and error bars) and the bright galaxy sample from the WXSC (contours, where the higher redshifts are magenta dashed contours, tracking the AGN). The data are delineated by their *WISE* colors (Fig. 10), and generally fall below the sequence derived from a more distant (and luminous) sample as defined by the GAMA-G12 region Jarrett et al. (2017), dashed line. The Milky Way (MW, black star symbol) is located in the central spread of the “intermediate” disk galaxies (green points and contours). The faint dashed lines represent lines of constant $\text{Log sSFR} = -13, -12, -11, -10$ and -9.0 yr^{-1} .

and the TIR SFRs from the W3 and W4 (11,12) spectral luminosities. Here the spectral luminosities, with the stellar subtraction, represent the $12 \mu\text{m}$ aggregate and $23 \mu\text{m}$ dust emission after stellar continuum subtraction. Finally, the specific star formation rate (sSFR, column 13) is the SFR normalized by the stellar mass.

To graphically show the SFR results, we relate the SFRs (based on the W3 relation) with the corresponding host stellar masses, creating the so-called galaxy star formation “main sequence” (hereafter referred to as the GMS), Fig. 16. This GMS sequence gives a crude representation of the past-to-present star formation history in which ever larger SFRs track with ever larger stellar masses, which appears to hold even at higher redshifts (see for example Elbaz et al. 2007; Noeske et al. 2007;

Bouché et al. 2010). The slope of the sequence therefore represents a secular evolution path, with deviations due to events from interactions, bar formation, AGN and superwind feedback, starburst and quenching events. For reference, we show lines of constant specific star formation ratio ($\text{sSFR} = \text{SFR}/\text{mass}$, column 13 of Table 3), ranging from 10^{-13} to 10^{-9} yr^{-1} , covering the range that is seen for nearby galaxies, from active building (10^{-9} to 10^{-10}), to semi-quiescent (10^{-10} to 10^{-11}) and quenched or depleted ($< 10^{-11}$).

To put the largest 100 galaxies into context, we show the results for the larger WXSC sample, some 5000 galaxies, contours coded by color classification as before, and the overall trend in the GMS derived from a

higher redshift (z complete up to 0.3) sample from the GAMA G12 region (Jarrett et al. 2017).

A number of interesting features are seen in Figure 16. The dusty galaxies with their strong W3 emission (blue points in the plot) are generally massive in stars, $\text{Log } M_{\star} > 10$ and relatively high (>2) SFRs, defining the upper end of the sequence. A maximum SFR is reached where the disk galaxies appear to turn over at stellar mass of $\text{Log } M_{\star}$ between 10.4 to 10.7, perhaps signifying a gas-depletion phase. Sitting well above the sequence is the starburst galaxy M 82, clearly demonstrating how young (Myr) starburst events move galaxies upward, outpacing the stellar mass Gyr build-up time scale. A cautionary note: the highest SFR galaxy is NGC 1068 (see also the Circinus Galaxy), which represents an upper limit since the AGN accretion emission from hot dust is heavily boosting the *WISE* fluxes – while even more luminous galaxies with AGN (e.g., Mrk 231, see Cluver et al. 2017) move long this upper AGN-sequence as represented by the dashed magenta contours, and should be viewed with discretion: neither the SFR nor the stellar mass of mid-infrared AGN is properly measured or modeled with simple *WISE* fluxes and colors.

As galaxies build their mass and consume their gas, they move to the right and down from the SF sequence, as demonstrated by the intermediate disk galaxies (green points and contours). Andromeda (M 31), M 81 and the Milky Way, values from Licquia & Newman (2015), are example galaxies that have built the bulk of their stellar backbone, while continuing to form stars at a relatively semi-quiescent rate, ~ 1 to $2 M_{\odot} \text{ yr}^{-1}$. The final evolutionary sequence is dominated by the spheroidals (red points), with examples of dwarf ($< 10^9 M_{\odot}$) and massive ($> 10^{11} M_{\odot}$) varieties in the 100 largest galaxies, whose SF rates are several orders of magnitude smaller than those of disk galaxies, and correspondingly low sSFRs ($< 10^{-12} \text{ yr}^{-1}$). Presumably the gas has been depleted – or accretion shutdown, so-called strangulation (Peng et al. 2015) – halting the SF and creating a downward descent from the GMS, reaching a peak in stellar mass around $\text{Log } M_{\star}(M_{\odot}) \sim 11.5$. The SF activity is so low for many of these early types that no *WISE* W3 emission is detected, and hence only upper limits are indicated in the GMS plot, for example the Heart of Virgo, NGC 4406 (M 86). As previously noted, galaxies with low dust content may poorly trace the ongoing SF that is better detected and traced using UV *GALEX* imaging or $\text{H}\alpha$ spectro-imaging.

In Figure 16, we can also compare the GMS of the bright and nearby galaxy with that of a deep and complete redshift survey (dashed line), GAMA-G12 $z < 0.3$ (Jarrett et al. 2017). Dwarf spheroidals, such as NGC 0185, have the lowest SFRs, 1 or 2 orders lower than the low-mass dwarfs in G12. It should be noted that G12 is optically selected (r-band) and preferentially finds redshifts of emission line systems at ever larger distances (hence relatively-unobscured SF disk galaxies, which would have higher SFRs than dwarf spheroidals). The corresponding specific-SFRs of the dwarf spheroidals is quite long, $> 10^{-11} \text{ yr}^{-1}$, confirming their quiescent state. The late-type SF galaxies, such as M 83, have unsurprisingly, the highest SFR rates and lie within the G12 sequence (i.e., consistent with the GAMA selection), with $> 10^{-9} \text{ yr}^{-1}$ rapid-building rates. In the 100-largest sample, the most rapidly-building galaxy is M 82, its current starburst phase is perhaps just one of many that will occur in its lifetime. Meanwhile, the massive, high-surface bright spheroidals, such as NGC 4696, have rapidly declining specific-SFRs, 10^{-12} yr^{-1} , indicating they are ‘dead’, having consumed their gas and fallen off the sequence long ago.

Table 3. Derived Global Stellar Mass and SFRs

iS	Galaxy	d	beam	1–2	2–3	Log L_{W1}	Log M_*	Log νL_3	Log νL_4	SFR $_{W3}$	SFR $_{W4}$	Log sSFR
(1)	(2)	Mpc	pc	mag	mag	$L_{\odot, W1}$	M_{\odot}	L_{\odot}	L_{\odot}	$M_{\odot} \text{ yr}^{-1}$	$M_{\odot} \text{ yr}^{-1}$	yr^{-1}
		(3)	(4)	(5)	(6)	(7)	(8)	(9)	(10)	(11)	(12)	(13)
1	LMC	0.05	1	0.06	2.79	9.47 0.01	9.15 0.11	7.62 0.01	7.76 0.01	0.12 0.03	0.03 0.14	-10.07
2	SMC	0.06	2	-0.05	1.55	8.63 0.01	8.59 0.09	6.06 0.01	6.43 0.01	0.01 0.01	0.01 0.01	-10.59
3	MESSIER31	0.77	22	-0.03	2.09	11.04 0.02	10.95 0.14	8.82 0.02	8.48 0.03	1.20 0.11	0.58 0.07	-10.88
4	MESSIER33	0.86	25	0.07	3.18	9.97 0.02	9.61 0.14	8.33 0.02	8.22 0.03	0.45 0.04	0.33 0.04	-9.96
5	NGC0253	3.01	88	0.19	3.83	10.88 0.01	10.24 0.09	9.54 0.01	9.64 0.01	5.36 1.86	6.52 2.56	-9.51
6	NGC5128	3.65	106	0.01	2.55	11.23 0.01	11.02 0.09	9.25 0.02	9.12 0.01	2.98 1.03	2.16 0.85	-10.55
7	NGC0055	2.10	61	0.09	2.66	9.77 0.01	9.39 0.09	7.88 0.02	8.06 0.01	0.19 0.06	0.23 0.09	-10.11
8	MESSIER81	3.65	106	-0.01	1.81	10.99 0.01	10.85 0.09	8.62 0.04	8.44 0.02	0.82 0.29	0.52 0.20	-10.94
9	MESSIER101	7.22	210	0.12	3.54	10.91 0.01	10.45 0.10	9.43 0.01	9.36 0.01	4.22 1.46	3.61 1.42	-9.82
10	NGC4945	3.22	94	0.18	3.57	10.71 0.01	10.07 0.09	9.26 0.01	9.15 0.01	3.03 1.05	2.31 0.91	-9.59
11	IC0342	3.14	91	0.05	3.80	10.74 0.01	10.43 0.09	9.33 0.02	9.23 0.01	3.49 1.21	2.75 1.08	-9.88
12	NGC1316	18.92	550	-0.03	0.74	11.82 0.01	11.72 0.10	8.28 0.61	8.60 0.06	0.42 0.14	0.73 0.29	-12.09
13	MESSIER49	15.28	444	-0.09	0.47	11.66 0.01	11.62 0.10	<4.28	7.73 0.28	<0.01	0.12 0.05	<-12.17
14	MESSIER86	16.32	475	-0.05	-0.18	11.53 0.01	11.48 0.10	<4.33	<4.04	<0.01	<0.01	<-10.84
15	MAFFE11	3.39	99	-0.04	-0.03	10.85 0.01	10.79 0.10	<2.97	7.02 0.23	<0.01	0.03 0.01	<-11.43
16	MESSIER110	0.82	24	-0.05	0.89	9.00 0.01	8.96 0.09	5.75 0.31	5.85 0.06	0.01 0.00	0.00 0.00	-10.96
17	MESSIER104	9.38	273	-0.03	1.01	11.38 0.01	11.28 0.09	8.34 0.19	8.30 0.04	0.47 0.16	0.39 0.15	-11.61
18	NGC2403	3.18	93	0.09	3.38	10.04 0.01	9.65 0.09	8.47 0.01	8.43 0.01	0.61 0.21	0.51 0.20	-9.86
19	NGC0247	3.44	100	-0.04	2.67	9.79 0.01	9.72 0.09	7.84 0.03	7.73 0.04	0.17 0.06	0.12 0.05	-10.49
20	MESSIER106	7.31	213	0.03	2.51	10.93 0.01	10.68 0.09	8.94 0.02	8.80 0.02	1.60 0.55	1.12 0.44	-10.47
21	MESSIER87	15.80	460	-0.07	0.42	11.57 0.01	11.53 0.10	<4.30	8.08 0.11	<0.01	0.24 0.10	<-12.49
22	NGC3628	10.45	304	0.12	3.24	11.02 0.01	10.53 0.09	9.40 0.01	9.33 0.01	4.05 1.40	3.40 1.33	-9.93
23	NGC0300	1.93	56	-0.00	2.59	9.58 0.01	9.41 0.10	7.62 0.02	7.55 0.01	0.11 0.04	0.08 0.03	-10.37
24	NGC4736	5.20	151	0.02	2.75	10.81 0.01	10.58 0.10	8.93 0.02	8.80 0.01	1.56 0.54	1.11 0.44	-10.39
25	NGC6822	0.47	14	-0.02	2.45	8.34 0.01	8.22 0.09	6.30 0.04	6.39 0.05	0.01 0.00	0.01 0.00	-10.22
26	NGC1532	14.25	415	0.05	2.86	11.02 0.01	10.73 0.09	9.20 0.02	9.02 0.02	2.69 0.93	1.76 0.69	-10.30
27	NGC5236	4.51	131	0.12	3.82	10.90 0.01	10.43 0.10	9.53 0.01	9.56 0.01	5.17 1.79	5.42 2.12	-9.72
28	NGC0147	0.73	21	-0.02	1.85	8.41 0.01	8.30 0.09	6.06 0.04	<1.34	<0.01	<0.01	<-9.69
29	NGC6744	9.51	277	0.01	3.35	11.04 0.01	10.83 0.09	9.43 0.02	9.20 0.01	4.24 1.47	2.57 1.01	-10.20
30	MESSIER63	9.81	285	0.05	3.35	11.16 0.01	10.86 0.09	9.56 0.01	9.38 0.01	5.60 1.94	3.75 1.47	-10.11
31	NGC1553	17.18	500	-0.06	0.69	11.39 0.01	11.34 0.10	7.47 1.42	8.04 0.08	0.08 0.03	0.22 0.09	-12.44
32	NGC1399	19.61	570	-0.08	0.39	11.56 0.01	11.51 0.10	<4.49	7.47 0.41	<0.01	0.07 0.03	<-11.90
33	NGC4236	4.47	130	-0.09	2.32	9.44 0.01	9.40 0.10	7.31 0.04	7.56 0.02	0.06 0.02	0.08 0.03	-10.62
34	NGC4565	12.05	351	0.04	2.56	11.14 0.01	10.88 0.09	9.18 0.02	8.99 0.01	2.58 0.89	1.67 0.66	-10.47
35	Maffe12	2.79	81	0.07	3.57	10.42 0.01	10.07 0.08	8.93 0.01	8.82 0.01	1.53 0.53	1.17 0.46	-9.89
36	NGC4631	7.35	214	0.19	3.84	10.63 0.01	9.98 0.09	9.30 0.01	9.27 0.01	3.26 1.13	2.95 1.16	-9.46
37	MESSIER60	17.36	505	-0.05	0.68	11.60 0.01	11.56 0.10	7.64 1.61	8.14 0.11	0.11 0.04	0.27 0.11	-12.52
38	NGC4636	14.85	432	-0.07	0.33	11.19 0.01	11.15 0.10	<4.25	7.38 0.22	<0.01	0.06 0.02	<-11.80
39	NGC2768	20.60	599	-0.03	0.34	11.20 0.01	11.09 0.10	<4.54	7.46 0.18	<0.01	0.07 0.03	<-11.83
40	NGC3585	18.14	528	-0.07	0.25	11.31 0.01	11.26 0.10	<4.43	7.30 0.34	<0.01	0.05 0.02	<-11.74
41	ESO270-G017	15.37	447	0.01	2.43	10.24 0.01	10.04 0.10	8.21 0.04	8.31 0.03	0.36 0.13	0.40 0.16	-10.48
42	MESSIER51a	9.12	265	0.11	3.81	11.16 0.01	10.71 0.09	9.79 0.01	9.66 0.01	8.77 3.04	6.77 2.65	-9.77
43	NGC3115	9.64	280	-0.02	0.33	11.03 0.01	10.91 0.10	<3.88	6.87 0.48	<0.01	0.02 0.01	<-11.22
44	NGC3923	20.08	584	-0.10	0.15	11.52 0.01	11.47 0.10	<4.51	<4.22	<0.01	<0.01	<-10.82
45	NGC4365	21.68	631	-0.11	-0.37	11.46 0.01	11.42 0.10	<4.58	<4.28	<0.01	<0.01	<-10.76
46	NGC1313	4.12	120	0.05	3.30	9.86 0.01	9.55 0.09	8.24 0.02	8.37 0.02	0.38 0.13	0.45 0.18	-9.97
47	MESSIER84	17.70	515	-0.03	0.12	11.50 0.01	11.41 0.10	<4.40	7.04 0.97	<0.01	0.03 0.01	<-11.42
48	NGC0185	0.64	19	-0.04	0.89	8.43 0.01	8.35 0.09	5.22 0.29	5.13 0.07	<0.01	<0.01	<-9.48
49	NGC6946	5.89	171	0.16	3.91	10.84 0.01	10.26 0.09	9.52 0.01	9.46 0.01	5.14 1.78	4.43 1.74	-9.55
50	NGC1395	22.03	641	-0.07	0.28	11.40 0.01	11.36 0.10	<4.59	7.40 0.34	<0.01	0.06 0.02	<-11.83

NOTE—columns: (1) order of W1 ($3.4 \mu\text{m}$) angular size; (2) Galaxy name; (3) distance; (4) physical resolution, based on $6''$ beam; (5) W1–W2 color; (6) W2–W3 color; (7) W1 in-band luminosity; (8) stellar mass derived from Log L_{W1} and the color-dependent mass-to-light; (9, 10) W3 and W4 spectral luminosities, Log νL_{ν} , after subtraction of the stellar continuum; (11, 12) TIR star formation rates based on W3 and W4.

Table 3. ... continued: Derived Global Stellar Mass and SFRs

iS	Galaxy	d	beam	1–2	2–3	Log L_{W1}	Log M_*	Log νL_3	Log νL_4	SFR $_{W3}$	SFR $_{W4}$	Log sSFR
(1)	(2)	Mpc	pc	mag	mag	$L_{\odot, W1}$	M_{\odot}	L_{\odot}	L_{\odot}	$M_{\odot} \text{ yr}^{-1}$	$M_{\odot} \text{ yr}^{-1}$	yr^{-1}
		(3)	(4)	(5)	(6)	(7)	(8)	(9)	(10)	(11)	(12)	(13)
51	IC0010	0.77	22	0.03	2.73	9.10 0.01	8.87 0.08	7.22 0.02	7.42 0.01	0.05 0.02	0.06 0.02	-10.17
52	NGC4517	10.63	309	0.08	3.15	10.51 0.01	10.13 0.09	8.83 0.01	8.72 0.01	1.27 0.44	0.94 0.37	-10.02
53	NGC1291	10.54	307	-0.05	1.20	11.18 0.01	11.12 0.10	8.33 0.12	8.19 0.05	0.46 0.16	0.31 0.12	-11.46
54	NGC2683	8.47	246	0.03	2.37	10.70 0.01	10.45 0.09	8.64 0.02	8.29 0.02	0.87 0.30	0.38 0.15	-10.51
55	NGC4697	10.50	305	-0.05	0.22	10.94 0.01	10.90 0.10	<3.95	7.26 0.17	<0.01	0.04 0.02	<-11.67
56	NGC3521	8.60	250	0.09	3.40	11.00 0.01	10.61 0.09	9.44 0.01	9.26 0.01	4.37 1.51	2.92 1.14	-9.97
57	NGC3109	1.25	36	-0.02	1.35	8.30 0.01	8.18 0.10	5.60 0.09	<1.80	<0.01	<0.00	<-9.23
58	NGC0891	7.09	206	0.19	3.37	10.81 0.01	10.16 0.09	9.28 0.01	9.13 0.01	3.16 1.09	2.20 0.86	-9.66
59	MESSIER85	14.38	418	-0.04	0.38	11.27 0.01	11.21 0.10	<4.22	7.63 0.15	<0.01	0.10 0.04	<-12.03
60	NGC4244	4.21	122	0.04	2.29	9.55 0.01	9.29 0.09	7.46 0.03	7.49 0.03	0.08 0.03	0.07 0.03	-10.38
61	NGC4762	13.86	403	-0.05	0.42	10.71 0.01	10.66 0.10	<4.19	6.80 0.27	<0.01	0.02 0.01	<-11.22
62	NGC5084	17.88	520	-0.03	1.41	11.06 0.01	10.95 0.09	8.41 0.09	8.27 0.04	0.54 0.19	0.36 0.14	-11.22
63	NGC5907	17.06	496	0.11	3.15	11.16 0.01	10.72 0.09	9.50 0.01	9.33 0.01	4.92 1.70	3.39 1.33	-10.03
64	NGC4395	4.51	131	-0.04	2.47	9.50 0.01	9.42 0.10	7.46 0.04	7.62 0.04	0.08 0.03	0.09 0.04	-10.52
65	NGC1407	25.41	739	-0.09	0.34	11.63 0.01	11.59 0.10	<4.72	6.62 3.39	<0.01	<0.01	<-11.06
66	NGC3627	10.02	291	0.10	3.45	11.09 0.01	10.67 0.09	9.56 0.01	9.51 0.01	5.49 1.90	4.97 1.95	-9.93
67	NGC4438	11.32	329	0.01	1.57	10.69 0.01	10.49 0.09	8.19 0.06	8.06 0.03	0.34 0.12	0.23 0.09	-10.96
68	NGC1365	17.92	521	0.28	3.65	11.38 0.01	10.70 0.09	10.01 0.01	10.19 0.01	13.62 4.72	20.39 8.00	-9.56
69	NGC2903	9.98	290	0.08	3.55	11.02 0.01	10.64 0.09	9.52 0.01	9.46 0.01	5.07 1.76	4.42 1.74	-9.94
70	NGC5846	25.23	734	-0.06	0.10	11.54 0.01	11.50 0.10	<4.71	<4.42	<0.01	<0.00	<-10.82
71	NGC4725	12.74	371	-0.03	2.20	11.08 0.01	10.98 0.09	8.91 0.03	8.68 0.02	1.50 0.52	0.86 0.34	-10.80
72	NGC1549	17.66	514	-0.09	0.54	11.22 0.01	11.18 0.10	<4.40	7.45 0.20	<0.01	0.07 0.03	<-11.88
73	WLM	0.94	27	-0.08	0.64	7.68 0.01	7.64 0.10	<1.90	5.23 0.16	<0.01	0.00 0.00	<-8.44
74	NGC2841	14.08	410	-0.01	2.16	11.22 0.01	11.09 0.09	9.04 0.03	8.91 0.01	1.93 0.67	1.40 0.55	-10.80
75	Circinus	4.21	122	0.61	4.07	10.85 0.01	10.17 0.08	9.79 0.01	9.80 0.01	8.79 3.04	8.98 3.52	-9.23
76	NGC3621	7.01	204	0.13	3.66	10.46 0.01	9.95 0.12	9.03 0.01	8.87 0.01	1.89 0.65	1.29 0.51	-9.68
77	NGC5078	31.13	906	0.05	2.64	11.59 0.01	11.30 0.09	9.67 0.02	9.50 0.01	6.94 2.40	4.80 1.88	-10.46
78	NGC1023	10.41	303	-0.05	0.37	10.89 0.01	10.85 0.10	<3.94	7.03 0.24	<0.01	0.03 0.01	<-11.46
79	NGC7331	14.72	428	0.08	3.28	11.37 0.01	11.01 0.09	9.75 0.01	9.59 0.01	8.19 2.84	5.79 2.27	-10.09
80	MESSIER64	10.02	291	0.00	2.26	11.24 0.01	11.06 0.09	9.11 0.03	9.02 0.01	2.25 0.78	1.78 0.70	-10.70
81	MESSIER59	16.32	475	-0.08	0.61	11.12 0.01	11.08 0.10	<4.33	7.43 0.16	<0.01	0.06 0.03	<-11.86
82	NGC4696	36.83	1071	-0.06	0.36	11.74 0.01	11.70 0.09	<5.04	7.98 0.20	<0.01	0.20 0.08	<-12.40
83	MESSIER82	3.70	108	0.45	4.58	10.81 0.01	10.13 0.10	9.89 0.01	10.29 0.01	10.68 3.70	25.27 9.91	-9.10
84	ESO274-001	3.18	93	-0.03	1.28	9.15 0.01	9.06 0.09	6.40 0.11	7.31 0.01	<0.01	0.05 0.02	-11.06
85	MESSIER77	10.28	299	1.71	3.57	11.49 0.01	10.81 0.10	10.67 0.01	10.51 0.01	52.00 18.00	40.60 15.90	-9.09
86	NGC3077	3.82	111	0.08	2.71	9.75 0.01	9.37 0.09	7.88 0.02	8.03 0.01	0.19 0.06	0.22 0.09	-10.09
87	MESSIER65	12.65	368	-0.02	1.82	11.15 0.01	11.02 0.09	8.78 0.04	8.60 0.02	1.14 0.40	0.73 0.29	-10.97
88	NGC7213	26.66	776	0.08	2.14	11.53 0.01	11.17 0.10	9.38 0.03	9.37 0.03	3.87 1.34	3.64 1.44	-10.58
89	IC0356	11.75	342	-0.02	2.20	11.14 0.01	11.02 0.09	8.97 0.03	8.87 0.02	1.69 0.59	1.30 0.51	-10.79
90	NGC1560	3.01	88	-0.08	1.04	8.83 0.01	8.79 0.09	5.77 0.20	6.22 0.03	<0.01	<0.01	<-10.79
91	NGC2663	28.49	829	-0.09	0.03	11.69 0.01	11.65 0.09	<4.82	8.00 0.17	<0.01	0.21 0.08	<-12.43
92	NGC4216	15.50	451	-0.02	2.22	11.12 0.01	11.00 0.09	8.96 0.03	8.71 0.02	1.65 0.57	0.93 0.36	-10.78
93	NGC1055	14.16	412	0.12	3.60	10.88 0.01	10.42 0.09	9.42 0.01	9.27 0.01	4.18 1.45	3.01 1.18	-9.80
94	NGC5170	22.07	642	0.02	2.26	11.00 0.01	10.79 0.09	8.89 0.03	8.70 0.02	1.42 0.49	0.90 0.35	-10.64
95	MESSIER98	15.98	465	0.03	2.91	11.01 0.01	10.77 0.09	9.20 0.02	9.03 0.01	2.70 0.94	1.82 0.71	-10.34
96	NGC2997	11.32	329	0.11	3.73	10.93 0.01	10.49 0.09	9.52 0.01	9.40 0.01	5.08 1.76	3.88 1.52	-9.79
97	NGC4125	21.99	640	-0.04	0.44	11.35 0.01	11.28 0.10	<4.59	7.79 0.12	<0.01	0.13 0.05	<-12.18
98	NGC7793	3.95	115	0.08	3.27	9.88 0.01	9.51 0.09	8.26 0.01	8.09 0.01	0.40 0.14	0.25 0.10	-9.91
99	NGC5363	20.30	591	-0.02	1.02	11.29 0.01	11.16 0.10	8.28 0.18	8.29 0.04	0.42 0.14	0.38 0.15	-11.54
100	NGC4217	18.57	540	0.16	3.34	10.93 0.01	10.35 0.09	9.38 0.01	9.20 0.01	3.85 1.33	2.59 1.02	-9.76
-	IC1613	0.73	21	-0.19	<3.30	7.63 0.01	7.58 0.10	<1.63	<1.34	<0.01	<0.01	<-8.58
-	MESSIER32	0.82	24	-0.05	0.69	9.12 0.01	9.07 0.09	5.27 1.24	5.55 0.12	<0.01	<0.01	-11.07
-	UGC05373	1.42	41	0.11	<2.79	7.70 0.01	7.25 0.10	<2.21	5.07 0.14	<0.01	<0.01	<-6.91
-	ESO245-007	0.43	13	-0.22	<1.39	6.14 0.01	6.10 0.14	<1.17	<2.58	<0.01	<0.01	<-6.95

NOTE—columns: (1) order of angular size; (2) Galaxy name; (3) distance; (4) physical resolution, based on $6''$ beam; (5) W1-W2 color; (6) W2-W3 color; (7) W1 in-band luminosity; (8) stellar mass derived from Log L_{W1} and the W1-W2 color-dependent mass-to-light; (9, 10) W3 and W4 spectral luminosities, Log νL_{ν} , after subtraction of the stellar continuum; (11, 12) W3 and W4 star formation rates; (13) specific SFR(W3).

6. WISE EXTENDED SOURCE CATALOGUE

6.1. *The Largest Angular-size Galaxies*

We have presented the largest galaxies in the sky, based on the angular apparent size, as measured in the mid-infrared. Compared to large (> 5000) samples of bright nearby galaxies, the 100 largest have physical properties that are generally unremarkable. Nevertheless, because these galaxies are either LG members or tend to be very close to the Milky Way, < 50 Mpc, we have access to the lowest mass satellites and dwarf galaxies (e.g., NGC 6822, NGC 3109), while also graced by two galaxy clusters that have some singularly-large galaxies (e.g., Fornax A and Virgo A, and many other BCGs such as M 86).

We have shown that the apparent mid-IR colors have distinct trends that can be exploited to discern galaxies in different states of their star formation history, including semi-quiescent/passive types (intermediate or green-valley disks), actively building SF types (late-type disks), ‘dead’ and gas-poor types (spheroidals), and even incredibly slow yet building types (dwarf spheroidals). There are two stand-out galaxies with AGN: NGC 1068 and Circinus, both of which have extraordinarily high surface brightnesses, several magnitudes brighter than typical galaxies, indicative of their intense nuclear activity. In the following we discuss how the 100 largest and the greater WXSC can be used to further our understanding of galaxy evolution.

6.2. *Legacy of Large Galaxy Archives*

The 100 largest are interesting in the sense that they are nearby and may be studied in precise – resolution and multi-wavelength – detail; they can have very small physical sizes, or be giants that live within dense environments. This special sample is but a small set of a much larger one that is being constructed, the whole-sky WISE Extended Source Catalogue (WXSC), which will have tens of thousands of galaxies drawn from the local universe, many of which are legacy galaxies from early surveys such as the Messier and NGC (RC3) catalogs, but also fainter galaxies that enter the realm (targets) of large-area spectroscopic surveys such as SDSS-V (in the north; Kollmeier et al. 2017) and Taipan (in the south; da Cunha et al. 2016).

The legacy extragalactic data from the WXSC is timely particularly in the southern hemisphere, given the historic paucity of studies below the equator, and the rapid rise of large telescopes in the south. The Square Kilometre Array (SKA), for example, is driving radio surveys of the southern hemisphere first through the pathfinders (e.g., ASKAP, MeerKAT, both now underway) and later next decade, by the SKA itself. These

future surveys notably target the early universe, but will sweep across the sky and image the local universe with clarity (resolution), quality (S/N), and will range across the vast mass spectrum of galaxies that is so pivotal in connecting how baryons are cycled through the cosmic web, to halos and into galaxies.

The goal of the WXSC archive is to make available data products that are directly useful to these surveys, including source catalogs of global properties, large-area imaging showing the environments of galaxies, internal measurements (bulge-disk decompositions), and diagrams that summarize physical characteristics. Ultimately our aim is to measure all resolved galaxies as discerned in the W1 ($3.4\mu\text{m}$) band, estimated to be 1 to 2 million galaxies, which may be combined with the ALLWISE point source catalog (Cutri et al. 2012) and the deeper CATWISE catalog (Eisenhardt et al. 2019), to form a complete whole-sky census of galaxies down to 15 micro-Jy, and sensitive to early galaxy formation at redshifts beyond one.

The 100 Largest and WXSC are comprised of several data products – images, profiles, SEDs and tables – that fully characterize the measurements from WISE. As part of a value-add effort to compare and contrast across galaxy properties, we create graphic diagrams that depict the key global measurements and derived values – colors, surface brightness, size, star formation rate – with the goal to be able to categorize and discern groups of galaxies that have similar properties and SF histories. We refer to these as “pinwheel” diagrams, described below.

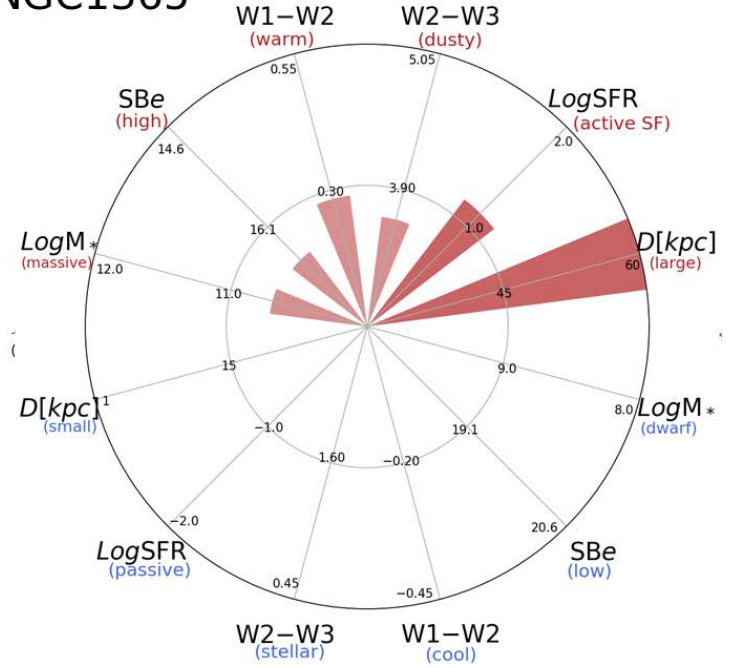
6.3. *Galaxy Physical Properties: the PINWHEEL DIAGRAM*

Inspired by the ‘starfish’ diagrams created for the SAMI survey of galaxies (see e.g., Konstantopoulos, 2014), we have constructed a polar-wedge schematic for each galaxy, which we will refer to as *pinwheel* diagrams. For a given attribute, e.g., SFR, the goal is to convey the value relative to some average or typical value observed for a large sample. In this way, the circular pinwheel can graphically show many attributes at once, conveying a signature pattern for that galaxy. We can then use that pattern, for example, to match against other galaxies in order to associate similar kinds of galaxies or those in comparable phases of their stellar-population evolution.

An example of the pinwheel diagram, for the barred Fornax spiral galaxy, NGC 1365, is shown in Fig. 17a. The six attributes that make the pinwheel are the following: mid-IR colors [W1-W2], [W2-W3], effective surface brightness (SBe), stellar mass ($\text{Log } M_{\star}$), diameter ($D[\text{kpc}]$), and star formation rate (Log SFR). Starting from the center, 0% departure from average, circular



NGC1365



NGC423

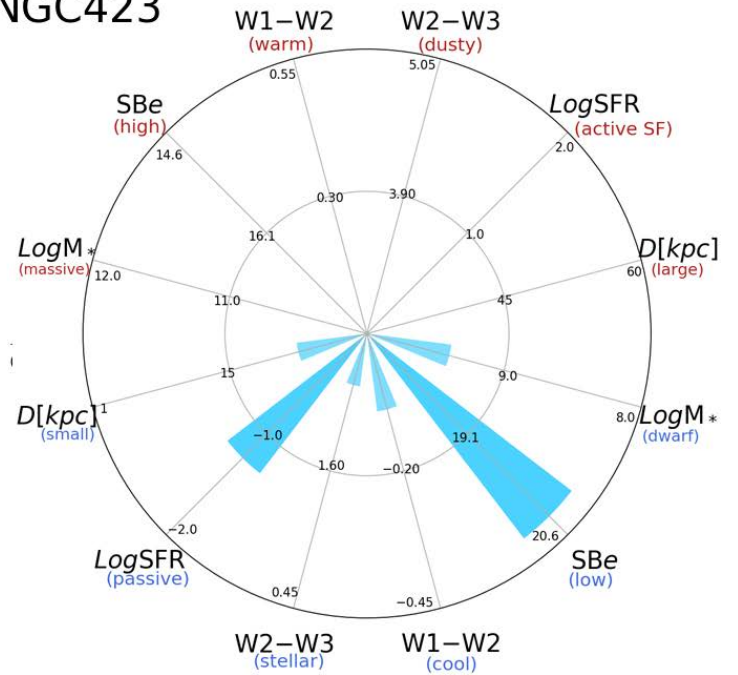


Figure 17. Physical properties of barred spiral NGC 1365 (top panel), and low surface brightness, highly-inclined galaxy NGC 4236 (bottom panel). The composite diagram shows the *WISE* 3-color view of the galaxy. The pinwheel diagram graphically displays the physical properties, with the center of the diagram representing average values for galaxies (see Table 4). The inner and outer rings demark the 50% and 100% departures from the canonical average values. In this example, NGC 1365 exhibits ‘positive’ attributes: active SF and colors, massive and extended host. In contrast, the galaxy NGC 4236 has ‘negative’ properties: minimal SF, low surface brightness, dwarf-like mass and extent.

rings demark the 50% and 100% departure value of the parameter from the typical value. The center of the diagram represents median values for galaxies in the WXSC (defined in Table 4), and so departures from the aver-

age value indicate either positive departure (upper half of diagram), or negative departure (lower half). For example, galaxies with a large SFR will have a red wedge pointing upwards, toward “active SF”; whereas galax-

Table 4. Pinwheel Diagram Reference Center

Attribute	units	median value	floor (min)	ceiling (max)
–	–	–	–	–
D	kpc	30	1	90
Log SFR	Log [$M_{\odot} \text{ yr}^{-1}$]	0	-2.0	+2.0
W2-W3	mag	2.75	0.45	5.05
W1-W2	mag	0.05	-0.45	0.55
SB _e	mag asec ⁻²	17.6	20.6	14.6
Log M _*	Log [M_{\odot}]	10.0	8.0	12.0

NOTE—The center of the pinwheel diagram has the values presented here; the median values are derived from the larger WXSC, several thousand galaxies. The exception is the central value for the Log SFR, adopted to be the approximate value of the Milky Way and its LG companion, M31.

ies with low Log SFRs will have a blue wedge pointing downward, toward “passive”. In the case of NGC 1365, it has large-valued colors indicating active star formation, somewhat high surface brightness, and is more massive and larger diameter than typical galaxies. In the Fornax Cluster, NGC 1365 stands out among its many cluster members.

In contrast, the faint galaxy, NGC 4236 in Fig. 17b, has ‘negative’ properties including low (dwarf) mass, low surface brightness, low SFR, and cool colors – indeed, there is not much going on in this physically small galaxy, but it may be quite typical for its stellar mass and evolutionary SFH phase. It is immediately apparent that NGC 1365 and NGC 4236 could not be more different galaxies in their measured and derived properties, visually (and easily) discerned with the pinwheel diagram.

In Paper II, we will present the measurements and derived properties of the WXSC, and include pinwheel diagrams for each. We will attempt to identify similar types of galaxies based on the pinwheel patterns, thereby linking their properties to their SF history and environment.

7. THE BRIGHTEST GLOBULAR CLUSTERS

For completeness we include here the brightest MW globular clusters (GCs), since many are also some of the largest and brightest objects in the sky; e.g., 47 Tucanae is a spectacular GC in the SMC field (see also Fig. 1), and Omega Centauri (NGC 5139), Figure 18a, is so large that it is effectively a dwarf satellite galaxy. Because we are unable to distinguish foreground (Milky Way) stars from those in the GCs, we measure their fluxes in a similar as was used for the Magellanic Clouds. Specifically, we compute the mean flux per pixel of the “sky” (annulus well outside of the GC), and remove that from each pixel value within the GC aperture.

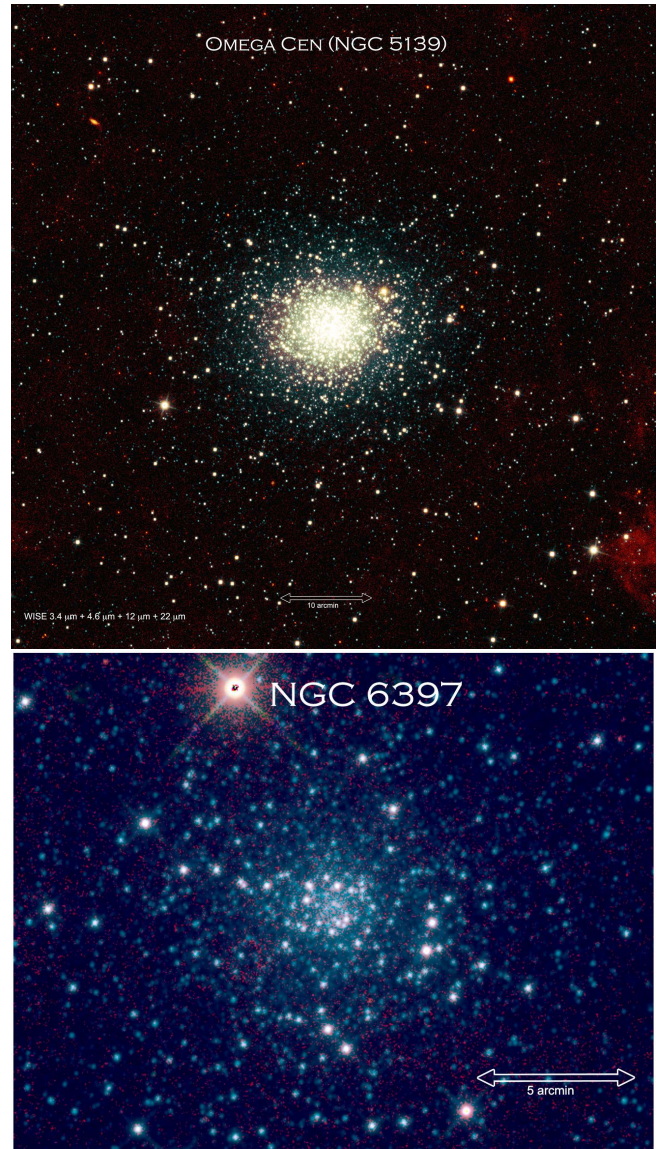


Figure 18. Nearby globular clusters Omega Centauri (a) and NGC 6397 (b), as seen with *WISE* in all four bands. Omega Cen is the brightest GC, and likely a dwarf galaxy. NGC 6397 has unusually ‘warm’ W2-W3 colors for a GC, indicating the presence of $11.3 \mu\text{m}$ PAH emission and significant dust mass, possibly arising from post-AGB shell ejection from a second generation of stars.

The resulting fluxes are shown in Table 5, which presents the 25 brightest GCs in the sky, all are part of the Milky Way system, and most of which are famed Messier objects. For simplicity, we use the same circular aperture (column 4) for all four *WISE* bands, and report the integrated flux (sky-subtracted) in Vega magnitudes, and the enclosed surface brightness. Omega Centauri (Figure 18a) is by far the brightest GC, with an integrated magnitude of +0.84 in W1 (143 Jy), while the last GC in the list, M 72, is 6.2 magnitudes fainter (0.5

Jy). A common property of GCs is their relatively uniform color, due to the dominate population – evolved, low-mass stars – the last survivors of these ancient star clusters; note how Omega Centauri and 47 Tucanae (Fig. 1) appear homogenous in apparent properties, but with the occasional dusty (shell-enshrouded) red giant standing out. Nevertheless, there is a slight spread in color across the 25 Brightest GCs, which would reflect accordingly the range in globular cluster ages and metallicities.

For this sample the mean colors are $+0.002 \pm 0.011$ and -0.101 ± 0.161 for W1–W2 and W2–W3 respectively, which would land at the extreme “blue” end of the galaxy color plot, indicated in Fig. 10. As some of the oldest known objects in the Universe, GCs have low-mass, evolved member populations, and correspondingly similar colors to spheroidal galaxies. None of the 25 brightest GCs have particularly deviant colors; however, in terms of the morphology or SF activity indicator, W2–W3 color, the GC with the warmest (red) color is NGC 6397 (Figure 18b, whose value is $+0.56 \pm 0.02$ mag, about 3σ warmer than the mean color for GCs.

One of the closest GCs relative to the Sun (~ 2.2 kpc; [Alcaino et al. \(1997\)](#)), NGC 6397 has the typical GC appearance of a strongly contracted core; see Figure 18b.

Upon closer inspection of the W3 ($12\mu\text{m}$) band, there is diffuse emission in the inner $\sim 3'$, consistent with the high(est) surface brightness (SBw3) seen in the sample (see Table 5). The presence of $11.3\mu\text{m}$ PAH or mid-IR continuum emission indicates significant dust in the inter-GC medium, and consequently moving NGC 6397 to the right of the GC mean in the color plot (Fig. 10). Possibly arising from post-AGB shell ejection from a second generation of stars ([Milone et al. 2012](#)), this dust emission is diffuse and relatively weak (compared to W1 and W2), but the relatively close proximity allows clear detection with *WISE*. Note that for M4, the closest GC system to the Sun (also ~ 2 kpc), does not indicate any excess W3 emission – 18.08 versus 16.08 mag/arcsec² in comparison to NGC 6397 (see Table 5) – and hence is unlikely to have a significant post-AGB population (see also [Maclean et al. 2016](#)). A detailed analysis of the GC properties is beyond the scope of this present work, but this exercise of measuring the brightest GCs shows that interesting outliers, such as NGC6397, can be discerned and identified from the general photometric properties.

Table 5. Brightest Globular Clusters

Cluster	R.A. deg	Dec deg	R_{W1} arcmin	$m1 \pm \Delta m1$ mag	SB1 mag · sec ⁻²	$m2 \pm \Delta m2$ mag	SB2 mag · sec ⁻²	$m3 \pm \Delta m3$ mag	SB3 mag · sec ⁻²	$m4 \pm \Delta m4$ mag	SB4 mag · sec ⁻²
NGC5139	201.69121	-47.47686	27.50	0.84 0.01	18.17	0.84 0.01	18.17	1.02 0.01	17.03	0.96 0.02	16.71
NGC0104	6.02233	-72.08144	25.00	1.17 0.01	18.29	1.20 0.01	18.33	1.13 0.01	16.89	0.99 0.01	15.73
MESSIER22	279.10086	-23.90341	10.83	1.92 0.01	17.23	1.82 0.01	17.12	1.70 0.01	16.44	-0.25 0.01	14.00
MESSIER04	245.89751	-26.52552	9.83	2.72 0.01	17.81	2.61 0.01	17.71	2.99 0.04	18.08	2.22 0.05	16.47
NGC6397	265.17233	-53.67369	11.67	3.11 0.01	18.58	3.03 0.01	18.50	2.47 0.01	16.43	3.42 0.06	17.38
NGC2808	138.01060	-64.86282	9.17	3.13 0.01	18.08	3.13 0.01	18.07	2.73 0.01	17.47	1.95 0.01	16.46
NGC6752	287.71576	-59.98185	10.00	3.16 0.01	18.29	3.13 0.01	18.26	3.26 0.01	18.20	3.67 0.10	18.18
MESSIER05	229.64064	2.08268	12.50	3.49 0.01	19.11	3.50 0.01	19.12	3.34 0.01	18.08	3.88 0.04	17.11
MESSIER13	250.42139	36.45853	10.83	3.57 0.01	18.88	3.58 0.01	18.89	3.66 0.01	17.91	3.67 0.07	17.63
MESSIER10	254.28746	-4.09933	10.17	3.58 0.01	18.75	3.57 0.01	18.74	3.69 0.02	17.94	3.69 0.03	15.81
MESSIER14	264.40067	-3.24592	8.75	3.65 0.01	18.50	3.65 0.01	18.49	3.73 0.02	17.36	3.05 0.03	15.80
NGC0362	15.80930	-70.84821	8.67	3.98 0.01	18.80	3.98 0.01	18.80	3.88 0.01	18.39	3.83 0.05	17.06
MESSIER55	294.99750	-30.96208	8.67	4.02 0.01	18.84	4.01 0.01	18.84	4.20 0.01	18.31	5.13 0.19	17.88
MESSIER03	205.54803	28.37712	10.83	4.06 0.01	19.37	4.07 0.01	19.38	3.98 0.01	17.61	3.95 0.04	16.70
MESSIER15	322.49323	12.16683	9.00	4.13 0.01	19.03	4.12 0.01	19.02	4.14 0.01	18.65	4.47 0.08	17.22
MESSIER12	251.81049	-1.94782	8.33	4.14 0.01	18.87	4.14 0.01	18.87	4.43 0.03	18.55	4.27 0.11	17.89
MESSIER02	323.36255	-0.82332	7.50	4.15 0.01	18.66	4.16 0.01	18.66	4.29 0.01	17.92	4.21 0.07	16.96
MESSIER92	259.28030	43.13652	9.58	4.34 0.01	19.38	4.33 0.01	19.37	4.58 0.02	17.04	4.54 0.04	16.67
MESSIER80	244.26045	-22.97511	5.83	4.53 0.01	18.49	4.52 0.01	18.49	4.83 0.03	16.96	4.14 0.04	15.59
MESSIER54	283.76364	-30.47850	5.42	4.63 0.01	18.43	4.55 0.01	18.35	4.27 0.01	17.50	3.94 0.04	16.06
MESSIER107	248.13298	-13.05363	7.50	4.79 0.01	19.30	4.82 0.01	19.33	5.54 0.10	18.00	7.03 0.54	18.27
MESSIER53	198.23013	18.16912	10.42	5.43 0.02	20.66	5.43 0.04	20.66	5.35 0.02	19.32	5.15 0.08	16.87
MESSIER79	81.04414	-24.52423	5.17	5.60 0.01	19.30	5.60 0.01	19.30	6.42 0.10	19.17	5.41 0.17	18.15
NGC0288	13.19106	-26.58730	7.83	5.80 0.01	20.40	5.80 0.01	20.41	5.97 0.03	19.45	6.26 0.43	19.01
MESSIER72	313.36630	-12.53706	2.92	7.02 0.01	19.48	7.05 0.01	19.51	7.35 0.03	18.36	7.47 0.35	17.21

NOTE—Coordinates are in J2000; photometry with circular apertures, radius R_{W1} ; SB is the mean surface brightness for the photometric aperture.

8. SUMMARY

Building upon the early pilot study of Jarrett et al. (2013), this is the first paper in a series that encompasses the *WISE* Extended Source Catalogue (WXSC) data release, here showcasing the 100 largest angular-diameter galaxies. These objects are unique in that we are able to discern parsec and sub-kpc scales with high signal-to-noise due to their apparent brightness and proximity, notably for the Local Group ($D < 1$ Mpc) and Local Volume (< 10 Mpc), enabling high fidelity study of their internal composition and galactic ‘ecosystem’. In this study we measure their global properties, including flux, surface brightness and colors, as well as their two-component axi-symmetric radial distribution.

The largest of the large are the Magellanic Clouds and the Andromeda Galaxy, which are also the (integrated) brightest galaxies in the sky by several orders of magnitude. From their apparent measurements and estimated distance, we derive physical properties such as luminosity, stellar mass, and star formation rate, and compare the largest galaxies with a statistically significant sample of bright nearby galaxies. We have created a visual diagram for each galaxy that simultaneously depicts the key global properties, which we envision using to categorize and group galaxies with common evolutionary traits. Finally, we present the largest and brightest Milky Way globular clusters, integrated measurements of size, flux, color and surface brightness.

To summarize the main results, we have investigated and presented the following:

1. We have constructed a whole-sky atlas of (chiefly) nearby, bright galaxies and globular clusters called the *WISE* Extended Source Catalogue (WXSC). For each source, we have constructed new – deep and wide – mosaics from which to measure and characterize the target galaxy, as well as sources that are nearby in projected radial distance. To date, we have measured over 70,000 sources. For the first release, we choose the largest angular galaxies in the sky, starting from the Magellanic Clouds, to the major Local Group galaxies such as M31 and M33, to nearby galaxy groups and clusters (Virgo and Fornax). The WXSC will allow us to compare the most well-studied galaxies with large and more distant galaxies samples from *WISE*, *Spitzer*, *Herschel*, *Euclid*, LSST, *JWST*, and the SKA pathfinders.
2. We have measured the global and internal radial brightness properties of the 100 largest galaxies based on the *WISE* W1 ($3.4 \mu\text{m}$) $1-\sigma_{\text{sky}}$ isophotal radius (about $23 \text{ mag arcsec}^{-2}$), which typically

reaches axi-symmetric-averaged depths of $25 \text{ mag arcsec}^{-2}$, or approximately $28 \text{ mag arcsec}^{-2}$ in the AB system. We present the results for angular diameters, integrated flux from isophotes and “total” extractions from both asymptotic apertures and fitting to the radial profile to levels below the noise, surface brightness, and colors, W1–W2 and W2–W3. The Magellanic Clouds, M31, and M33 are large enough that special methods were required to extract their light from the intervening foreground Galactic emission.

3. Because of the high quality measurements from the largest and brightest galaxies in the sky (WXSC), the *WISE* color-color diagram reveals a tight sequence that represents galaxy morphology and star-formation history, including present-day activity. We use the rest-frame-corrected measurements from the largest and highest S/N galaxies to fit the functional form of this *WISE* color-color “sequence”, given by: $(W1 - W2) = [0.015 \times e^{\frac{(W2 - W3)}{1.38}}] - 0.08$. Offsets from the sequence arise from the usual photometric scatter, and more meaningfully, from excess infrared emission associated with nuclear activity from AGN and starbursts.
4. The sample is sub-divided by the *WISE* colors, which serve as proxies for four general types of galaxies: bulge-dominated spheroidals, intermediate semi-quiescent disk, SF spirals, and AGN-dominated systems. Physical properties and attributes are computed based on their distance, notably the diameter, aggregate stellar mass and the dust-obscured star formation rate. We use this classification scheme to study their global properties: effective surface brightness, size, bulge-to-disk ratios, luminosity. We compare the half-light radii and surface brightnesses between *WISE* W1 ($3.4 \mu\text{m}$) and 2MASS ($2.2 \mu\text{m}$) measurements, showing that W1 radii are much larger and surface brightnesses much fainter than those extracted from the less sensitive 2MASS imaging, notably for dwarf and low-surface brightness galaxies.
5. We find that the global properties are not remarkable compared to galaxies in the local universe, except in the sense that we can detect and discern the smallest and lowest-mass dwarf and satellite galaxies because of their close proximity. Nevertheless, the 100 largest galaxies include bright cluster (Virgo and Fornax) galaxies (which have enormous diameters, >100 kpc, very high B/T ratios, and aggregate stellar masses; NGC 1316 is the

- most massive), starbursts (such as NGC 253 and M 82 with SFRs ten times the rate of the Milky Way), and AGN (e.g. Circinus and NGC 1068, with surface brightnesses that are so bright that they image-saturate in the mid-IR).
6. In terms of the star formation history, the 100 largest galaxies tend to have lower specific-SFRs compared to field galaxies, notably compared to a much larger sample of nearby galaxies belonging to the WXSC and compared to deeper redshift-selected samples, such as those from GAMA G12 (Jarrett et al. 2017).
 7. The low mass end is dominated by dwarf spheroids (e.g., NGC 0185), which have very low SFRs and hence, slowly building their bulge population. Early-type disk galaxies, such as M 81, are passively building with rates that fall below the sequence trend. Late-type spirals, such as M 83, are actively building with rates perfectly consistent with the SFH sequence observed in the GAMA G12 study.
 8. To efficiently display the attributes that we are capable of estimating with *WISE* measurements, we introduce a ‘pinwheel’ diagram that depicts the physical properties with respect to the median value observed for galaxies in the WXSC. These six attributes are the physical diameter, surface brightness, colors, SFR and stellar mass. We show that with this diagram, it is possible to delineate between different kinds of galaxies, identifying those with similar SFHs, for example. The Pinwheel Diagrams will be a featured product as

part of the WXSC image, catalog and ancillary data archive.

9. Finally, we present the 25 brightest globular clusters in the sky, for which many are also the largest and brightest objects outside of the Milky Way. Most notably Omega Centauri, 47 Tucanae and a number of famed night-sky targets (e.g., Hercules/M 13). GCs have mid-IR color properties that are similar to spheroidal galaxies, indeed Omega Centauri is essentially this type of object, indicative of their dominant evolved-stellar populations.

ACKNOWLEDGEMENTS

THJ thanks Barry Madore (and the NED team, notably Joe Mazarella) for the many wonderful and inspiring discussions of nearby galaxies over the years. He would also like to thank the incredible *WISE* team for a job well done, and notably Ned Wright, Peter Eisenhardt and Roc Cutri for creating and shepherding *WISE* from idea to brilliant reality. We thank the anonymous referee for helpful analysis suggestions. THJ acknowledge support from the National Research Foundation (South Africa). MC is a recipient of an Australian Research Council Future Fellowship (project number FT170100273) funded by the Australian Government. This research has made use of the NASA/IPAC Extragalactic Database (NED) and Wide-field Infrared Survey Explore (WISE), both of which are operated by the Jet Propulsion Laboratory, California Institute of Technology, under contract with the National Aeronautics and Space Administration, and *WISE* is also a joint project with the University of California, Los Angeles.

REFERENCES

- Alcaino, G., Liller, W., Alvarado, F., et al. 1997, *AJ*, 114, 1067
- Asabere, B., Horellou, C., Jarrett, T., & Winkler, H., 2016, *Å*, 592, a20
- Besla, G., Martinez-Delgado, D., van der Marel, R., et al. 2016, *ApJ*, 825, 20
- Bouch’e, N., Dekel, A., Genzel, R., et al. 2010, *ApJ*, 718, 1001
- Brown, M.J.I., Moustakas, J., Smith, J.D., et al. 2014, *ApJS*, 22, 18
- Brown, M.J.I., Jarrett, T. H., & Cluver, M. E. 2014, *PASA*, 31, 49
- Chauke, P. 2013, MSc dissertation, University of Cape Town
- Ching, J. H. Y., Sadler, E. M., Croom, S. M., et al. 2017, *MNRAS*, 464, 1306
- Clark, C.J.R., Verstocken, S., Bianchi, S, et al. 2018, *A&A*, 609, 37
- Cluver, M. E., Jarrett, T. H., Dale, D., et al. 2017, *ApJ*, 850, 68
- Cluver, M. E., Jarrett, T. H., Hopkins, A. M., et al. 2014, *ApJ*, 782, 90
- Cluver, M. E., et al. 2013, *ApJ*, 765, 93
- Cutri, R. M., Wright, E. L., Conrow, T., et al. 2012, Explanatory Supplement to the *WISE* All-Sky Data Release Products, 1
- da Cunha, E., et al. 2016, *PASA*, 34, 47

- de Vaucouleurs G., de Vaucouleurs A., Corwin H.G., Buta R.J., Paturel G., Fouque P. 1991, Springer-Verlag: New York
- Eisenhardt, P., et al. 2019, (arXIV: 1908.08902)
- Elbaz, D., Daddi, E., Le Borgne, D., et al. 2007, *A&A*, 468, 33
- Elson, E. C., Kam, S. Z., Chemin, L., Carignan, C., Jarrett, T. H. 2019, *MNRAS*, 483, 931
- For, B. Q., Koribalski, B. S., Jarrett, T. H. 2016, *MNRAS*, 425, 1934
- Hall, C., Courteau, S., Jarrett, Thomas, et al. 2018, *ApJ*, 865, 154
- Heald, G., de Blok, W. J. G.; Lucero, D, et. al. 2016, *MNRAS*, 462, 1238
- Hopkins, A. M., & Beacom, J. F. 2006, *ApJ*, 651, 142
- Huang, T., Goto, T., Hashimoto, T. et al. 2017, *MNRAS*, 471, 4239
- Jarrett, T. H., Cluver, M.C., Magoulas, C., et al. 2017, *ApJ*, 836, 182
- Jarrett, T. H., Masci, F., Tsai, C. W., et al. 2013, *AJ*, 145, 6
- Jarrett, T. H., Masci, F., Tsai, C. W., et al. 2012, *AJ*, 144, 68
- Jarrett, T. H., Cohen, M., Masci, F., et al. 2011, *ApJ*, 735, 112
- Jarrett, T. H., Chester, T., Cutri, R., et al. 2003, *AJ*, 125, 525
- Jarrett, T. H., Chester, T., Cutri, R., et al. 2000, *AJ*, 119, 2498
- Johnson, K. E., Hibbard, J. E., Gallagher, S. C., et al. 2007, *AJ*, 134, 1522
- Kam, S.Z., , Carignan, C., Chemin, L., et al. 2017, *AJ*, in press
- Kennicutt, R. C., Calzetti, D., Aniano, G., et al. 2011, *PASP*, 123, 1347
- Kennicutt, R. C., Jr., Armus, L., Bendo, G., et al. 2003, *PASP*, 115, 928
- 2018*MNRAS*.473..776K Kettlety, T., Hesling, J., Phillipps, S., et al. 2018, *MNRAS*, 473, 776
- Kollmeier, J., et al. 2017, (arXIV:1711.03234)
- Konstantopoulos, I., 2014, (arXIV:1407.5619)
- Korsaga, M., Carignan, C.; Amram, P., Epinat, B., & Jarrett, T. H. 2018, *MNRAS*, 478, 50
- Kroupa, P. 2002, *Sci*, 295, 82
- Lacy, M., et al. 2004, *ApJS*, 154, 166
- Licquia, t. & Newman, J. 2015, *ApJ*, 806, 96
- Lucero, D. M.; Carignan, C.; Elson, E. C., et al. 2015, *MNRAS*, 450, 3935
- MacLean, B.T., Campbell, S.W., De Silva G., et al. 2016*m MNRAS*, 460, L69
- Mainzer, A., Bauer, J., Cutri, R. M., et al. 2014, *ApJ*, 792, 30
- Masci, F. 2013, *Astrophysics Source Code Library*, 2010
- Meidt, S. E., Schinnerer, E., Knapen, J. H., et al. 2012, *ApJ*, 744, 17
- Meidt, S. et al. 2014, *ApJ*, 788, 144
- Meixner, M., Gordon, K., Indebetouw, R., et al. 2006, *AJ*, 132, 2268
- Milone, A. P., Marino, A. F., Piotto, G., et al. 2012, *ApJ*, 745, 27
- Mingo, B., Watson, M., Rosen, S., et al. 2016, *MNRAS*, 462, 2631
- Neill, J.D., Seibert, M., Tully, B. et al. 2014, *ApJ*, 792, 129
- Nilsson, P., 1973, *Uppsala General Catalogue of Galaxies*, *Uppsala Astron. Obs. Ann.* 6
- Noeske, K. G., Weiner, B. J., Faber, S. M., et al. 2007, *ApJL*, 660, L43
- Noyola, E., Gebhardt, K. & Bergmann, M. 2008, *ApJ*, 676, 1008
- Ogle, P., Jarrett, T.H., Lanz, L. et al. 2019, *ApJ*, 884, L11
- Parkash, V., Brown, M.J., Jarrett, T.H., & Bonne, N.J. 2018, *ApJ*, 864, 40.
- Parkash, V., Brown, M.J., Jarrett, T.H., et al. 2019, *MNRAS*, 485, 3169
- Peng, Y., Maiolino, R., & Cochrane, R. 2015, *Nature*, 521, 192.
- Ponomereva, A.A., Verheijen, M.A.W., Reynier, F., Bosma, A. 2017, *MNRAS*, submitted (arXiv:1704.08788)
- Querejeta, M., Meidt, S. E., Schinnerer, E., et al. 2015, *ApJS*, 219, 5
- Satyapal, S., Abel, N., Secrest, N.J. 2018, *ApJ*, 858, 38
- Silva, L., et al. 1998, *ApJ*, 509, 103
- Sheth, K., Regan, M., Hinz, J. et al. 2010, *PASP*, 122, 1397
- Stern, D., Assef, R. J., Benford, D. J., et al. 2012, *ApJ*, 753, 30
- Taylor, E. N., Hopkins, A. M., Baldry, I. K., et al. 2011, *MNRAS*, 418, 1587
- Tsai, C.W., Eisenhard, P.R., Wu, J., et al. 2015, *ApJ*, 805, 90
- Tomicic, N., Ho, I., Kreckel, K., et al. 2019, *ApJ*, 873, 3
- Walker, L. M., Johnson, K. E., Gallagher, S. C., et al. 2010, *AJ*, 140, 1254
- Wickramasinghe, T. & Ukwatta T. N. 2010, *MNRAS*, 406, 548
- Wright, E. L., Eisenhardt, P. R. M., Mainzer, A. K., et al. 2010, *AJ*, 140, 1868
- Yan, L., Donoso, E., Tsai, C.-W., et al. 2013, *AJ*, 145, 55
- Yew, M., Filipovi, M., Roper, Q. et al. 2017, *PASA*, 35, 15

A. TOTAL FLUXES: LARGE APERTURE AND RADIAL-PROFILE FITTING PHOTOMETRY

This appendix is comprised of a table that lists the ‘total’ fluxes for the 100 largest galaxies and LG galaxies detected by *WISE* (except the Magellanic Clouds). Two methods are used to estimate total fluxes: (1) large asymptotic apertures from curve-of-growth measurements, and double-Sersic Function fitting to the axi-symmetric radial profile. The method and results are described in Section 4.1, with some statistical comparison results presented in Table 2.

Table A1. Asymptotic and Total Integrated Brightness

iS	Galaxy	R_{W1} $A_{W1} \pm \Delta$ amin mag mag	R_{W2} $A_{W2} \pm \Delta$ amin mag mag	R_{W3} $A_{W3} \pm \Delta$ amin mag mag	R_{W4} $A_{W4} \pm \Delta$ amin mag mag	$T_{W1} \pm \Delta$ mag mag	$T_{W2} \pm \Delta$ mag mag	$T_{W3} \pm \Delta$ mag mag	$T_{W4} \pm \Delta$ mag mag
(1)	(2)	(3)	(4)	(5)	(6)	(7)	(8)	(9)	(10)
3	M31	149.39 0.08 0.01	132.78 0.13 0.01	148.80 -1.95 0.01	99.38 -3.11 0.01	0.06 0.01	0.10 0.01	-2.00 0.01	-3.13 0.01
4	M33	65.32 3.03 0.01	38.83 3.00 0.01	37.28 -0.17 0.01	30.55 -1.94 0.01	3.08 0.01	3.02 0.01	-0.22 0.01	-2.02 0.01
5	NGC0253	25.27 3.46 0.01	24.39 3.26 0.01	25.13 -0.55 0.03	25.33 -2.94 0.03	3.46 0.01	3.25 0.01	-0.56 0.03	-2.95 0.03
6	NGC5128	23.45 2.99 0.01	23.36 2.98 0.01	9.08 0.41 0.01	8.32 -1.29 0.01	2.98 0.01	2.97 0.01	0.44 0.01	-1.26 0.01
7	NGC0055	23.36 5.42 0.01	23.31 5.33 0.01	18.76 2.80 0.01	18.66 0.29 0.01	5.43 0.01	5.30 0.02	2.70 0.03	0.22 0.02
8	MESSIER81	16.57 3.60 0.01	16.97 3.60 0.01	10.34 1.82 0.03	10.61 0.44 0.03	3.60 0.01	3.59 0.01	1.79 0.03	0.35 0.03
9	MESSIER101	13.01 5.22 0.01	13.62 5.10 0.01	10.38 1.61 0.01	10.28 -0.30 0.01	5.19 0.01	5.03 0.02	1.56 0.02	-0.38 0.02
10	NGC4945	15.49 4.06 0.01	14.72 3.87 0.01	12.76 0.31 0.01	13.70 -1.57 0.01	4.06 0.01	3.86 0.01	0.30 0.01	-1.58 0.01
11	IC0342	15.48 3.95 0.01	15.42 3.88 0.01	11.40 0.22 0.01	10.96 -1.83 0.01	3.93 0.01	3.85 0.01	0.09 0.03	-1.84 0.01
12	NGC1316	15.21 5.06 0.01	12.80 5.11 0.01	8.32 4.27 0.01	4.05 3.18 0.02	5.06 0.01	5.10 0.01	4.36 0.03	3.13 0.05
13	MESSIER49	15.03 4.94 0.01	12.71 5.03 0.01	9.75 4.04 0.02	3.10 3.82 0.03	4.94 0.01	5.03 0.01	4.17 0.10	3.74 0.09
14	MESSIER86	14.23 5.45 0.01	11.85 5.52 0.01	5.87 5.43 0.02	2.08 4.99 0.06	5.45 0.01	5.51 0.02	5.70 0.05	4.92 0.10
15	MAFFEI1	13.82 3.91 0.01	12.32 3.93 0.02	7.05 3.22 0.02	2.54 2.68 0.01	3.90 0.01	3.92 0.02	3.26 0.08	2.50 0.13
16	MESSIER110	13.53 5.29 0.01	12.06 5.36 0.01	12.12 4.57 0.02	12.12 3.16 0.07	5.28 0.01	5.35 0.01	4.48 0.08	3.25 0.08
17	MESSIER104	13.05 4.60 0.01	11.05 4.64 0.01	9.30 3.54 0.01	4.36 2.53 0.02	4.60 0.01	4.62 0.01	3.63 0.02	2.42 0.03
18	NGC2403	13.11 5.67 0.01	12.95 5.57 0.01	12.77 2.25 0.01	10.92 0.28 0.01	5.66 0.01	5.53 0.02	2.21 0.02	0.19 0.02
19	NGC0247	13.02 6.45 0.01	12.88 6.49 0.01	12.91 4.04 0.01	12.16 2.27 0.03	6.44 0.01	6.42 0.02	3.85 0.06	2.08 0.08
20	MESSIER106	12.52 5.22 0.01	11.95 5.18 0.01	9.93 2.75 0.01	10.57 1.09 0.01	5.22 0.01	5.16 0.01	2.68 0.02	1.00 0.03
21	MESSIER87	12.39 5.29 0.01	10.38 5.41 0.01	6.75 4.75 0.02	2.22 3.79 0.02	5.28 0.01	5.41 0.02	4.96 0.06	3.73 0.08
22	NGC3628	12.02 5.75 0.01	10.21 5.62 0.01	9.79 2.42 0.01	9.78 0.50 0.01	5.74 0.01	5.61 0.01	2.39 0.02	0.46 0.02
23	NGC0300	11.91 5.70 0.01	11.43 5.72 0.01	9.93 3.13 0.01	12.00 1.27 0.02	5.69 0.01	5.65 0.02	null null	null null
24	NGC4736	11.37 4.75 0.01	9.67 4.74 0.01	7.34 2.03 0.01	7.47 0.32 0.01	4.75 0.01	4.74 0.02	1.99 0.01	0.28 0.02
25	NGC6822	11.41 5.73 0.01	11.38 5.76 0.01	11.40 3.41 0.01	11.07 1.13 0.02	5.71 0.02	5.66 0.03	3.36 0.09	1.13 0.11
26	NGC1532	11.28 6.42 0.01	9.38 6.38 0.01	8.85 3.58 0.01	8.85 1.97 0.02	6.42 0.01	6.37 0.01	3.52 0.04	1.90 0.04
27	NGC5236	10.53 4.24 0.01	9.52 4.12 0.01	10.94 0.32 0.01	9.27 -1.86 0.01	4.24 0.01	4.11 0.01	0.31 0.01	-1.88 0.01
28	NGC0147	11.12 6.50 0.01	9.30 6.57 0.01	9.02 4.55 0.01	null null null	6.47 0.02	6.52 0.05	null null	null null
29	NGC6744	10.77 5.47 0.01	10.88 5.45 0.01	8.94 2.27 0.01	10.02 0.68 0.01	5.47 0.01	5.44 0.01	2.12 0.04	0.58 0.03
30	MESSIER63	10.36 5.25 0.01	9.94 5.19 0.01	10.17 1.87 0.01	9.89 0.24 0.01	5.24 0.01	5.16 0.01	1.85 0.01	0.20 0.02
31	NGC1553	10.41 5.85 0.01	8.69 5.95 0.01	5.72 5.19 0.01	2.69 4.24 0.02	5.87 0.01	5.96 0.01	5.26 0.02	4.13 0.05
32	NGC1399	10.23 5.80 0.01	8.68 5.90 0.01	6.00 5.28 0.02	2.45 4.77 0.04	5.80 0.01	5.88 0.01	5.51 0.04	4.69 0.06
33	NGC4236	10.36 7.84 0.01	10.32 7.94 0.01	10.38 5.93 0.03	10.35 3.06 0.04	7.81 0.02	7.80 0.05	5.67 0.09	null null
34	NGC4565	10.01 5.75 0.01	9.73 5.71 0.01	10.19 3.19 0.01	10.23 1.63 0.01	5.75 0.01	5.70 0.01	3.15 0.02	1.58 0.02
35	Maffei2	10.12 4.74 0.01	9.99 4.57 0.01	10.04 1.05 0.01	10.15 -1.06 0.01	4.74 0.01	4.57 0.01	1.01 0.02	-1.07 0.01
36	NGC4631	9.88 5.99 0.01	9.41 5.80 0.01	9.92 1.98 0.01	9.72 -0.07 0.01	5.99 0.01	5.78 0.01	1.96 0.01	-0.10 0.01
37	MESSIER60	9.69 5.37 0.01	8.18 5.42 0.01	6.31 4.33 0.02	2.59 3.85 0.04	5.36 0.01	5.41 0.02	4.76 0.11	3.77 0.12
38	NGC4636	9.59 6.05 0.01	8.04 6.13 0.01	6.47 5.00 0.02	1.98 4.69 0.05	6.04 0.01	6.11 0.02	5.11 0.13	4.78 0.17
39	NGC2768	9.52 6.74 0.01	7.97 6.77 0.01	5.90 6.20 0.03	2.15 5.50 0.06	6.72 0.01	6.76 0.02	6.45 0.07	5.41 0.09
40	NGC3585	9.43 6.26 0.01	7.97 6.35 0.01	5.70 5.74 0.03	1.61 5.28 0.07	6.25 0.01	6.34 0.02	5.90 0.07	5.10 0.08
41	ESO270-G017	9.52 8.41 0.01	7.96 8.51 0.01	7.26 6.10 0.02	7.26 3.91 0.04	8.36 0.03	8.45 0.08	6.09 0.10	3.85 0.07
42	MESSIER51a	9.22 5.07 0.01	9.09 4.96 0.01	9.09 1.18 0.01	8.98 -0.62 0.01	5.08 0.01	4.94 0.01	1.16 0.01	-0.65 0.01
43	NGC3115	9.06 5.58 0.01	7.67 5.60 0.01	5.68 4.55 0.01	1.88 4.52 0.03	5.58 0.01	5.59 0.02	4.68 0.08	4.49 0.04
44	NGC3923	9.15 5.95 0.01	7.66 6.07 0.01	5.91 5.43 0.03	1.58 5.29 0.07	5.95 0.01	6.06 0.02	5.93 0.09	5.16 0.09
45	NGC4365	8.92 6.25 0.01	7.54 6.38 0.01	1.25 6.75 0.01	1.02 5.77 0.05	6.24 0.01	6.38 0.02	6.75 0.03	5.56 0.12
46	NGC1313	8.91 6.68 0.01	8.93 6.62 0.01	8.96 3.44 0.01	8.96 0.98 0.01	6.66 0.01	6.57 0.02	3.35 0.05	0.90 0.04
47	MESSIER84	8.93 5.71 0.01	7.45 5.76 0.01	4.68 5.42 0.02	1.56 4.77 0.05	5.70 0.01	5.79 0.01	5.64 0.04	4.72 0.09
48	NGC0185	8.92 6.19 0.01	7.44 6.27 0.01	5.84 5.25 0.02	2.47 4.55 0.04	6.16 0.02	6.26 0.02	5.36 0.03	4.38 0.08
49	NGC6946	8.84 5.00 0.01	8.88 4.82 0.01	7.96 0.94 0.01	8.71 -1.04 0.01	5.00 0.01	4.80 0.01	0.93 0.01	-1.07 0.01
50	NGC1395	8.88 6.43 0.01	7.43 6.51 0.01	5.67 5.85 0.02	1.52 5.37 0.07	6.42 0.01	6.51 0.02	6.24 0.06	5.28 0.10

NOTE—columns: (1) order of W1 3.4 μ m isophotal angular size, see Table 1; (2) galaxy name; (3-6) W1, W2, W3, and W4 (respectively), asymptotic measurements: Radius (arcmin), magnitude and its uncertainty; (7-10) total magnitude and its uncertainty (W1, W2, W3, W4, respectively) estimated using a double-Sersic fitting to the radial surface brightness profile.

Table A1. ... continued: Asymptotic and Total Integrated Brightness

iS	Galaxy	R _{W1} A _{W1} ± Δ	R _{W2} A _{W2} ± Δ	R _{W3} A _{W3} ± Δ	R _{W4} A _{W4} ± Δ	T _{W1} ± Δ	T _{W2} ± Δ	T _{W3} ± Δ	T _{W4} ± Δ
(1)	(2)	amin mag (3)	amin mag (4)	amin mag (5)	amin mag (6)	mag (7)	mag (8)	mag (9)	mag (10)
51	IC0010	8.73 5.08 0.01	8.38 5.01 0.01	5.53 2.28 0.01	4.62 -0.35 0.01	5.07 0.01	5.01 0.01	2.30 0.01	-0.35 0.01
52	NGC4517	8.57 7.07 0.01	8.55 6.98 0.01	8.64 3.89 0.01	8.61 2.10 0.02	7.07 0.01	6.96 0.01	3.84 0.03	2.02 0.02
53	NGC1291	8.62 5.34 0.01	8.65 5.39 0.01	6.22 4.29 0.01	8.09 3.09 0.05	5.33 0.01	5.37 0.01	4.20 0.06	3.02 0.10
54	NGC2683	8.40 6.13 0.01	7.46 6.08 0.01	7.47 3.77 0.01	3.88 2.56 0.01	6.13 0.01	6.06 0.01	3.73 0.02	2.56 0.03
55	NGC4697	8.51 5.98 0.01	7.12 6.05 0.01	4.98 5.50 0.02	1.58 4.72 0.04	5.96 0.01	6.03 0.02	5.83 0.06	4.61 0.14
56	NGC3521	8.39 5.43 0.01	7.13 5.35 0.01	5.87 1.96 0.01	5.90 0.31 0.01	5.42 0.01	5.35 0.01	1.94 0.01	0.27 0.02
57	NGC3109	8.50 7.93 0.01	8.49 7.95 0.01	8.26 6.63 0.05	null null null	7.89 0.03	7.80 0.05	null null	null null
58	NGC0891	8.27 5.50 0.01	8.43 5.29 0.01	8.49 1.95 0.01	8.47 0.22 0.01	5.50 0.01	5.29 0.01	1.93 0.01	0.19 0.01
59	MESSIER85	8.43 5.78 0.01	7.08 5.82 0.01	5.33 5.29 0.02	2.07 4.41 0.04	5.77 0.01	5.81 0.01	5.45 0.05	4.36 0.10
60	NGC4244	8.47 7.48 0.01	8.45 7.43 0.01	8.46 5.32 0.01	7.52 3.26 0.03	7.47 0.01	7.39 0.03	5.18 0.05	3.11 0.07
61	NGC4762	8.41 7.09 0.01	7.09 7.14 0.01	5.18 6.43 0.03	1.92 5.98 0.10	7.09 0.01	7.12 0.02	6.73 0.07	5.88 0.09
62	NGC5084	8.13 6.81 0.01	8.15 6.83 0.01	8.22 5.41 0.02	8.15 3.93 0.08	6.80 0.01	6.79 0.02	5.44 0.09	4.08 0.08
63	NGC5907	7.91 6.46 0.01	8.04 6.34 0.01	8.05 3.22 0.01	8.03 1.55 0.01	6.46 0.01	6.34 0.01	3.20 0.01	1.52 0.02
64	NGC4395	8.04 7.70 0.01	8.02 7.73 0.01	7.98 5.43 0.03	7.77 2.99 0.05	7.67 0.02	7.58 0.07	5.34 0.09	2.97 0.11
65	NGC1407	7.92 6.19 0.01	6.61 6.28 0.01	5.28 5.55 0.03	1.53 5.38 0.08	6.18 0.01	6.27 0.02	5.95 0.09	5.25 0.10
66	NGC3627	7.83 5.55 0.01	6.56 5.45 0.01	6.14 2.02 0.01	6.15 0.01 0.01	5.54 0.01	5.44 0.01	2.00 0.01	-0.02 0.02
67	NGC4438	7.76 6.77 0.01	6.58 6.77 0.01	5.53 5.03 0.01	2.23 3.78 0.02	6.76 0.01	6.71 0.02	5.20 0.05	3.73 0.05
68	NGC1365	7.79 6.03 0.01	7.43 5.74 0.01	7.65 2.11 0.01	7.40 -0.46 0.01	6.02 0.01	5.73 0.01	2.09 0.01	-0.48 0.01
69	NGC2903	7.57 5.66 0.01	7.75 5.57 0.01	7.70 2.06 0.01	7.68 0.09 0.01	5.66 0.01	5.56 0.01	2.03 0.01	0.05 0.02
70	NGC5846	7.68 6.38 0.01	6.45 6.47 0.01	4.59 6.08 0.03	1.41 5.69 0.07	6.36 0.01	6.47 0.03	6.37 0.08	5.52 0.10
71	NGC4725	7.67 6.07 0.01	6.46 6.12 0.01	5.22 3.99 0.01	4.09 2.60 0.02	6.06 0.01	6.11 0.01	3.90 0.02	2.50 0.03
72	NGC1549	7.66 6.33 0.01	6.80 6.43 0.01	5.63 5.64 0.01	2.27 5.16 0.04	6.33 0.01	6.41 0.01	5.90 0.08	5.04 0.07
73	WLM	7.70 8.85 0.01	7.68 8.93 0.02	7.69 8.17 0.22	4.97 5.36 0.17	8.79 0.03	8.75 0.07	null null	null null
74	NGC2841	7.68 5.88 0.01	6.33 5.89 0.01	4.68 3.78 0.01	5.90 2.17 0.02	5.87 0.01	5.88 0.01	3.74 0.01	2.10 0.03
75	CircinusGalaxy	7.62 4.39 0.01	7.61 3.74 0.01	11.02 -0.31 0.04	10.28 -2.59 0.04	4.37 0.02	3.73 0.01	-0.31 0.04	-2.60 0.04
76	NGC3621	7.58 6.32 0.02	6.32 6.18 0.02	6.24 2.55 0.01	6.24 0.83 0.01	6.31 0.02	6.15 0.02	2.52 0.01	0.78 0.02
77	NGC5078	7.56 6.69 0.01	6.32 6.65 0.01	4.59 4.00 0.01	3.26 2.44 0.01	6.68 0.01	6.64 0.01	4.01 0.01	2.40 0.02
78	NGC1023	7.53 6.03 0.01	6.27 6.09 0.01	3.69 5.62 0.02	1.92 4.93 0.05	6.03 0.01	6.09 0.01	5.72 0.07	4.78 0.08
79	NGC7331	7.45 5.69 0.01	7.21 5.60 0.01	7.25 2.35 0.01	7.18 0.66 0.01	5.69 0.01	5.59 0.01	2.33 0.01	0.62 0.01
80	MESSIER64	7.18 5.18 0.01	6.14 5.17 0.01	5.95 2.95 0.01	5.96 1.19 0.01	5.18 0.01	5.17 0.01	2.91 0.02	1.15 0.02
81	MESSIER59	7.21 6.43 0.01	6.11 6.51 0.01	4.53 5.31 0.02	1.73 5.09 0.07	6.42 0.01	6.51 0.02	5.41 0.12	5.06 0.07
82	NGC4696	7.18 6.64 0.01	6.05 6.70 0.01	5.09 5.92 0.02	1.94 5.37 0.06	6.63 0.01	6.69 0.01	6.35 0.09	5.32 0.14
83	MESSIER82	6.92 4.06 0.01	6.82 3.61 0.01	9.00 -0.96 0.01	8.81 -4.14 0.01	4.06 0.01	3.61 0.01	-0.97 0.01	-4.14 0.01
84	ESO274-001	7.07 7.82 0.01	7.07 7.85 0.01	3.29 6.36 0.03	3.38 3.01 0.01	7.77 0.33	7.77 0.09	6.65 0.09	2.98 0.02
85	MESSIER77	6.60 4.59 0.01	5.01 2.89 0.01	6.94 -0.68 0.04	7.33 -2.45 0.04	4.59 0.01	2.89 0.01	-0.68 0.04	-2.45 0.04
86	NGC3077	6.95 6.77 0.01	5.84 6.71 0.01	4.53 3.98 0.01	3.16 1.61 0.01	6.76 0.01	6.69 0.02	4.00 0.02	1.58 0.02
87	MESSIER65	6.95 5.89 0.01	5.88 5.91 0.01	5.85 4.14 0.01	5.88 2.74 0.03	5.89 0.01	5.90 0.01	4.09 0.02	2.64 0.04
88	NGC7213	6.91 6.46 0.01	5.82 6.41 0.01	4.02 4.23 0.01	2.64 2.42 0.01	6.45 0.01	6.41 0.02	4.26 0.02	2.38 0.07
89	IC0356	6.74 5.76 0.01	5.92 5.76 0.01	3.09 3.74 0.01	5.96 1.91 0.02	5.74 0.01	5.75 0.01	3.56 0.02	1.81 0.04
90	NGC1560	6.90 8.56 0.01	5.82 8.69 0.01	3.03 7.15 0.05	1.88 5.35 0.04	8.55 0.01	8.67 0.02	null null	null null
91	NGC2663	6.90 6.22 0.01	6.00 6.32 0.01	5.06 5.86 0.03	1.43 4.90 0.04	6.21 0.01	6.29 0.02	6.30 0.04	4.83 0.04
92	NGC4216	6.92 6.36 0.01	5.73 6.37 0.01	5.62 4.22 0.01	5.30 2.89 0.02	6.35 0.01	6.36 0.01	4.16 0.02	2.78 0.03
93	NGC1055	6.79 6.74 0.01	6.49 6.63 0.01	6.82 3.06 0.01	6.77 1.30 0.01	6.74 0.01	6.60 0.01	3.04 0.01	1.27 0.02
94	NGC5170	6.73 7.42 0.01	5.67 7.40 0.01	5.68 5.21 0.01	5.19 3.79 0.03	7.41 0.01	7.39 0.01	5.14 0.03	3.61 0.04
95	MESSIER98	6.62 6.70 0.01	6.69 6.66 0.01	6.77 3.81 0.01	6.73 2.19 0.02	6.70 0.01	6.64 0.01	3.77 0.02	2.11 0.03
96	NGC2997	6.73 6.13 0.01	6.54 6.02 0.01	6.57 2.34 0.01	6.74 0.53 0.01	6.13 0.01	6.00 0.01	2.30 0.01	0.48 0.02
97	NGC4125	6.68 6.48 0.01	5.62 6.55 0.01	3.89 5.98 0.02	1.42 5.20 0.04	6.48 0.01	6.54 0.01	6.10 0.05	5.00 0.07
98	NGC7793	6.72 6.50 0.01	6.62 6.41 0.01	5.99 3.21 0.01	4.68 1.54 0.01	6.50 0.01	6.38 0.01	3.16 0.01	1.47 0.02
99	NGC5363	6.65 6.55 0.01	5.60 6.58 0.01	3.55 5.46 0.01	1.79 4.30 0.03	6.54 0.01	6.56 0.02	5.57 0.03	4.23 0.07
100	NGC4217	6.69 7.21 0.01	5.60 7.05 0.01	5.01 3.72 0.01	5.02 2.05 0.01	7.20 0.01	7.05 0.01	3.71 0.01	2.04 0.02
101	IC1613	5.62 8.35 0.01	5.56 8.59 0.02	2.53 8.31 0.12	null null null	8.26 0.06	8.41 0.09	null null	null null
102	MESSIER32	4.32 5.01 0.01	3.56 5.07 0.01	3.49 4.42 0.01	1.90 3.57 0.03	5.01 0.01	5.06 0.01	4.37 0.02	3.49 0.04
103	UGC05373	3.46 9.65 0.01	2.92 9.66 0.02	null null null	2.11 6.39 0.33	9.57 0.04	9.56 0.09	null null	null null
104	ESO245-007	2.61 10.88 0.02	2.61 11.12 0.04	null null null	null null null	10.53 0.10	null null	null null	null null

NOTE—columns: (1) order of W1 3.4 μm isophotal angular size, see Table 1; (2) galaxy name; (3-6) W1, W2, W3, and W4 (respectively), asymptotic measurements: Radius (arcmin), magnitude and its uncertainty; (7-10) total magnitude and its uncertainty (W1, W2, W3, W4, respectively) estimated using a double-Sersic fitting to the radial surface brightness profile.

B. SEDS OF A CLASSIC GALAXY TYPES

Four examples of galaxies that represents the *WISE* color sets (Fig. 10), comprising spheroids, intermediate-SF, active-SF disks, and AGN-dominated. The SEDs are constructed from 2MASS XSC and *WISE* global measurements, and templates that best fit the data. Since these Brown et al. (2014a) templates have real mid-infrared spectral data from *Spitzer*-IRS, they are accurate representations of the emission and continuum features. Also indicated are the *WISE* relative system response curves (RSRs), here normalized to unity for easy comparison. Note that the actual throughput quantum efficiency is significantly different, with W1 the most sensitive band, followed closely by W2, and the long wave-bands considerably less sensitive (Jarrett et al. 11). The $12\ \mu\text{m}$ W3 detector, however, makes up for less sensitivity by having a very wide band, enclosing molecular emission and dust continuum components.

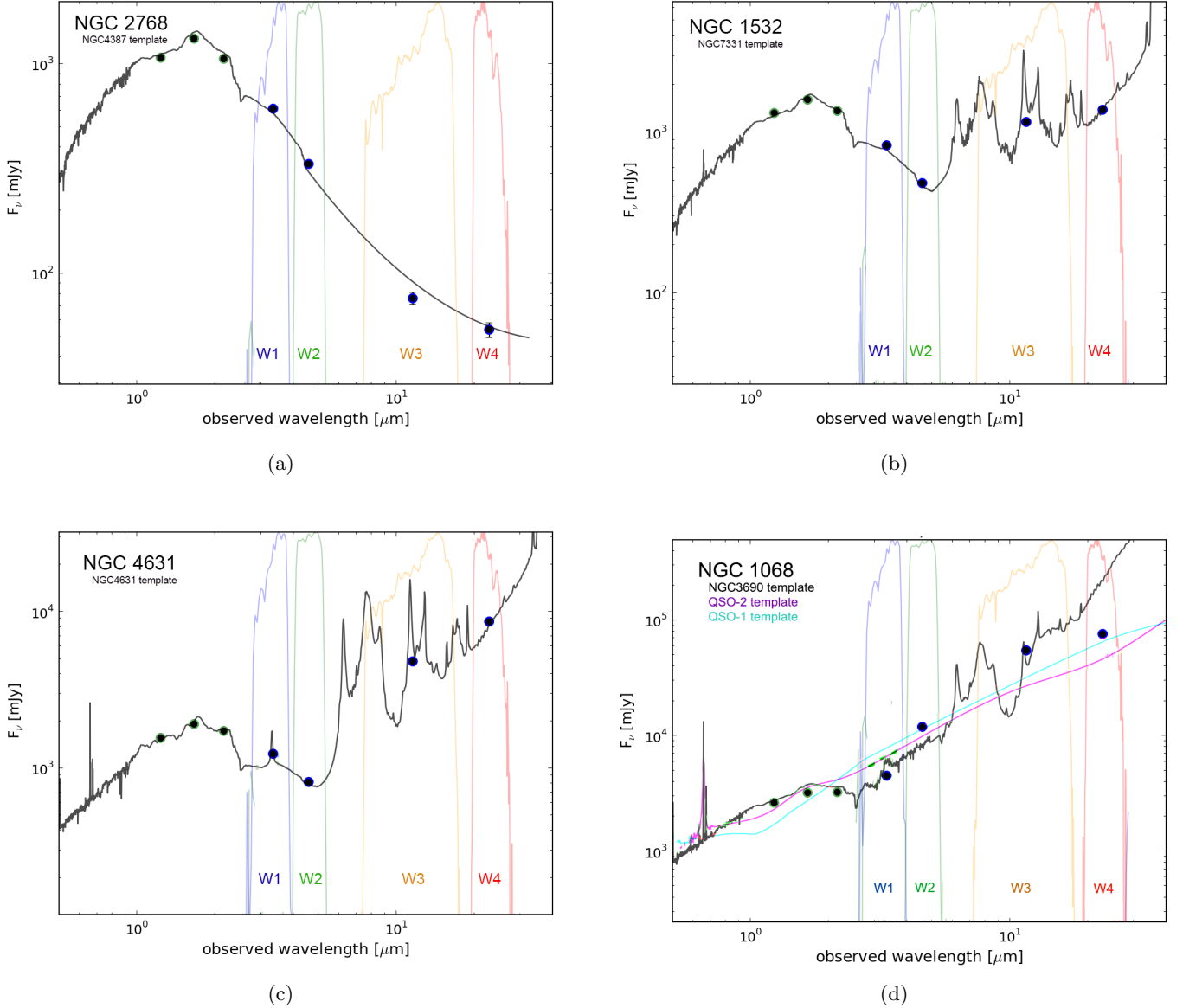


Figure 19. Infrared spectral energy distributions of four galaxies, demonstrating the broad classification revealed by *WISE* colors. (a) The first is a typical early-type elliptical galaxy, stellar-bulge dominated; (b) the second is an intermediate (Sb) galaxy; (c) the third is a late-type (Sd), SF-dominated spiral, and (d) the last demonstrates an AGN-dominated host galaxy. The data points are global measurements from 2MASS XSC and *WISE* (this study). The “template” is a best fit to the data, from the Brown et al. (2014a) and GRASIL (Silva et al. 1998) suite of spectral-templates. The *WISE* filter bands (normalized to unity) are indicated for each.

C. DATA PRODUCTS OF THE WXSC

Images: The foundation of the WXSC are the native-resolution mosaics, constructed specifically for resolved galaxies. For each galaxy, the images range in size from 0.25 degrees to many degrees (e.g., LG galaxies), large enough to encompass the galaxy and its local environment. The pixel scale is 1 arcsec, except for the Magellanic Clouds (8 arcsec) and M31 (1.5 arcsec). The flux calibration is in the Vega system, and the zero point magnitude is in the FITS header. The orientation is standard, and the headers have full WCS information.

There are four bands of *WISE*, for each band we construct three kinds of images: integrated signal (INT), the corresponding uncertainty (UNC) and the frame coverage (COV).

Processing includes identification and removal of foreground stars, background galaxies and neighboring (satellite) galaxies, as well as the (rare) artifact or image glitch. These ‘cleaned’ images are also part of the available data products, and are used to measure and study the target galaxy.

Photometry and Catalogued Values: Full source characterization is carried out on the cleaned images, featuring size, shape, integrated fluxes, surface brightness, and a number of other measurements. A README detailing the catalog columns is part of the data release. For those galaxies with a distance (either redshift-independent, or a redshift-based luminosity distance), physical attributes (luminosities, SFRs, stellar mass) are derived from k-corrected fluxes. The k-correction is carried out using templates and SED fitting (see Jarrett et al. (2017) for more details). Likewise, there is a README file that details the physical values in a separate ‘derived’ catalog.

Ancillary Products: The images and catalogs are the primary data products, but there are a number of other useful products. 3-color (RGB) images of the WXSC galaxies that show the before and after star removal, SEDs where the flux data are plotted and compared with the best-fit SED template, and the pinwheel diagrams (see below), that graphically show the physical attributes of the galaxy with respect to the mean values of the greater WXSC sample (Table 4).

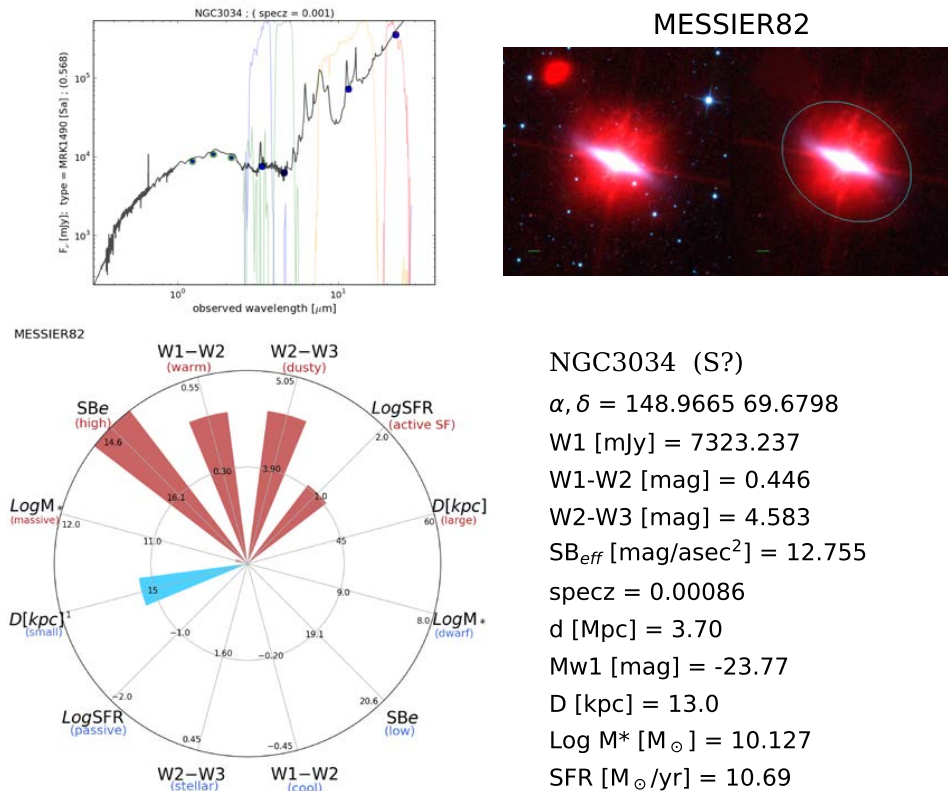


Figure 20. Physical properties of starburst NGC 3034 (M82). The image shows the *WISE* view before/after star subtraction. The ellipse denotes the $1-\sigma_{\text{sky}}$ isophote aperture. The spectral energy distribution includes the four wise band measurements, three 2MASS measurements and the best-fit galaxy template.

D. 3-COLOR IMAGES OF THE LARGEST GALAXIES

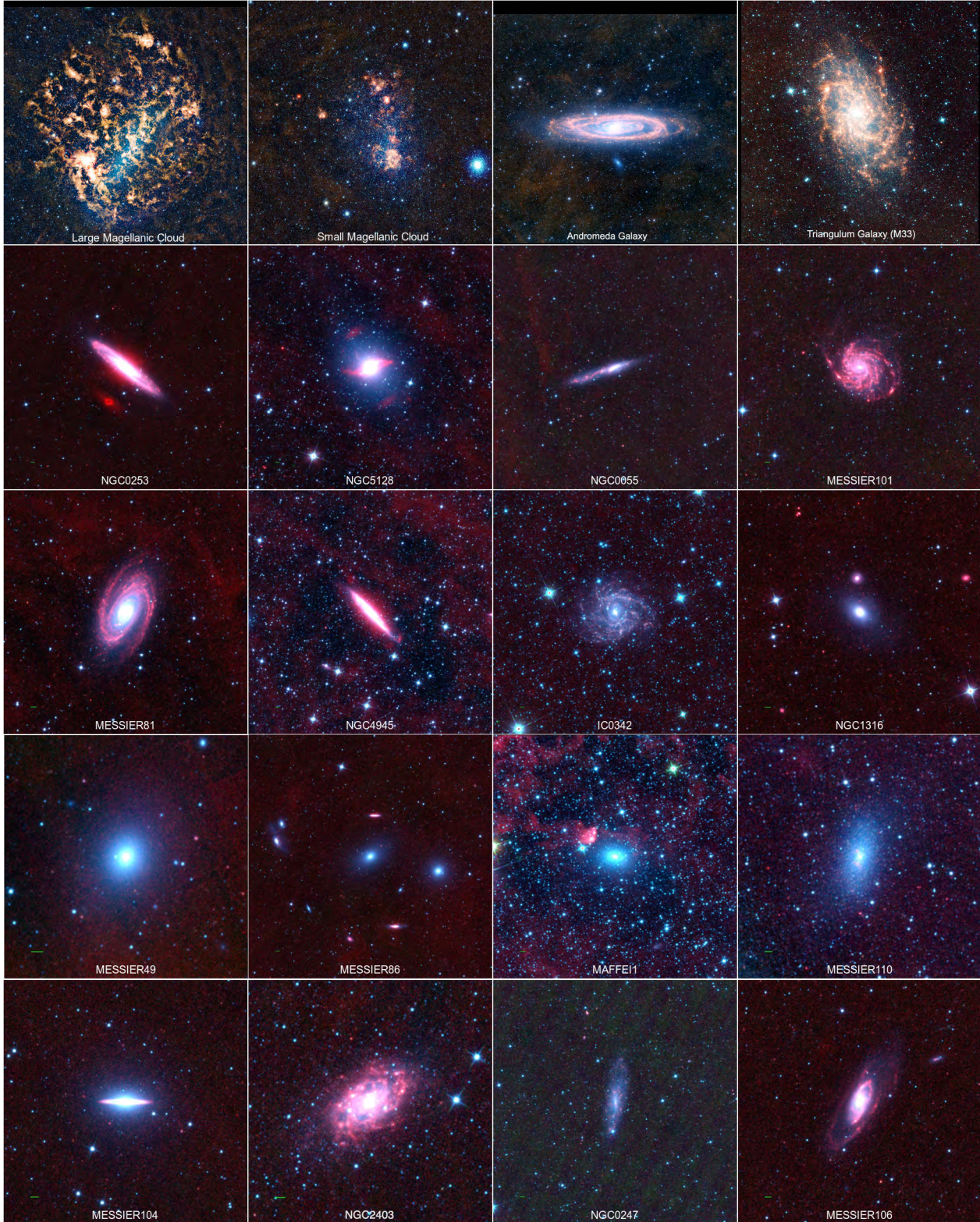


Figure 21. Color combination of the W1, W2 and W3 bands. Assigning the blue (W1) and green (W2) renders the stellar-dominated light to have a blue-cyan hue. Assigning red to W3 highlights star formation sites, appearing yellow-orange-red. Sources that have strong AGN emission will have strong W2 relative to W1, and hence appear yellow/green. In the lower left corner, the green dash specifies 1 arcmin in scale.

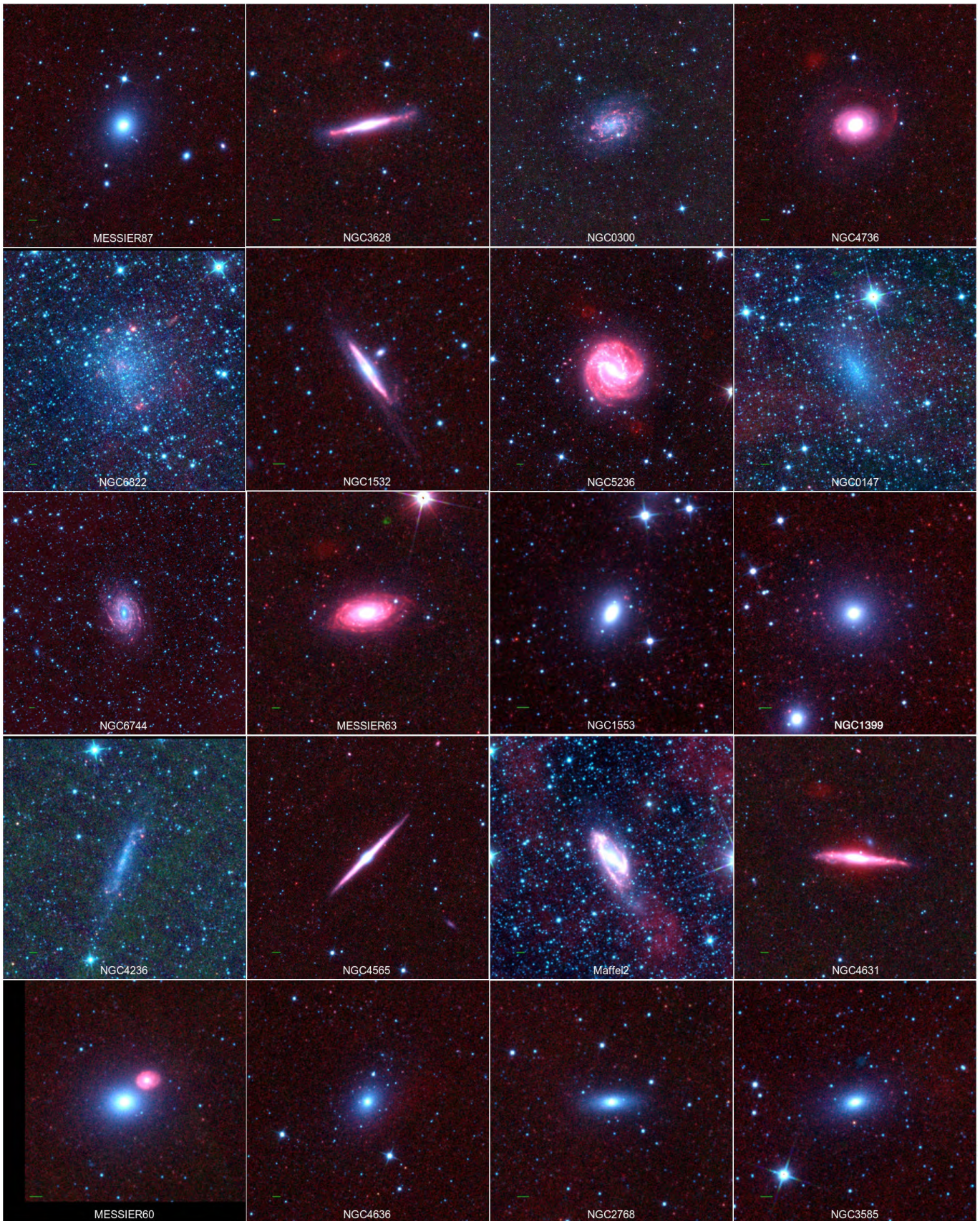


Figure 22. See Fig 21 for details.

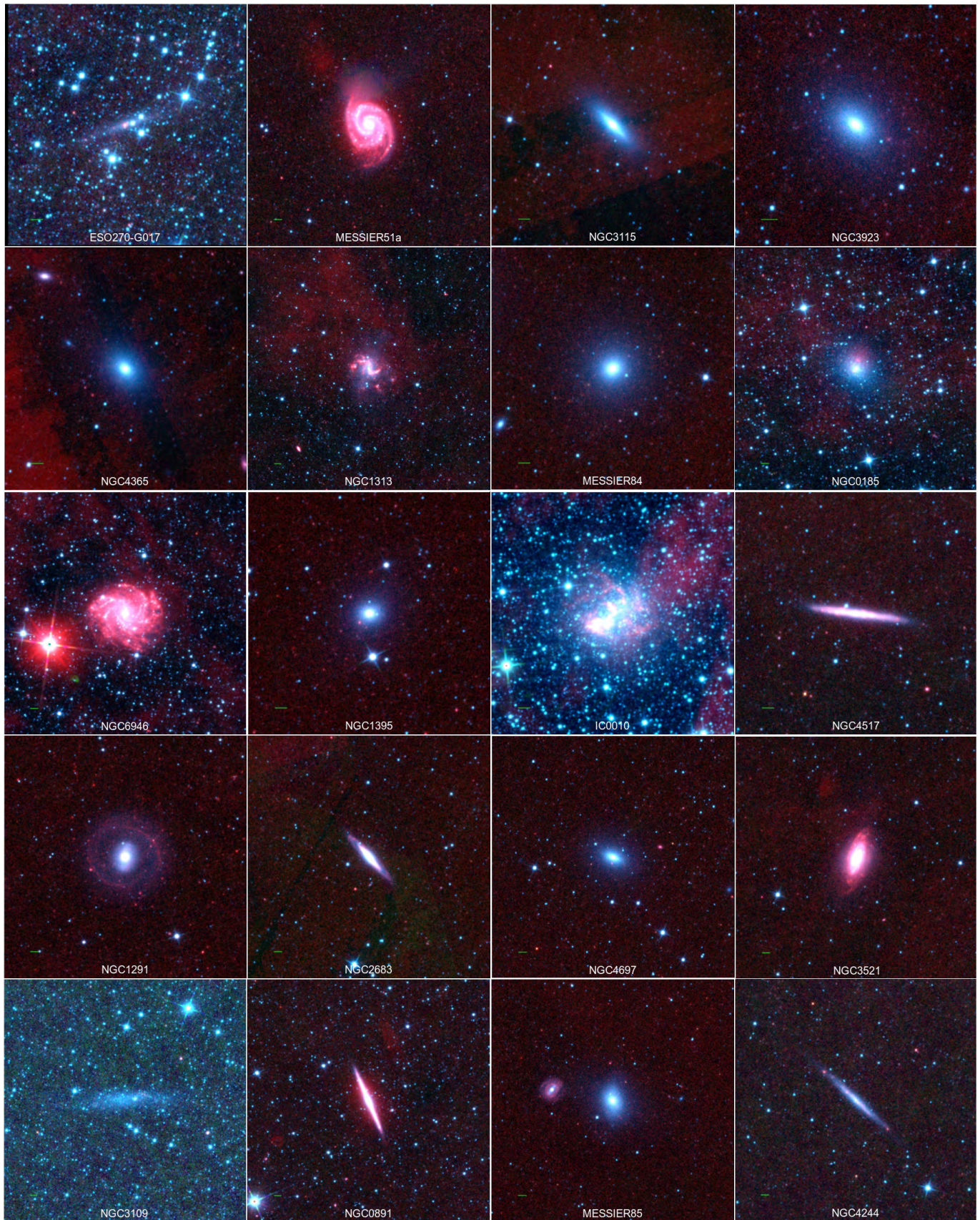


Figure 23. See Fig 21 for details.

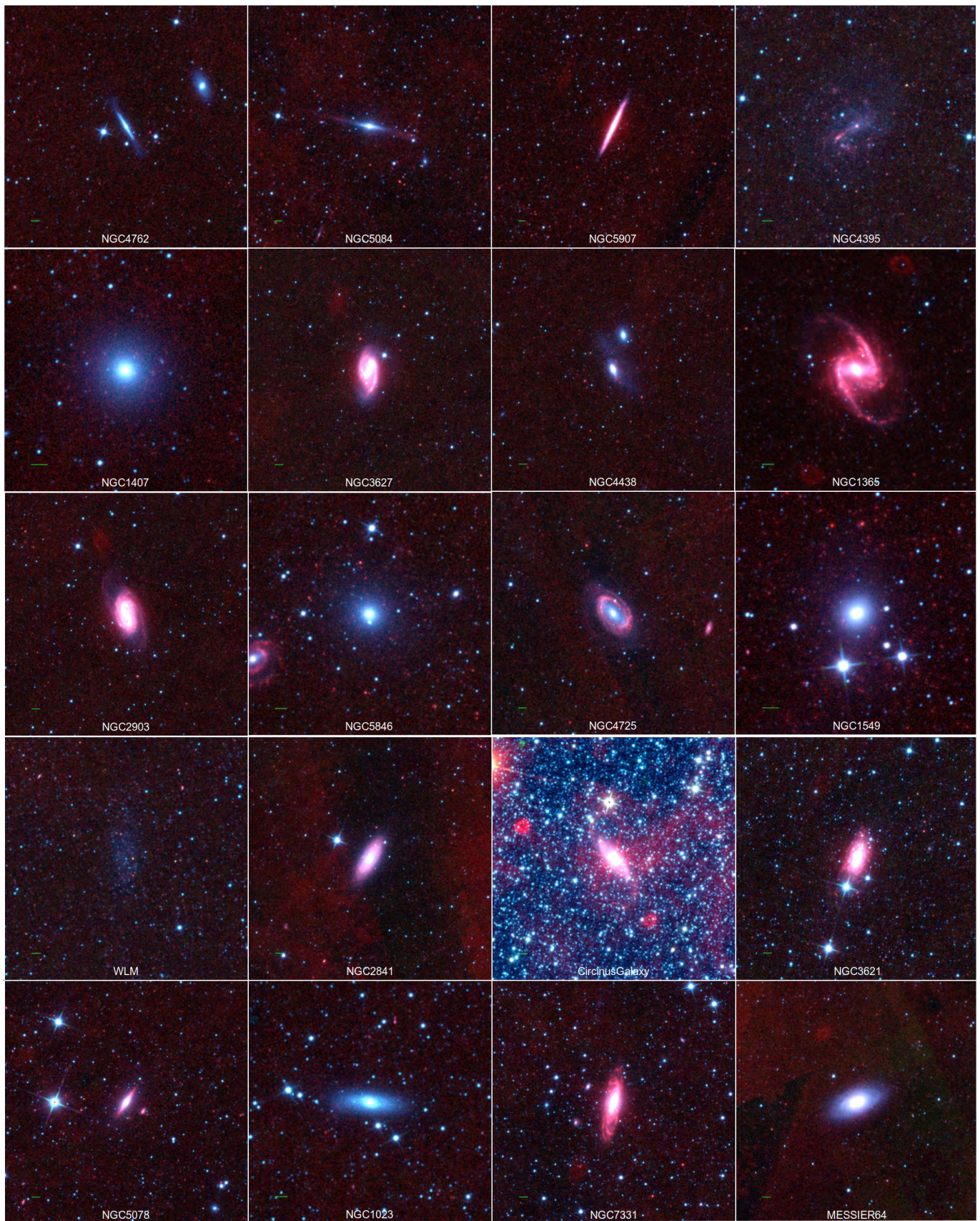


Figure 24. See Fig 21 for details.

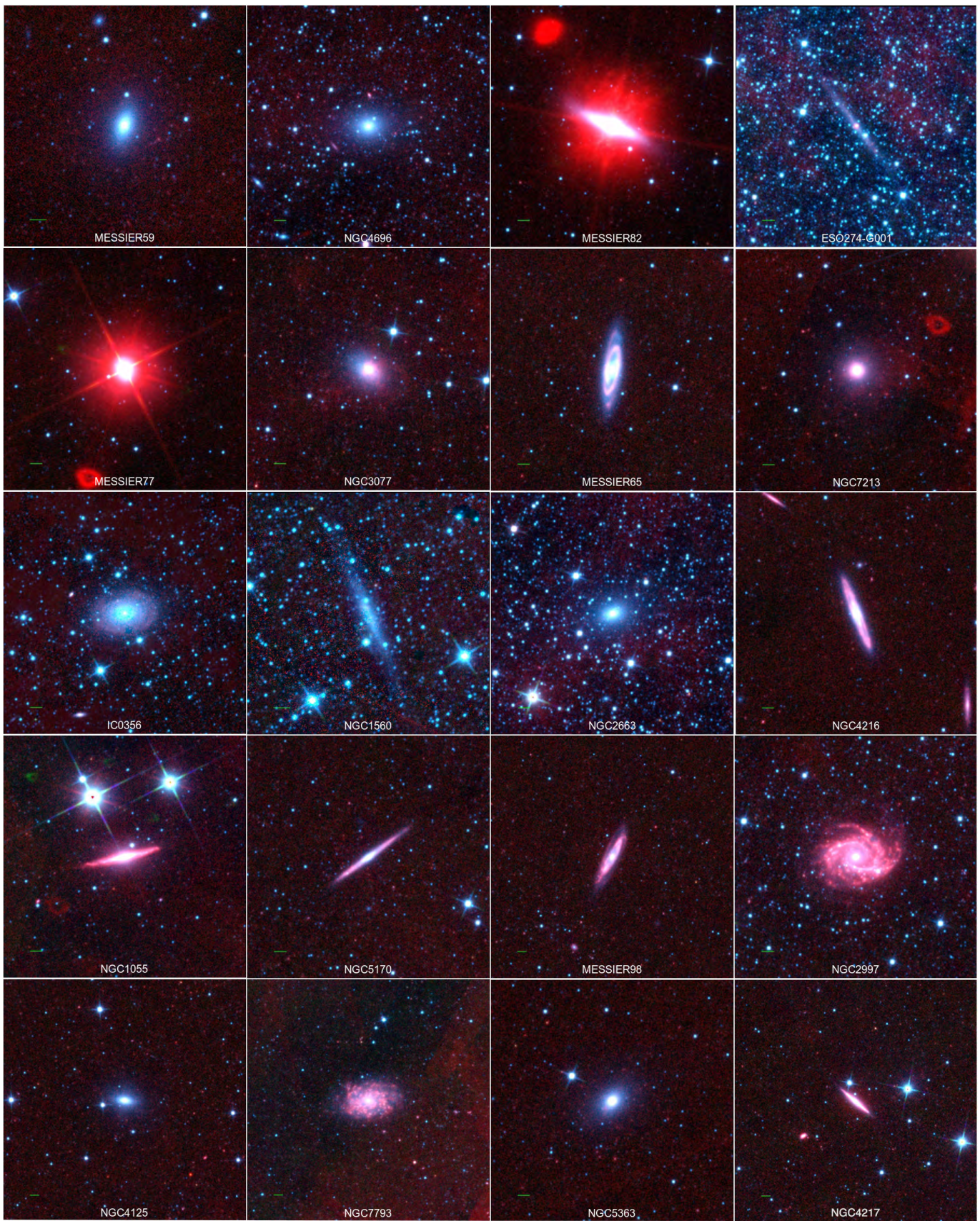


Figure 25. See Fig 21 for details.